Measurement of vertical betatron oscillations using the straw tracking detectors for the E989 muon g-2 experiment at Fermilab.

Thesis submitted in accordance with the requirements of
the University of Liverpool for the degree of Doctor in Philosophy by

Tabitha Leonie Odell Halewood-Leagas

September 2019

Declaration

I hereby confirm that the work presented in this thesis is my own. Where information has been derived from other sources, I confirm that this has been referenced in the thesis.

Tabitha Leonie Odell Halewood-Leagas

Acknowledgements

Firstly I would like to thank my supervisors Themis Bowcock and Barry King for giving me the opportunity to work on this project. A massive thank you to Joe Price. I wouldn't have completed this thesis if it wasn't for your constant advice and encouragement. Thank you to the previous Liverpool g–2 students Saskia Charity and Will Turner for their guidance. I would like to thank the straw tracking construction team Dave Sim, Mike Wormald, Talal Albahri and Kayleigh Thomson for making the long days working in the clean room much more entertaining and fun than it otherwise would have been. And also John Carroll for his advice on the metrology studies. A thank you to Mark Lancaster, Becky Chislett, Gleb Lukicov, Alex Keshavarzi and James Mott amongst others for their help, advice and for making my long term attachment at Fermilab an enjoyable one. Thanks to Heather Wark, Lauren Anthony and Vinicius Franco for their friendship and for motivating one another to complete our theses. Finally a massive thank you to my friends and family for their support throughout my PhD.

Abstract

The measurement of the anomalous magnetic moment of electrons and muons has been an important test of the Standard Model (SM) of particle physics over many decades. This is because it can be measured experimentally and calculated theoretically to a high precision. In particular the anomalous magnetic moment of the muon, a_μ, is an ideal candidate for the search of new physics due to the combination of the muons large mass and relatively long lifetime.

The current world's most precise value of a_μ was measured by the E821 experiment at the Brookhaven National laboratory (BNL). This achieved a precision of $540\,\mathrm{ppb}$ ($463\,\mathrm{ppb}$ stat., $283\,\mathrm{ppb}$ syst.) and measured a $\sim 3.5\,\sigma$ deviation from the SM value [1]. This motivated a new experiment: the E989 muon g–2 experiment at the Fermi National Accelerator Laboratory (Fermilab) to confirm or reject this discrepancy. This experiment aims to gather a data sample 21 times larger than the BNL experiment and improve the determination of the systematic uncertainties by a factor of three and thereby achieve a fourfold increase in precision to $140\,\mathrm{ppb}$ [2]. If the a_μ value were to remain unchanged, this improvement in precision would establish evidence for Beyond SM (BSM) physics with a significance of more than 7 standard deviations.

The Fermilab experiment has the same methodology as the BNL experiment and reuses the experiment's storage ring magnet. New, improved experimental apparatus has been introduced to reduce the systematic uncertainty on the a_μ measurement. One such improvement is the addition of two straw tracking stations. These measure the trajectory of the positrons emitted from the (positive) muon decays which allows a detailed study of the spatial and temporal motion of the beam and critical cross-checks of the calorimeter data.

This thesis describes in detail the design, construction and testing of the tracking detectors which were built at the University of Liverpool. A detailed study of the vertical motion of the beam is also presented. This study provides an important correction that must be applied to the data before a_μ can be determined.

Contents

x

List of Figures

List of Tables

Chapter 1

Introduction

Since the muon was discovered in 1936 [3] its properties have been of great interest to the particle physics community. Of particular interest is how its behaviour differs from the electron and what is the origin of its larger mass. One property in particular; its anomalous magnetic moment, a, has been the subject of detailed study for more than 50 years [4]. Prior to the introduction of Quantum Electrodynamics (QED), the Dirac theory [5] of quantum interactions predicted the anomalous magnetic moment to be exactly zero. The measurement of a non-zero value of a for the electron in 1947 [6] came as a surprise and motivated Schwinger [7], Feynman [8], Tomonaga [9], Dyson [10] and others to develop QED. This theory showed that the non-zero value of a was due to quantum fluctuations of the electromagnetic field around the particle. The measurement of this value with increasing precision underpinned the development of QED to include higher-order interactions and ultimately the extension to incorporate hadronic and weak interactions. The incorporation of all three interaction types in the theory became necessary to explain the measurements. The anomalous magnetic moment of the electron is presently the most precisely measured and predicted value in modern physics. It is measured [11] and predicted [12] to better than one part in 10^{12}. However, despite this precision, its sensitivity to BSM physics is limited to low mass phenomena since typical BSM interactions at an energy scale of Λ contribute to a as $(m/\Lambda)^2$ where m is the lepton mass. Showing that the sensitivity of the lepton magnetic moments to SM/BSM physics increases with increasing lepton mass. So while the precision of the a_e measurements is approximately one thousand times better than the a_μ measurements, it is only sensitive

to QED interactions. The much larger muon mass means that a_μ has a better sensitivity to other parts of the SM than a_e. a_μ experiments are now so precise that they can look for BSM interactions.

Improved measurements of a_e and α, which limit the theory precision, may ultimately lead to the electron having a sensitivity to BSM physics at higher mass scales [15]. Recently the most precise measurement of the fine structure constant has been measured and lead to a new calculation of a_e. The value differs from theory by 2.5 sigma but its sign is opposite to a_μ [13]. It has been found that while there are theoretical models that fit each anomaly separately, there is no appealing model that can fit both simultaneously. An example of this is a model with a massive spin-1 Z' boson (dark photon) coupling very weakly to electrically charged particles through kinetic mixing with the ordinary photon [14]. Where the Z' boson like the photon has vector-like and universal couplings to the muon and electron. This gives a positive contribution to a_μ but does not fit a_e well, which favours a negative contribution.

The lifetime of the τ and the relatively low numbers of τ leptons that can be studied experimentally mean that a_τ [16] has essentially no sensitivity to BSM physics. The muon thus remains the best particle to search for BSM physics through a precise a_μ measurement and this has motivated several generations of experiments to measure a_μ.

Underpinning these experiments was the discovery of parity-violating weak-decays [17, 18]. The maximal parity violation in the weak interaction means that muons from pion decays are polarised and the spin and momentum of the muon are aligned. This allows the direction of the muon's spin to be determined from a measurement of its decay electron. This has been exploited in all a_μ experiments using a muon beam, beginning with the three CERN experiments [19] that took place between 1958 and 1976. The final CERN experiment was the blueprint for the E821 experiment at BNL which finished data taking in 2001 and achieved the most precise measurement to date with a precision of 540 parts per billion (ppb).

The BNL experiment showed a $\sim 3.5\,\sigma$ discrepancy between the measured and theoretically predicted SM value. Since 2001 there have been incremental improvements in the theoretical prediction but the discrepancy remains at 3.3–3.7 σ [20, 21]. The discrepancy has lead to a plethora of papers attributing the discrepancy to BSM

interactions with explanations including, but not limited to, supersymmetry [22], extended Higgs sectors [23], technicolor [24], and extra dimensions [25]. The discrepancy between the BNL measurements and the SM and that no BSM phenomena has yet been observed at the LHC motivates a new measurement of a_μ to determine whether the muon has a hitherto undetected BSM interaction or whether the BNL measurement was merely a statistical fluctuation.

The muon E989 g–2 experiment at Fermilab aims to increase the precision on the a_μ measurement by a factor of four with respect to the BNL experiment in order to prove or refute the discrepancy. The Fermilab experiment has a goal of measuring a_μ to a precision of 140 ppb. It is based on the BNL experiment, reusing the BNL 1.45 T, 14 m diameter storage ring, which was transported to Fermilab in 2013.

The Fermilab experiment has many improvements over the BNL experiment: the beam has a lower pion contamination and the instantaneous rate, mitigating pileup, is lower, while the overall yield of muons is substantially higher owing to the increased number of muon injections per second. The magnetic field is more uniform and is measured more precisely and frequently. The calorimeter system is much more finely segmented with significantly improved spatial and temporal resolutions. The tracking system which is a major part of this thesis is also significantly improved with a larger acceptance, better resolution and electronics permitting measurements immediately after the beam is injected. The tracking system comprises of two stations each containing 8 tracking modules. These contain 128 straws filled with an Argon-Ethane gas mixture each containing a sense wire. The tracking detectors are used to measure the muon beam profile by extrapolating the trajectory of the decay positrons back to the point of the muon[1] decay. The variation of the beam position with time is a very important aspect of the a_μ determination, since the magnetic field is not uniform over the beam profile and the acceptance of the calorimeters depends on the beam position. Unless the beam motion is correctly accounted for in the analysis, it is not possible to determine a_μ accurately and without bias.

The beam was commissioned in June 2016 and the beam storage and performance of the detectors was optimised from November 2017 through to March 2018. The first physics data was taken in March–July 2018 where a sample almost twice the size

---

[1]Hereafter a muon should be taken to refer to a μ^+, unless otherwise stated, since the E989 experiment has a μ^+ beam.

of the BNL dataset was accumulated. This so-called, Run-1 dataset, is the subject of this thesis. Upgrades to the experimental apparatus were undertaken over the summer and winter of 2018, and a second, so-called Run-2, dataset was accumulated from March–July 2019. Together these two datasets have more than four times the statistics of the BNL dataset. A third data run is due to begin in November 2019 and this should bring the size of the dataset to be more than 10 times that of the BNL dataset.

The operating principles, construction and quality assurance testing of the straw tracking detector are a major part of this thesis. The tracking detectors were built and tested in the University of Liverpool clean rooms. I was heavily involved in almost every step of the construction and testing of the straw tracking detectors which took up the majority of the first two and a half years of my PhD. I was also in charge of the metrology survey of the machined pieces of the trackers and the decisions leading to which pieces were used in which module.

Using the data from the straw tracking detectors, I performed a detailed analysis of the vertical motion of the stored muon beam as a function of time after the beam is injected into the storage ring and compared the characteristic frequencies of this motion with those expected. a_μ is determined by a fit to the number of positrons detected in the calorimeters as a function of time, along with a measurement of the magnetic field. An acceptable fit to the data can only be obtained if a parameterisation of the vertical beam motion is incorporated into the fit and if a correction is applied to account for the fact that the beam is not perfectly perpendicular to the magnetic field. My analysis determined this correction and the parameterisation of the vertical motion: both of which are critical in the determination of a_μ.

Chapter 2

The theory of lepton anomalous magnetic moments

2.1 Introduction

In Particle Physics, the study of the anomalous magnetic moment of the muon is particularly fascinating due to the wide range of SM physics it is sensitive to and the precision with which it can be measured both experimentally and predicted theoretically. It also provides a sensitive probe of BSM physics.

The magnetic dipole moment relates the torque experienced by a charged particle to the external magnetic field. The torque acts perpendicular to both the magnetic dipole moment and the magnetic field and causes the magnetic dipole moment to precess about the direction of the magnetic field at the so-called Larmor frequency.

In quantum mechanics, charged particles with a non-zero spin have an intrinsic magnetic dipole moment, μ, arising from the spin, even when at rest. The magnetic dipole moment for a spin-$\frac{1}{2}$ charged particle is given by:

$$\vec{\mu} = g\frac{Qe}{2m}\vec{s},$$

(2.1)

where g is the gyromagnetic ratio, Q is the sign of the charge, e is the charge of the proton, m is the mass and $\vec{s}$ is the spin of the particle. The gyromagnetic ratio, also known as the g-factor, is the dimensionless proportionality constant relating the angular momentum and the intrinsic magnetic moment.

After the discovery of spin, Dirac predicted that the g-factor of a spin-$\frac{1}{2}$ particle, such as electrons and protons should be equal to 2 [5]. However in 1933, Frisch, Stern and Estermann carried out measurements of the magnetic moment of the proton, which at the time was considered to be a point-like Dirac particle. To everyone's surprise, it was discovered that the g-factor of the proton was in fact approximately 5.5 [27, 28]. This was followed by measurements of the neutron [29] which was assumed to have no magnetic moment due to its zero charge. However it was also measured to have a large magnetic moment. This lead to the first experimental evidence that nucleons were composite particles and ultimately that their magnetic moments were understood to arise from the magnetic moments of the point-like constituents of the nucleon i.e. the quarks and gluons.

At the same time, experiments indicated that the electron g-factor was consistent with $g_e = 2$. However in 1947, a deviation was observed by the Kusch and Foley experiment which found a $0.12\,\%$ increase in this value, thereby indicating an unknown, "anomalous" contribution to the magnetic moment [6].

This was resolved theoretically by Schwinger in 1948 [7] by exploiting the emergent theory of Quantum Electrodynamics (QED). This explained that the discrepancy was caused by a small radiative correction to the lowest order Dirac moment. This resulted in the calculation of the lowest order self-interaction term for leptons emitting and reabsorbing photons. The Feynman diagram for this is shown in Figure 2.1. The Schwinger term for the leading-order (LO), one-loop correction, to g_e is given by

$$a_l^{\mathrm{QED}} = \frac{\alpha}{2\pi}, \tag{2.2}$$

where α is the electromagnetic coupling constant.

This correction accounted for the experimentally measured deviation from 2 and provided an early success of QED. The corrections to the g-factor are known collectively as the anomalous magnetic moment, which for a lepton, l, is given by

$$a_l = \frac{g_l - 2}{2}. \tag{2.3}$$

Although the majority of the anomaly originates from QED processes, there are smaller contributions from electroweak and hadronic processes which will be dis-
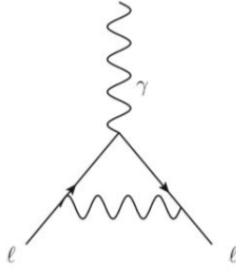
Figure 2.1: Feynman diagram of the Schwinger, leading-order, QED contribution to a_l.

cussed in the next section.

2.2   Standard Model value of a_μ

The high precision to which a_μ has been and is intended to be measured demands a corresponding precision in the SM theoretical prediction. The comparison between the experimental measurement and theory provides a stringent test of the SM. In the SM, contributions to a_μ arise from QED, strong (Had.) and electroweak (EW) interactions, i.e.

$$a_\mu^{\mathrm{SM}} = a_\mu^{\mathrm{QED}} + a_\mu^{\mathrm{Had.}} + a_\mu^{\mathrm{EW}}. \tag{2.4}$$

There is possible interference in these processes as any interaction that involves an electroweak process falls into the electroweak contribution. These include purely electroweak processes, electroweak with QED processes and electroweak with hadrons processes all being parts of the electroweak contribution. Each of the above contributions will be discussed below, with the contribution to a_μ^{SM} and its uncertainty quoted for each part.

2.2.1   QED contributions to a_μ

QED interactions contribute $\sim 99.99\,\%$ to the value of a_μ^{SM}, but these interactions are very precisely predicted. The QED contributions to a_μ consists of all virtual photon and lepton loops. The leading order contribution is the same as the electron and is simply the Schwinger term: $\frac{\alpha}{2\pi}$. At next-to-leading order (NLO) there are

nine two loop processes, one of which is shown in Figure 2.2. The QED contribu-
tions have recently been calculated up to and including the five loop interactions by
Kinoshita *et al.* [12, 34]. A subset of the 12,672 five loop Feynman diagrams are
shown in Figure 2.3. While the number of interactions calculated is large and the
total contribution dominates, the uncertainty in the QED calculations is significantly
smaller than the uncertainty in the hadronic and electroweak contributions.

The SM theoretical value for the QED contribution to the anomalous magnetic mo-
ment is determined to be

$$a_\mu^{\text{QED}} = 116584718.97(0.07) \times 10^{-11}. \tag{2.5}$$
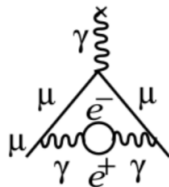
Figure 2.2: An example QED NLO Feynman diagram contributing to a_μ.
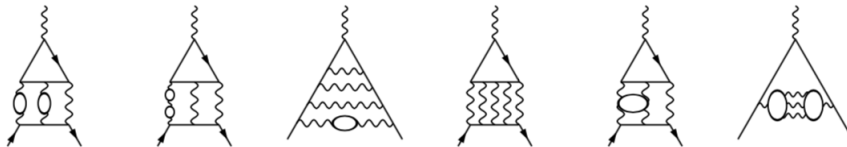
Figure 2.3: Feynman diagrams for a number of typical five-loop QED contributions.

2.2.2   Electroweak contributions to a_μ

The electroweak contribution arises from loop interactions of W, Z and Higgs bosons.
Their large masses suppress their contribution and the electroweak interactions are
the smallest contribution to a_μ. A subset of the electroweak contributions to a_μ are
shown in Figure 2.4. The interactions have been determined [35, 37, 43] to high
accuracy up to NLO and are dominated by the LO contribution.

The SM theoretical value for the electroweak contribution is determined to be

$$a_\mu^{\text{EW}} = 153.6(1.0) \times 10^{-11}. \tag{2.6}$$
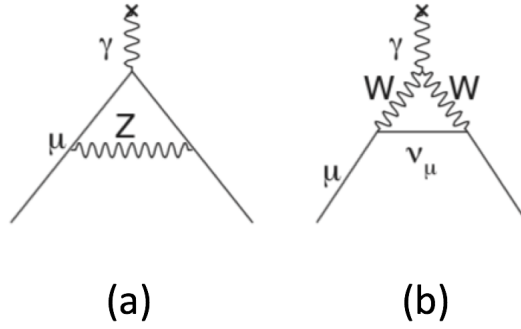
Figure 2.4: Electroweak contributions to the anomalous magnetic moment. (a) The LO electroweak interaction. It is identical to the Schwinger term, except the photon is replaced by a Z boson. (b) The largest NLO contribution to a_μ^{EW}.

2.2.3   Hadronic contributions to a_μ

Hadronic interactions contribute the largest uncertainty in the SM prediction of a_μ. These interactions arise from virtual quark and gluon loops and can be divided into two contributions: the hadronic vacuum polarisation (HVP) and the hadronic light-by-light (HLbL) contribution:

$$a_\mu^{\text{Had.}} = a_\mu^{\text{HVP}} + a_\mu^{\text{HLbL}}. \tag{2.7}$$

The hadronic contributions, unlike the QED and electroweak contributions, cannot be determined by a perturbative calculation [38]. This is because the energy scale of the virtual hadronic interactions is of the order m_μ, which lies below the perturbative region of QCD. Instead the HVP calculation relies on data from low-energy e^+e^- experiments. This is because the HVP contribution to a_μ can be related via a dispersion relation to the cross section for e^+e^- annihilation into hadrons. Thus the measured cross sections of e^+e^- annihilation into hadrons is used to make a HVP calculation [39]. An example HVP Feynman diagram is shown in Figure 2.5. The LO HVP contribution determined from the dispersion relation is given by

$$a_\mu^{\text{Had.(LO)}} = \left(\frac{\alpha m_\mu}{3\pi}\right)^2 \int_{m_\pi^2}^\infty \frac{ds}{s^2} K(s) R(s), \tag{2.8}$$

where $R = \dfrac{\sigma_{\text{tot}}(e^+e^- \to \text{hadrons})}{\sigma(e^+e^- \to \mu^+\mu^-)},$ $\tag{2.9}$

where s^2 is the centre of mass energy, $K(s)$ is a kinematic factor with a value of 0 at $s = \infty$ and 0.4 at $s = m_\pi^2$. Due to the $1/s^2$ dependence, the value of $a_\mu^{\text{Had.(LO)}}$ is dominated by the $R(s)$ values at low energies i.e. below $2\,\text{GeV}$. Cross-section data from a range of experiments including KLOE, BaBar, BELLE, VEPP and BES have been combined in order to determine the HVP contribution [20, 21].
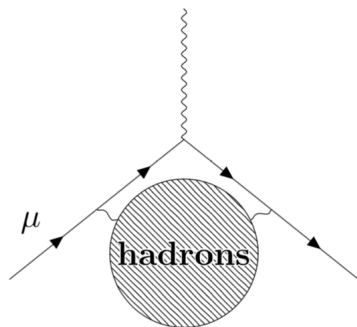
Figure 2.5: The Feynman diagram of the LO hadronic vacuum polarisation contribution to a_μ.

Unlike the HVP contribution, the hadronic LbL contribution cannot be determined directly from experimental data and instead a mixture of experimental data, lattice QCD calculations and somewhat ad-hoc models are utilised. Several groups have made independent determinations and these are combined by a group comprising of all those involved in the calculations. The present combination is embodied in the so-called "Glasgow consensus" [41] and is in the process of being updated ready for the release of the Fermilab muon g–2 measurement. A reduced uncertainty is anticipated in this new combination largely due to recent advances in the lattice QCD calculations. The LO hadronic LbL Feynman diagram is shown in Figure 2.6. Overall the uncertainty on a_μ^{SM} is dominated by the HVP and LBL contributions, with both contributing approximately 25×10^{-11} [41, 42, 40].
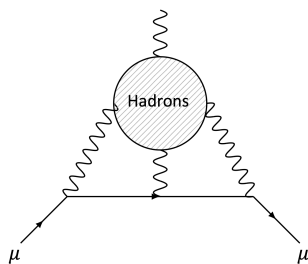
Figure 2.6: Feynman diagram showing the LO hadronic light-by-light process.

The hadronic contributions to a_μ^{SM} are determined to be

$$a_\mu^{HVP} = 6933(25) \times 10^{-11}, \tag{2.10}$$

$$a_\mu^{HLbL} = 980(26) \times 10^{-11}. \tag{2.11}$$

Where the HVP value is taken from the recent KNT analysis of the e^+e^- data [21] and the LbL value is from the "Glasgow consensus".

2.2.4   Value and uncertainty of a_μ^{SM}

The SM contributions can be summed together to give an overall determination of the SM value of a_μ^{SM} and its uncertainty [21]. The individual contributions to a_μ^{SM} are shown in Table 2.1.

Contribution	Result (10^{-11})
QED	116584718.97 $\pm$ 0.07
HVP	6933 $\pm$ 25
HLbL	980 $\pm$ 26
EW	153.6 $\pm$ 1.0
Total SM	116591820.4 $\pm$ 35.6

Table 2.1: Table of all the contributions to a_μ^{SM}.

The SM value of a_μ^{SM} is determined to be

$$a_\mu^{\text{SM}} = 116591820.4(35.6) \times 10^{-11}. \tag{2.12}$$

As mentioned previously the current best experimental measurement of a_μ was determined by the BNL E821 experiment in 2001 [43, 4] giving

$$a_\mu^{\text{Exp.}} = 116592091(54)(33) \times 10^{-11}, \tag{2.13}$$

where the value in the first bracket is the statistical uncertainty and the value in the second bracket is the systematic uncertainty. The difference between the experimental and theoretically calculated a_μ is

$$a_\mu^{\text{Exp.}} - a_\mu^{\text{SM}} = 270.6 \pm 72.6 \times 10^{-11} \qquad (2.14)$$

corresponding to a $3.7\,\sigma$ difference. If instead the analysis of [20] is used to determine a_μ^{HVP}, the difference is reduced somewhat to $3.3\,\sigma$. If this observed difference is not a statistical fluctuation, it could indicate the presence of a BSM contribution to a_μ.

To investigate this discrepancy a new experiment, the Fermilab E989 muon g–2 experiment has been designed to improve on the accuracy of the BNL experiment by a factor of four. If the value of a_μ is unchanged after this experiment, the expected reduction in the a_μ uncertainty would result in a $\sim 7\sigma$ deviation from the SM as shown in Figure 2.7 [44]. Improvements in the lattice QCD calculations and new e^+e^- datasets e.g. from BES-III are also expected to reduce the uncertainty in the determination of $a_\mu^{\text{Had.}}$. The comparison of the measurement and the SM prediction remain an important test of the SM and could potentially highlight the existence of BSM physics.
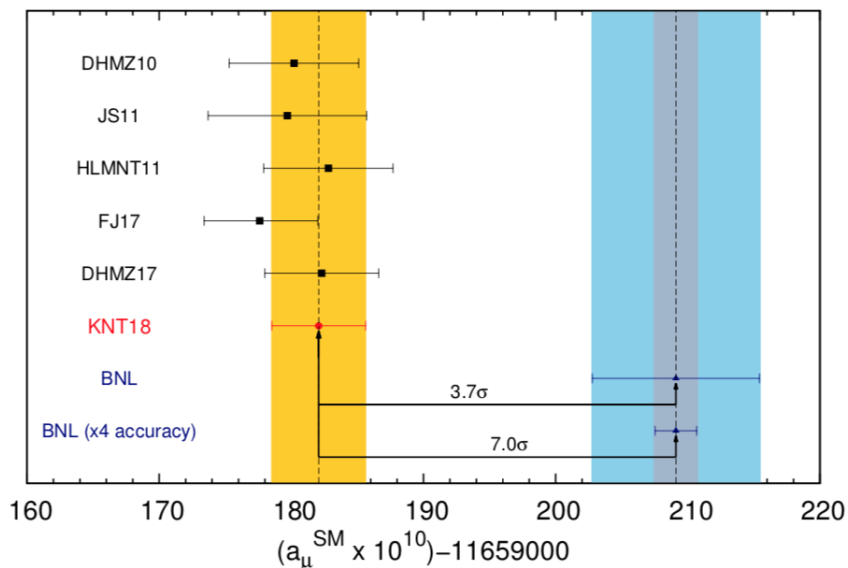
Figure 2.7: A comparison of recent evaluations of a_μ^{SM} [21]. The BNL measurement and the equivalent result with the expected improvements to the uncertainty are also shown.

2.3   Possible new physics contributions to a_μ

A possible explanation for the discrepancy between the experimental measurement and theoretical prediction of a_μ is from BSM physics. It is known that the SM is an incomplete theory. BSM refers to the theoretical models required to describe fundamental physical phenomena in nature which are currently unexplained. These include neutrino masses, gravity, dark matter, strong-CP violation and matter-antimatter asymmetry which are discussed briefly below.

- Neutrino masses: In the SM, neutrinos are massless particles. This has been disproven through observations of neutrino oscillations which indicate that neutrinos do have a small mass. The addition of these mass terms however leads to further theoretical issues, as it is not certain if the neutrino masses are created by the same processes in which other fundamental particles attain mass.

- Gravity: The SM omits gravity and seems to have no impact on the subatomic interactions that the SM describes. The SM is considered to be at odds with general relativity and the inclusion of the graviton into the SM does not recreate what is observed in nature.

- Dark matter: Due to cosmological observations, it has been shown that approximately 25% of matter in the universe originates from the as yet unexplained dark matter. The SM does not give any suitable candidate particles. As dark matter is not observed directly, it is thought to scarcely interact with SM fields and only interacts with gravity.

- Strong-CP problem: Seeks an explanation as to why Quantum Chromodynamics (QCD) appears to conserve Charge-conjugation Parity (CP) symmetry. No experiment has observed a violation of CP symmetry in a strong interaction and there is as yet no known reason as to why it is conserved.

- Matter-antimatter asymmetry: Describes the imbalance in baryonic matter and antimatter in the universe. The SM predicts that equal amounts of matter and antimatter should have been created in the Big Bang. However the universe has a disproportionate amount of matter compared to antimatter. The SM has no explanation to explain the physical phenomena which caused this asymmetry.

The size of the contribution to a_μ from BSM interactions tends to decrease with the mass scale of the BSM phenomena. Given the size of the discrepancy, most of the BSM phenomena proposed to explain the discrepancy have mass scales in the region of the electroweak scale and the measurement thus probes a similar energy scale to the LHC experiments. Any BSM interaction contributing to a_μ must be CP and flavour conserving and flip the chirality of the muon. The interaction must be CP conserving because the magnetic dipole moment is not flipped under a time reversal transform, and so to conserve CPT it must be CP conserving. It is flavour conserving because the Feynman diagrams have an incoming muon and an outgoing muon. The interaction is chirality flipping because the muon is converted from a left-handed muon into a right-handed muon. These interactions complement other searches for new physics e.g. those explicitly searching for CP or flavour violations. There are a variety of BSM models that could explain the anomaly. These include supersymmetry (SUSY), additional electroweak bosons e.g. W' or Z' and extended-Higgs models [26]. The Feynman diagram of a SUSY contribution to a_μ is shown in Figure 2.8 and the magnitude of a_μ can be used to place constraints on the parameters of a given SUSY model e.g. a_μ has a dependence on $\tan\beta$ [45, 46] as shown below

$$|a_\mu^{\text{SUSY}}| \approx (\text{sgn } \mu)130 \times 10^{-11} \tan\beta \left(\frac{100 \text{ GeV}}{\tilde{m}}\right)^2. \tag{2.15}$$

For a $\tan\beta$ value of 50, the observed discrepancy can be explained with sleptons of a mass ($\tilde{m}$) of ≈ 500 GeV [44, 47].
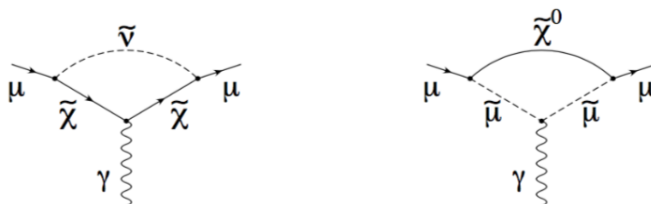
Figure 2.8: Feynman diagrams of two SUSY interactions contributing to a_μ. The left diagram, shows the muon interaction with a chargino $\tilde{\chi}$ and a sneutrino $\tilde{\nu}$ and the right diagram shows an interaction with a smuon $\tilde{\mu}$ and a neutralino $\tilde{\chi}^0$.

The measurement at Fermilab will constrain the parameters of BSM models. More-

over if BSM physics is discovered elsewhere the measured value of a_μ will be critical in elucidating the nature of the BSM interaction. As such, it remains one of the most anticipated measurements in particle physics.

Chapter 3

Experimental technique

3.1 Previous muon g–2 measurements

The first measurements of a non-zero a_μ were conducted at CERN until the mid 1970s following on from the initial investigations of Lederman [30] at Columbia into the parity violating nature of pion and muon decays. These and subsequent measurements have exploited the fact that muons produced from pion decay are polarised and that the direction of the highest energy positrons are aligned with the spin of the muon such that the spin precession of the muon in a magnetic field can be measured by recording the rate at which positrons are detected in a fixed detector. This rate has a sinusoidal dependence due to the precession of the muon spin (and hence direction of the positrons) in a magnetic field.

The evolution in precision of muon g–2 experiments is shown in Figure 3.1 and these experiments are described briefly below.

3.1.1 CERN-I (1958–1962)

The CERN-I experiment [31] located in the experimental hall of the CERN Synchro-Cyclotron became the first experiment to determine a non-zero value of a_μ. A 6 m, 1.5 T bending magnet produced a uniform field between two rectangular pole pieces as shown in Figure 3.2. This enabled muons to undergo up to 2,000 turns within the muon storage time period of $2\,\mu\text{s}$–$8\,\mu\text{s}$. The muons were injected into the magnet and directed towards an absorber material inside the magnetic field. The energy loss in the absorber caused the muons to change direction and follow a helical orbit
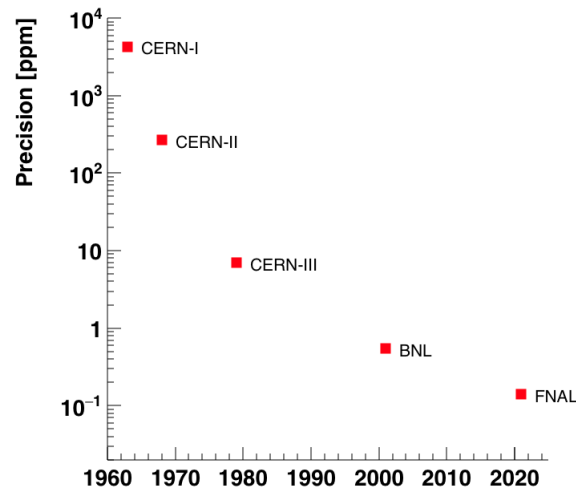
Figure 3.1: The precision achieved by a_μ measurements for all previous experiments and the target a_μ precision for the current Fermilab experiment.

in the magnetic field. A transverse magnetic field gradient was applied to ensure the muons did not hit the absorber material on subsequent turns and to guide the muons horizontally from one side of the magnet to the other. At the opposite end of the magnet, a large magnetic gradient was used to eject the muons from the magnet and direct them at an absorber where they were stopped and decayed into positrons. The spin directions of the incident muons were measured by recording the decay positrons in forward and backward counters and the storage time was determined by counters at either end of the magnet.

This experiment determined an a_μ value of

$$a_\mu = 1162(5)\times10^{-6}. \tag{3.1}$$

3.1.2 CERN-II (1962–1968)

By now it had been acknowledged that the best candidate for BSM physics searches was a more precise measurement of a_μ. To achieve this, an experiment was needed that could store a larger number of muons for an increased amount of time in order to observe more muon g–2 cycles compared to the CERN-I experiment. The new CERN
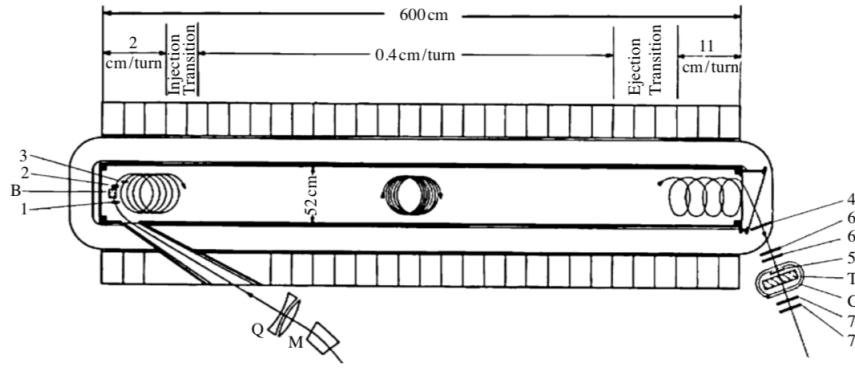
Figure 3.2: The CERN-I experiment. A 6 m bending magnet stores the muons. The muons enter through a bending magnet (M) and a focussing quadrupole. The muons are directed to a target (B), follow a helical orbit and drift towards the opposite end of the magnet where they are ejected from the magnetic field. Here they are stopped by an absorber and decay into positrons. The storage time of the muon in the magnetic field was recorded by coincidences in counters 123 at the input, and at the output with counters 466' and 57' [4].

proton synchrotron (PS) was ideal for this purpose as it could supply higher energy muons (of order GeV) whose lifetime was relativistically dilated. This experiment was the first to utilise a weak focusing magnetic field storage ring. 10.5 GeV protons were injected onto a pion production target situated inside a 5 m diameter storage ring. A diagram of the CERN-II [32] experiment is shown in Figure 3.3. The pions subsequently decayed in flight to produce muons. The stored muons were mainly from forward pion decays that had lost a small amount of energy and as such did not strike the production target in further orbits of the ring. The stored muons had a momentum of 1.28 GeV/c and a gamma factor $\gamma = 12$ giving a relativistically dilated lifetime of 27 μs. These muons subsequently decayed to positrons which curled inwards towards the detectors. This experiment improved the accuracy of a_μ by a factor of 15. Leading to an a_μ value of

$$a_\mu = 1165922(9) \times 10^{-9}. \tag{3.2}$$
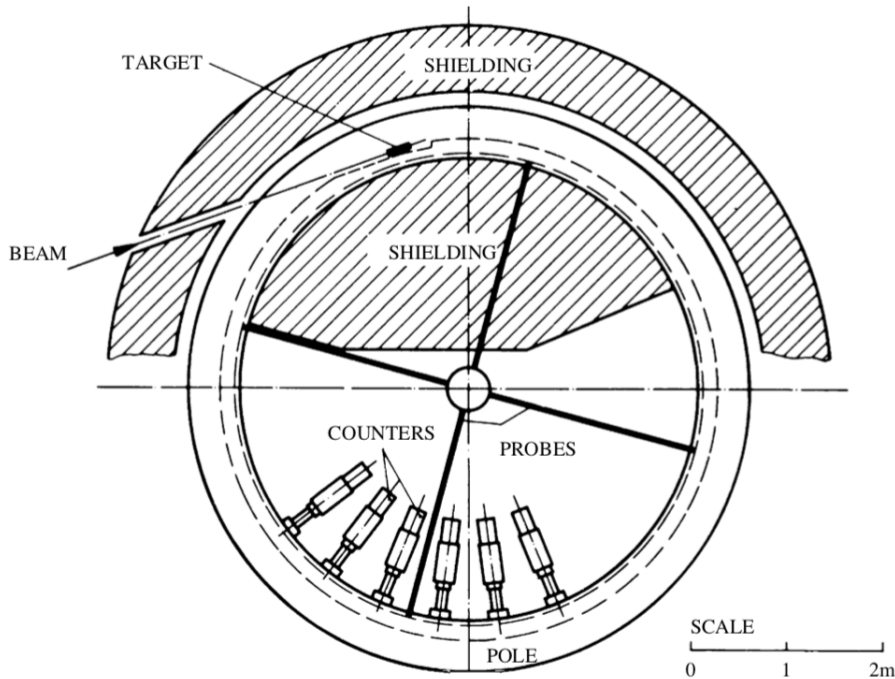
Figure 3.3: An illustration of the CERN-II experiment [4].

3.1.3 CERN-III (1969–1976)

The CERN-III experiment [33] utilised a new $14\,\mathrm{m}$ diameter storage ring installed in the CERN Super Proton Synchrotron (SPS) and was the blueprint for the BNL and Fermilab experiments. The experiment is shown in Figure 3.4. This experiment used electrostatic quadrupoles and not a graded magnetic field to vertically focus the beam and introduced the concept of the muon "magic" momentum (see section 3.5). The absence of a graded magnetic field enabled a more precise determination of the magnetic field compared to the CERN-II experiment. The momentum of the beam (3.094 GeV/c) was also higher than CERN-II allowing a longer measurement period. The experiment also utilised pion injection rather than proton injection which reduced the background and increased the beam intensity. These improvements led to an uncertainty on a_μ of $8\,\mathrm{ppm}$ and a value of

$$a_\mu = 116592300(800)\times10^{-11}. \tag{3.3}$$
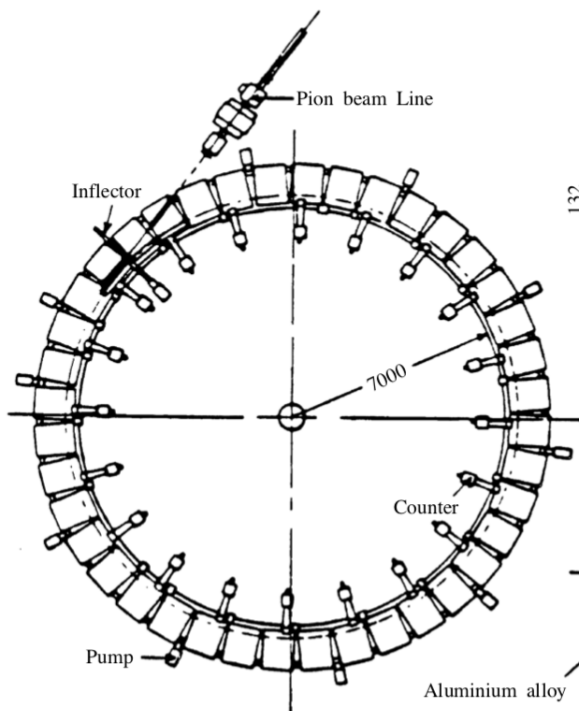
Figure 3.4: An illustration of the CERN-III experiment [4].

3.1.4 The E821 experiment at the Brookhaven National Laboratory (1984–2003)

The BNL E821 experiment [1] shown in Figure 3.5 carried out the most precise measurement of a_μ to date. The experiment used the Brookhaven Alternating Gradient Synchrotron and the same methodology as the CERN-III experiment except muons were injected into the storage ring and not pions. This reduced the backgrounds from pion interactions enabling data to be recorded at earlier times than CERN-III and a significantly larger data sample was accumulated. The magnetic field was determined with a much better precision utilising 360 stationary NMR probes and a novel trolley equipped with 17 NMR probes that could traverse the storage ring. The experiment ultimately achieved an uncertainty on a_μ of 540 ppb, giving a value of

$$a_\mu = 116592082(54) \times 10^{-11}. \tag{3.4}$$

Figure 3.5: The storage ring of the BNL E821 experiment [2].

3.2 The E989 Fermilab muon g–2 experiment

The E989 Fermilab muon g–2 experiment aims to measure a_μ, to a world's best precision of 140 ppb [35]. This would be an improvement of almost a factor of four compared to the E821 measurement.

The experiment applies the same measurement principle as the BNL E821 experiment but with 21 times the data sample (1.5×10^{11} e$^+$) and a reduction in the systematic uncertainty by a factor of 3 to $\sim$100 ppb. Table 3.1 outlines how the precision will be improved compared to the E821 experiment.

Category	E821 [ppb]	E989 improvement	E989 Goal [ppb]
Gain changes	120	Better laser calibration. Low energy threshold	20
Pileup	80	Low energy samples recorded. Calorimeter segmentation	40
Lost muons	90	Better collimation in ring	20
CBO	70	Higher n value (frequency). Better match of beamline to ring	< 30
E and pitch	50	Improved tracker. Precise storage ring simulations	30
Total	180	Quadrature sum	70

Table 3.1: Table of the largest systematic uncertainties for the BNL E821 experiment along with the improvements implemented in the Fermilab experiment.

The gain changes systematic is used to correct any systematic hardware gain drifts throughout for the calorimeter detectors. This is where the positron energies measured in the calorimeter crystals are gain corrected using in fill and out of fill laser calibrations.

In fill gain: At beam injection, some muons are not stored and travel inwards towards the calorimeters. This is called the flash, with the calorimeters close to the injection region receiving the majority of these muons. The calorimeter electronics require time to recover from this saturation of events. This saturation leads to the mismeasurement of positron energies. To correct for this effect, photons of fixed energy are fired at different times throughout the fill. This measures the calorimeters response as a function of time in the fill. Figure 3.6 shows a plot of the typical response of a calorimeter crystal with time. Initially the response drops down due to saturation of the electronics, which then recovers over time. Thus for a particle detected at a certain time, the calorimeter response is determined and a correction to it's measured energy can be applied. This is important as any uncorrected fluctuations in the gain causes an effective change in the energy threshold throughout the fill. This would modify the average measured phase of the detected positrons.
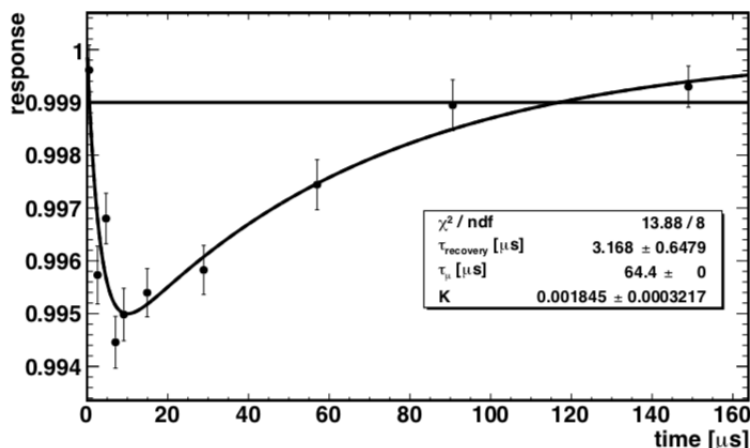
Figure 3.6: A plot showing a calorimeter crystal response to a fixed energy laser fired at varying times during the fill, from which the gain values can be determined. [2].

Out of fill gain: These measurements are carried out by firing photons of fixed energy between fills at each calorimeter crystal, looking for long term drifts in their performance. The effects measured are largely temperature dependent, for instance

an increase in the experimental hall temperature. This would cause the calorimeters to experience higher levels of noise and thus measure positron energies less accurately. These effects need to be accounted for. This is done by measuring changes in the photon energy detected by the calorimeter. The difference between the measured and known energy is used to determine gain corrections which are applied to events throughout the fill.

The pileup systematic is used to correct events where two or more particles overlap spatially and temporally in the calorimeter and are reconstructed into a single pulse with the combined energy of all the particles. Unlike E821, E989 uses segmented calorimeters. These are able to record a higher rate of statistics and measure lower energy events. A calorimeter is also placed at the end of each tracking station, enabling a cross check between the two detectors. This would typically be recognised by a tracker measuring two or more particles in a certain time period, which when extrapolated to the calorimeter, are all reconstructed as a single pulse.

The lost muon systematic is used to correct for muons which are not stored at the magic radius and travel towards the detectors before they decay. At E821, due to temperature changes, the average radial magnetic field would change by about 40 ppm every month, reducing storage of the muon beam. This meant every month the average radial magnetic field had to be centered using shims to increase muon storage. E989 possesses much better temperature control and precision shimming and aims to reduce this change to < 10 ppm per month. Due to the upgraded kicker system, it only takes E989 one cycle of the storage ring to move muons onto the correct orbit position. This is compared to E821 which took many turns around the storage ring. This means that full collimators can be used instead of half collimators, leading to increased removal of muons at the outer edges of the beam distribution. These collimators are also oval shaped rather than round to better match the muon beam distribution. The better collimator control along with the reduced change in the average radial magnetic field leads to lower beam distortions and therefore a reduced number of lost muons after the scraping process.

The CBO systematic is caused by the mismatch of the muon beam injection into the storage ring. This leads to Coherent Betatron Oscillations (CBO), where the average position and width of the muon beam varies throughout the fill as it is focused and

defocused around the storage ring. For the E821 2000 data run the f_{CBO} was close to the second harmonic of the ω_a frequency. This meant that the difference frequency $f_{CBO} - \omega_a$ was very close to ω_a. This caused problems with its fitting and lead to a systematic error. The 2001 data run sort to lower this error by changing the field index which controls the vertical focusing achieved by the quadrupoles. E989 will further reduce this systematic error by changing the quadrupole voltage by an additional 30%. The calorimeter's vertical length is also a centimeter longer to increase the detector acceptance to the muon beam position and width through a reduced number of positrons missing the detectors.

The electric field (E-field) and pitch corrections modify the final value extracted for ω_a. Therefore errors originating from these corrections are by extension errors on the ω_a measurement. The E-field correction accounts for the fraction of stored muons that do not possess the magic momentum. The storage ring momentum acceptance is $\pm 0.15\%$, which leads to a range of muon momenta around the magic momentum. Thus a range of radii in which the muons circulate the storage ring. The trackers are optimised to measure this muon beam distribution as a function of time. The pitch correction accounts for the vertical angle in the precession plane. Vertical betatron oscillations arise from the fraction of muons whose momenta are not perpendicular to the magnetic field. This means that the muon's spin direction and magnetic field are not aligned, which reduces the rate of precession. Both corrections will be discussed in further detail in Chapter 7. The addition of the tracking stations to E989 will improve these uncertainties as the trackers are placed closer to the beam, so have a higher acceptance. They are also able to turn on sooner in the fill and so can measure the beam for a longer time.

3.3   Muon precession frequencies

The measurement of a_μ utilises the fact that a charged particle with a non-zero magnetic moment experiences a torque in an external magnetic field. This leads to a precession of the particles spin vector about the magnetic field direction at a frequency, ω_s:

$$\omega_s = g\frac{eB}{2m} + (1 - \gamma)\frac{eB}{\gamma m}, \tag{3.5}$$

where γ is the Lorentz factor.

The particle's momentum also changes as it rotates around the storage ring, at the cyclotron frequency, ω_c:

$$\omega_c = \frac{eB}{\gamma m}. \tag{3.6}$$

The difference in these frequencies is called the anomalous spin precession frequency and is denoted by ω_a:

$$\omega_a = g\frac{eB}{2m} + (1 - \gamma)\frac{eB}{\gamma m} - \frac{eB}{\gamma m} = \left(\frac{g}{2} - 1\right)\frac{eB}{m} = \frac{e}{m}a_\mu B. \tag{3.7}$$

From which it can be seen that a_μ is thus determined from a measurement of ω_a and the magnetic field B. ω_a itself can be determined by exploiting the maximal parity violation inherent in muon decay.

3.4   Pion and muon decay

Muons are produced from the parity-violating weak decays of pions. The dominant pion and muon decay Feynman diagrams are shown in Figure 3.7. The dominant decay of the pion is given by

$$\pi^+ \rightarrow \mu^+ \nu_\mu \tag{3.8}$$

and is illustrated in Figure 3.8.

The chiral nature of the weak interaction means that only left-chiral particles or right-chiral antiparticles participate in weak interactions. The pion is a scalar and when it decays at rest, the chiral restrictions and the need to conserve momentum and angular momentum (spin) lead to the μ^+ spin being in the opposite direction to its momentum. The muons from pion decay are thus 100% polarised and this is exploited in the a_μ measurement.

The dominant decay of the muon is also a parity-violating weak interaction:

$$\mu^+ \to e^+ + \nu_e + \bar{\nu}_\mu$$
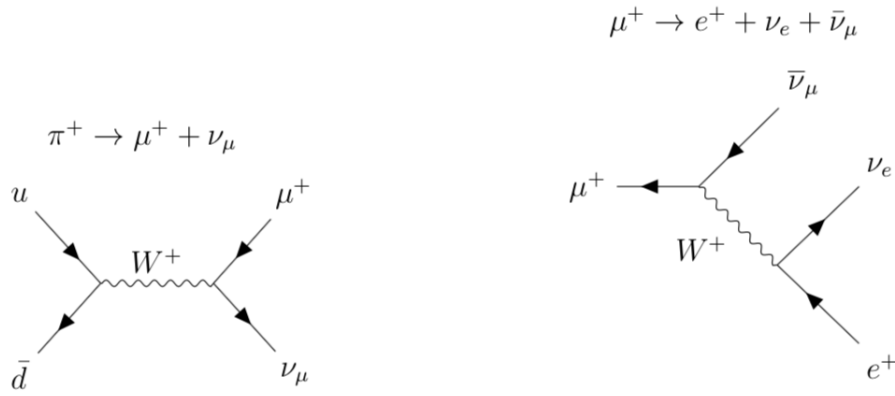
Figure 3.7: Feynman diagrams of the dominant decays of the pion and muon.
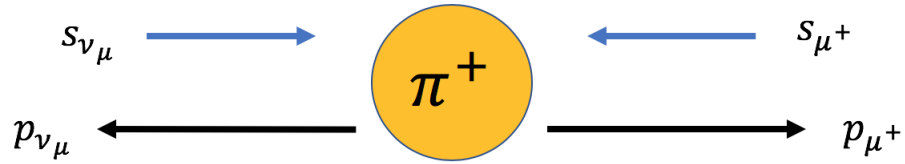
Figure 3.8: A diagram of the parity violating pion decay.

$$\mu^+ \to e^+ \bar{\nu}_\mu \nu_e. \tag{3.9}$$

In muon decay, the positrons have a maximum allowed energy in the muon reference frame (MRF) of $E_{\mathrm{max}} = \frac{m_\mu c^2}{2} = 53\,\mathrm{MeV}$. In these decays, the muon anti-neutrino will be in a right-handed chiral state and the electron neutrino in a left-handed chiral state as shown in Figure 3.9. In the decays emitting the highest energy positrons i.e. those where the positron is in the opposite direction to both neutrinos, the positron's spin vector must be aligned with the muon's spin vector.
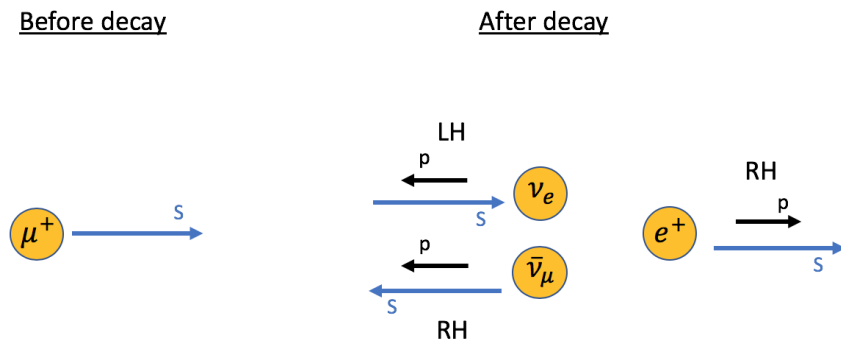
Figure 3.9: A diagram of the parity violating muon decay.

This gives a means to determine the direction of the muon's spin and this is the basis of the ω_a determination. As the muon spin vector precesses, the number of the highest energy positrons emitted is at a maximum when the direction is aligned with the muon spin and a minimum when it is anti-aligned, as shown in Figure 3.10. The number of the highest energy positrons is thus modulated by a $\cos(\omega_a t)$ term, shown in equation 3.10. Experimentally one measures the positrons above a certain energy threshold (E) and in this case, the number of measured positrons varies with time as:
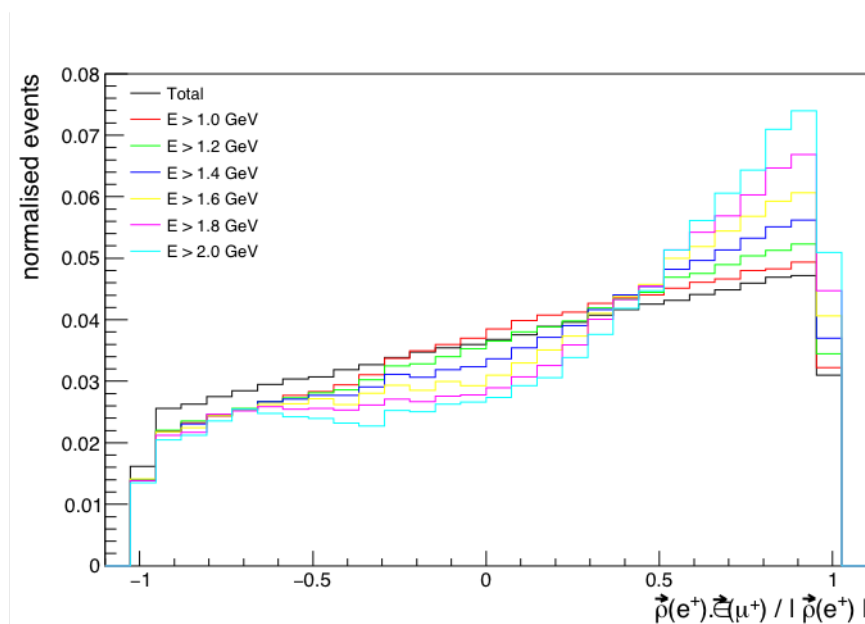
Figure 3.10: A plot of the component of the e^+ momentum along the μ^+ polarisation vector (ϵ) for several energy cuts in the muon rest frame. This displays that at higher energies more positrons have their momenta aligned with their polarisation vector. The asymmetry distribution is calculated by taking away the number of events below zero from the number of events above zero and dividing by the total number of events. The results show that the asymmetry increases as the energy cut is increased [36].

$$N(t) = N_0(E)e^{(-t/\gamma\tau_\mu)}[1 + A(E)\cos(\omega_a t + \phi)], \qquad (3.10)$$

where $N_0(E)$ is a normalisation factor, τ_μ the muon rest frame lifetime, and $A(E)$, the so-called asymmetry distribution, is given by:

$$A(y) = \frac{q}{e}\frac{2y-1}{3-2y}, \tag{3.11}$$

where $y = \frac{E}{E_{\max}}$. A is a maximum when $y = 1$ (highest energy e^+) and a minimum at $y = 0$. A fit to $N(t)$ using Equation 3.10 can thus in principle be used to determine ω_a. However in practice there a number of other effects that modulate $N(t)$ e.g. the acceptance of the detectors as a function of the decay position, the fact that the number of muons decreases by means other than decaying e.g. a muon's orbit around the storage ring is altered by the focussing E-field and variances in the B-field and muons exit the storage ring before decaying. The uncertainty in the determination of ω_a is determined by both $\frac{1}{\sqrt{N}}$ and $\frac{1}{\sqrt{A^2}}$, where A is energy dependent. Therefore to minimise the uncertainty, NA^2 must be maximised. The lowest uncertainty, after accounting for the energy resolution of the detectors and their acceptance, is found to be at an energy cut of $1.9\,\mathrm{GeV}$ as illustrated in Figure 3.11.
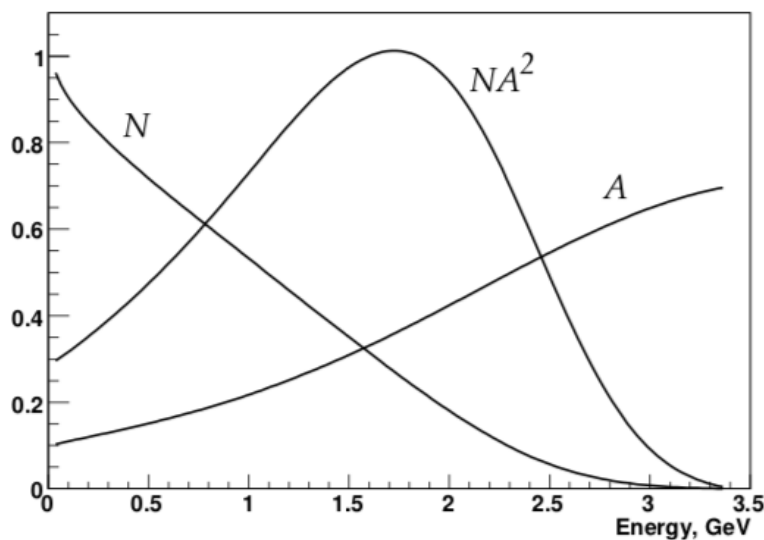
Figure 3.11: A plot of the number distribution (N), the asymmetry function (A) and the statistical figure-of-merit (NA^2) as a function of positron energy with detector acceptance and energy resolution included [2].

The number of positrons recorded as a function of time with energy greater than $1.9\,\mathrm{GeV}$ by the calorimeters of the BNL E821 experiment is shown in Figure 3.12. This illustrates the characteristic $\cos(\omega_a t)$ oscillation and muon exponential decay.
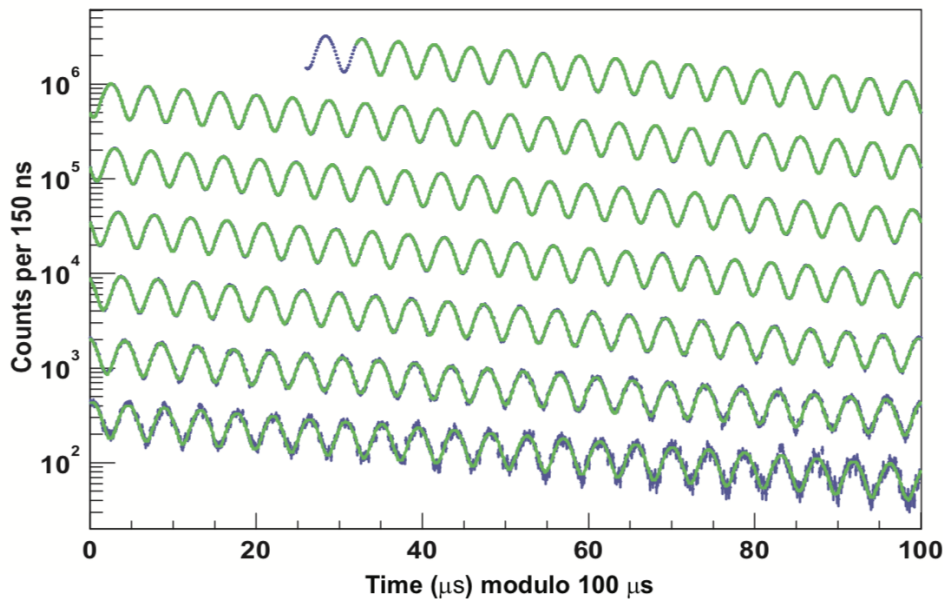
Figure 3.12: Distribution of the decay positrons as a function of time with energy above 1.9 GeV for the BNL 2001 dataset. A total of 3.6×10^9 positrons were used in the fit to determine a value of ω_a [2].

3.5   The magic momentum and the E-field effect on ω_a

Equation 3.7 is for the simple case where the muon is in a uniform B-field. In reality, variances in the B-field and the muons momentum mean that the muon beam diverges vertically and would be quickly lost before a measurement can be made without the application of vertical focussing. The vertical focussing is achieved using electrostatic quadrupoles and this E-field adds an additional term to Equation 3.7:

$$\omega_a = \frac{e}{m}\left[a_\mu B - \left(a_\mu - \frac{1}{\gamma^2-1} \right) \frac{\vec{\beta} \times \vec{E}}{c} \right], \qquad (3.12)$$

arising from the fact that a relativistic particle travelling through an electric field will see a motional magnetic field. It is impossible to measure the E-field to the sub ppm precision required by the a_μ measurement but if γ is 29.3, this second term vanishes and has no contribution to ω_a. Fortunately this corresponds to a momentum, 3.094 GeV/c, readily achievable in a particle accelerator and this momentum has become known as the magic momentum and has been used in the CERN-III, BNL and Fermilab experiments. In reality the muon's have a small variance in momentum around the magic momentum and so there is a small O(200) ppb contribution to ω_a

from this source and a correction is applied to the measured ω_a to account for it: this is commonly known as the "E-field correction".

A further $\vec{\beta} \cdot \vec{B}$ term is required in Equation 3.12 to account for the fact that the muon's momentum is not completely orthogonal to the B-field:

$$\omega_a = \frac{e}{m} \left[a_\mu B - \left(a_\mu - \frac{1}{\gamma^2 - 1} \right) \frac{\vec{\beta} \times \vec{E}}{c} - a_\mu \left(\frac{\gamma}{\gamma + 1} \right) (\vec{\beta} \cdot \vec{B}) \beta \right]. \tag{3.13}$$

The B-field is not perfectly vertical and the muon's momentum is not entirely constrained in the horizontal plane i.e. the beam has a small vertical momentum and the muons undergo vertical betatron oscillations. A O(200) ppb correction must be applied to the measured ω_a to correct for this: this is commonly known as the "pitch correction" and this is discussed in detail in chapter 7 since it is determined by measurements of the vertical beam motion by the straw tracking detectors.

3.6 Determining ω_p

The magnetic field, B, is determined by a measurement of the free proton Larmor precession frequency, ω_p, using NMR which is related to B via:

$$\omega_p = 2\mu_p B, \tag{3.14}$$

where μ_p is the proton magnetic moment. This is achieved using three separate systems. A trolley is equipped with 17 NMR probes and traverses the storage ring every 2–3 days, when muons are not circulating, to measure the field in the region that the muons are stored. 378 fixed NMR probes are mounted at the top and bottom of the storage ring vacuum chambers and measure the field continually. Finally a third set of so-called "plunging probes" are used to make measurements at both the trolley location and the fixed probe location to allow an interpolation between the continual fixed probe readings and the intermittent trolley measurements. The straw tracking detectors measure the beam profile and this is convoluted with the magnetic field map to determine the magnetic field experienced by the stored muons.

3.7 a_μ calculation

Combing Equation 3.7 relating ω_a to a_μ and Equation 3.14 relating ω_p to B yields:

$$a_\mu = \frac{2m_\mu \mu_p}{e} \frac{\omega_a}{\omega_p}.$$ (3.15)

Equation 3.15 can be written in terms of ratios of quantities that are extremely precisely determined. Using

$$\mu_e = \frac{g_e e}{4m_e},$$ (3.16)

one obtains:

$$a_\mu = \frac{g_e}{2} \frac{m_\mu}{m_e} \frac{\mu_p}{\mu_e} \frac{\omega_a}{\omega_p}.$$ (3.17)

g_e i.e. a_e has been measured to 0.3 ppt accuracy [11] and the ratios $\frac{m_\mu}{m_e}$ and $\frac{\mu_p}{\mu_e}$ have both been determined from the E1054 LAMPF measurement of the muonium Zeeman ground state hyperfine transitions to a precision of 22 ppb and 3 ppb respectively [48, 49] and this precision will be improved further by the J-PARC MuSEUM experiment. It is evident that the dominant uncertainty in a_μ arises from the measurements of ω_a and ω_p.

Chapter 4

The Fermilab Muon g-2 experiment

4.1 The Fermilab Muon g-2 experiment

In this chapter a description of the muon beam preparation and its delivery into the storage ring will be given alongside a description of the major components of the g–2 experiment. The tracking detectors will be discussed briefly here and described in detail in chapter 5.

4.2 Production and preparation of the muon beam

The accelerator complex at Fermilab was reconfigured in 2011–2016 to produce a high quality muon beam in addition to the neutrino beams for the short and long baseline neutrino experiments. The relevant parts of the complex are shown in Figure 4.1. The process of creating muon bunches starts with the booster. This increases the energy of 400 MeV protons from the linac into bunches of 8 GeV protons. Within the booster, for each 1.33 s cycle of the accelerator, four bunches of 8 GeV protons are produced. These are then injected into the Recycler ring through the Main Injector (MI) line. Here each bunch is further divided into four. These sub-bunches contain $\sim$ 10^{12} protons and must have a temporal length shorter than the cyclotron frequency of 149 ns. The compacted sub-bunches are concentrated at the beginning of the MI cycle and separated by 10 ms, meaning only one bunch of muons is injected into

the storage ring and measured by the detectors at a time, which allows sufficient time for the g–2 experiment data acquisition system to process the data between the injection of successive bunches, known as muon fills or spills. The average fill rate is approximately 12 Hz. Figure 4.2 shows the structure of the proton beam pulses [50].
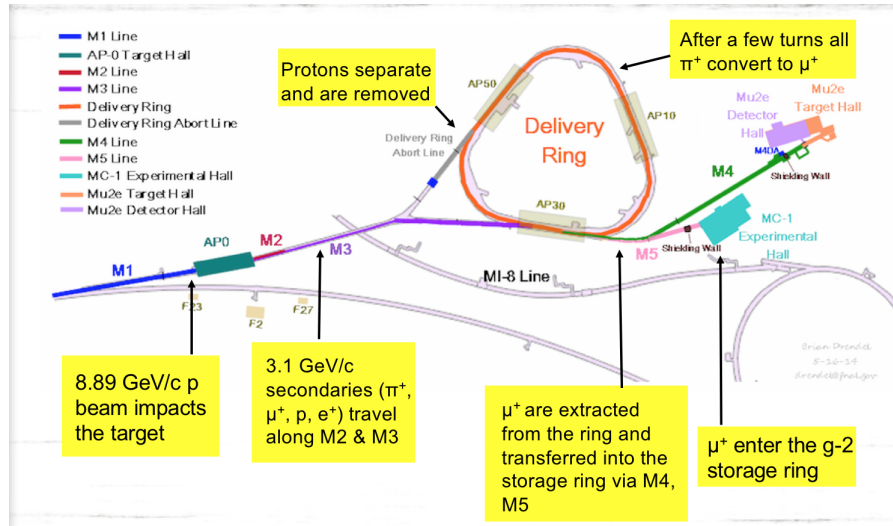
Figure 4.1: The components of the Fermilab accelerator complex producing the muon bunches for the g–2 experiment [2].
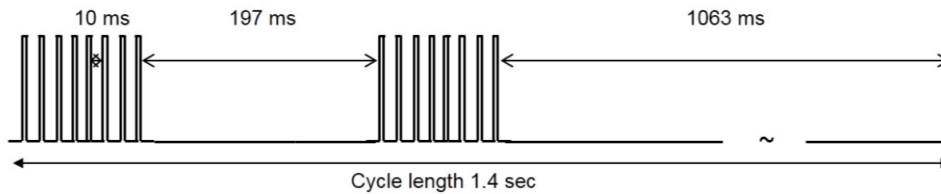
Figure 4.2: Time structure of the proton bunches used by the g–2 experiment [2].

The bunches are then directed separately through the P1, P2 and M1 lines and directed at the Target station which is located in the AP0 hall. Each bunch of 8 GeV protons are fired separately at the pion production target, with the beam parameters at this position shown in Table 4.1. The positively charged particles produced are momentum selected to $3.11 \pm 0.3 \, \mathrm{GeV/c}$ using a pulsed dipole magnet and collimator system. The beam is then directed through the M1 and M2 lines which select muons produced from the pion decays with a momentum of 3.094 ± 0.3 GeV/c. Particles that are not momentum selected will continue forward and are absorbed by a beam dump [51]. Table 4.2 shows the number of secondary particles

remaining after momentum selection.

Parameter	FNAL $(g-2)$ 12 Hz
Intensity per pulse	10^{12} p
Total POT per cycle	16×10^{12} p
Number of pulses per cycle	16
Cycle length	1.33 s
Primary energy	8.89 GeV
Secondary energy	3.1 GeV
Beam power at target	17.2 kW
Beam size σ at target	0.15-0.30 mm
Selected particle	π^+
$\lvert dp/p \rvert$ (PMAG selection)	10%

Table 4.1: Beam parameters at the Target station [2].

Beam Type	Particle Species	Beam Momentum (GeV/c)	Number of Particles per pulse
Primary protons	p	8.9	10^{12}
Mixed secondaries	μ^+, π^+, p, e^+	3.1	10^7 to 2×10^8
Proton secondaries	p	3.1	10^7
Muons	μ^+	3.1	$< 10^5$

Table 4.2: A table showing the expected properties of the primary proton beam, the secondary beam created by the target and the muon beam from pion decay. [2].

The remaining muons are directed into the delivery ring along with any remaining protons and pions. The beam circulates around the delivery ring four times, by which time all of the pions will have decayed. Any remaining protons are removed by a kicker since they travel slower than the muons and become separated from the muon bunch. This produces a very pure, polarised muon beam. The beam is then guided into the M4/M5 beamline to the MC1 experimental hall. Here final focusing is provided by magnetic quadrupoles before the muon beam enters the storage ring through the inflector [2].

4.3   Injection into the storage ring

The polarised muon beam is injected into the storage ring as shown in Figure 4.3. To do this it must pass through the storage ring magnetic field. However doing this would deflect the path of the muons, causing them to exit the storage ring. To counteract this effect, the inflector which is a 1.7 m superconducting magnet is
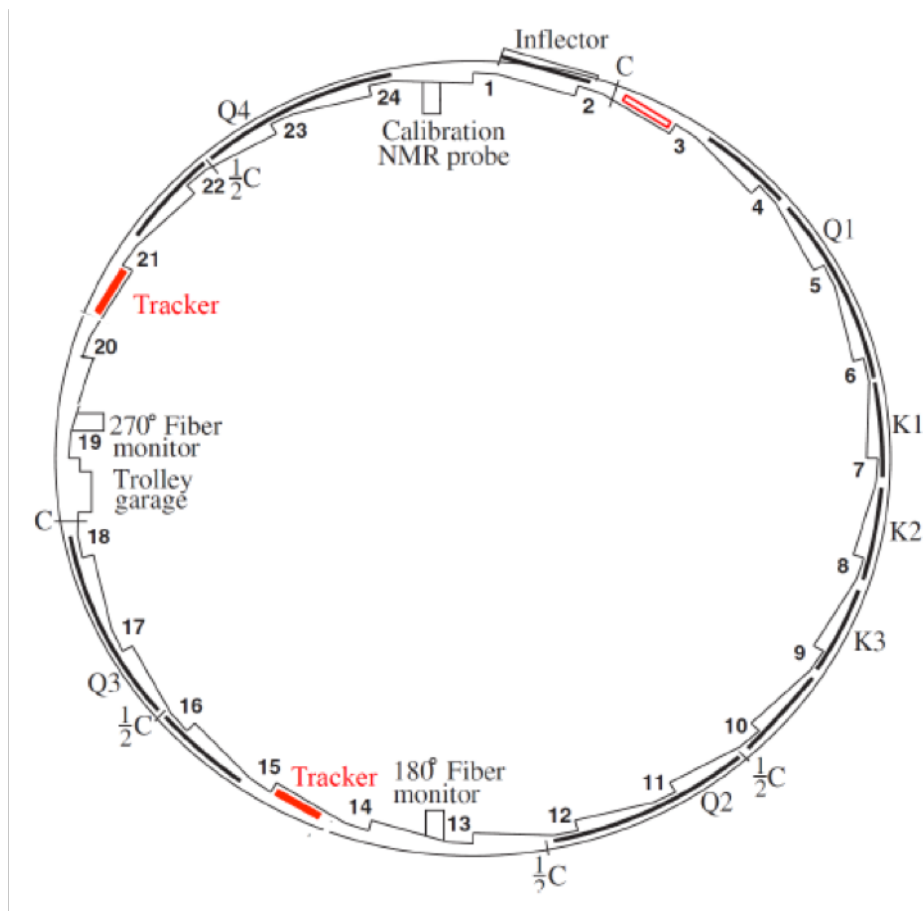
Figure 4.3: Diagram of the storage ring and its main components. The kicker positions indicated by a "K", the collimators with a "C", the quadrupole positions with a "Q",the tracking stations placed at 180° and 270° and the 24 calorimeter locations around the ring [26].

placed at the point of injection to create an almost magnetic-field-free region. The inflector makes a 1.45 T uniform vertical field which acts to cancel out the magnetic field in the injection channel and allows the muon beam to pass into the storage ring unperturbed. The inflector was constructed such that its own magnetic field does not affect the magnetic field in the region where the muons ultimately circulate.

Muons are delivered into the storage ring in 120 ns pulses at an average rate of 12 Hz. Each muon bunch forms one fill of approximately 5,000 muons. The beam line leading to the inflector is positioned at a 1.25° angle from the tangential direction to allow the beam to enter the inflector almost parallel to it. A layout of this is shown in Figure 4.4. The position at which the beam enters the storage ring through the inflector is at a circumference 77 mm radially larger than the equilibrium radius for
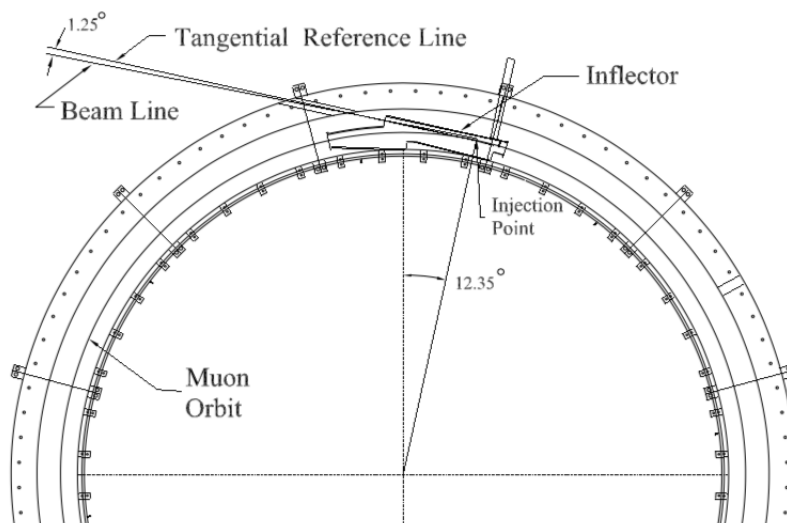
Figure 4.4: Diagram of the beam entering the storage ring [26].

the magic momentum of 3.094 GeV/c.

To direct the muon bunches onto the ideal, equilibrium radius, a device called the kicker system is used. The kicker system comprises three independent 1.27 m long plate magnets. This system is placed at approximately 90° around the ring after the injection point, at the position where the muons orbit intersects with the ideal radius. The kicker provides 0.03 T pulses to centre the beam. These pulses last the entire bunch width of 120 ns to create a 10.8 mrad angular kick that directs the muons onto the ideal orbit. To avoid a second kick perturbing the orbit, the kicker pulse must return to zero before the bunch returns to the same position a cyclotron period later.

The kicker device resides within the precision magnetic field. Consequently the kicker cannot consist of any magnetic materials which would subsequently perturb the magnetic field. The kicker does not direct all muons exactly onto the ideal radius as there is a small momentum spread in the muon beam which results in a variance in the beam distribution.

Electrostatic quadrupoles are used to vertically focus the beam. Four electrostatic quadrupoles are placed symmetrically around the ring to produce four separate regions of focusing. In an ideal situation the electrostatic quadrupoles would be placed throughout the whole ring circumference but space occupied by the inflector, kickers

and tracking detectors means that only 43% of the ring circumference is equipped with quadrupoles.

Electrostatic quadrupoles were chosen for vertical focusing rather than magnetic quadrupoles in order to not perturb the storage ring magnetic field. The quadrupole field acts to focus the beam vertically while defocussing the stored beam radially. However the combined effect of the electric field and the vertical storage ring magnetic field provides radial focusing. This leads the storage ring to behave as a weak focusing betatron.

There are collimators placed around the storage ring. These are copper rings with an inner radius of 45 mm which are used to remove muons which lie outside the 9 cm diameter muon storage region. The collimators are rotated away during the periods when the NMR trolley is measuring the magnetic field in the storage region. After injection, the electrostatic quadrupole plates are charged asymmetrically which moves the beam horizontally and vertically to direct the muons outside of the core distribution towards the collimators where they lose energy and are lost after several orbits. This process is called scraping. It begins at $8\,\mu s$ after beam injection and continues for $5\,\mu s$. Once scraping is completed, the quadrupole plates are charged symmetrically to enable the vertical focussing. The removal of the muons lying at the extremities results in a reduction in the momentum spread of the stored beam to 0.15% (5 MeV/c).

Once the muon beam has been successfully stored, its beam motion exhibits several measurable frequencies. These frequencies are introduced below and will be discussed in more depth in Chapter 7. Table 4.3 displays the parameter values of these frequencies from a subset of Run-1 data corresponding to a quadrupole voltage of 18.3 kV. The observed frequencies are:

- The muon g–2 precession frequency: Is the frequency at which the muon spin vector precesses relative to the momentum vector.

- The cyclotron frequency: Is time it takes for a muon to travel once around the storage ring.

- Horizontal and vertical betatron oscillations: The electrostatic quadrupoles provide a linear restoring force in the vertical direction. The combination of the

storage ring vertical magnetic field and the radial electric fields causes a linear restoring force in the radial direction. These forces cause the muons to undergo simple harmonic motion (SHM) in the horizontal and vertical directions, causing them to oscillate periodically about their stored orbits horizontally and vertically.

- Coherent betatron oscillations (CBO): This frequency is the beat frequency between the cyclotron frequency and the horizontal betatron frequency.

- Vertical waist frequency: The oscillation of the vertical width of the muon beam.

Muon Beam Frequencies				
Name	Symbol	Expression	Frequency (MHz)	Period
$g-2$	f_a	$a_\mu Be/2\pi mc$	0.23	$4.365\,\mu s$
cyclotron	f_c	$v/\pi R_0$	6.71	$149.2\,ns$
horizontal betatron	$f_{x_{BO}}$	$\sqrt{1-n}f_c$	6.34	$158\,ns$
vertical betatron	$f_{y_{BO}}$	$\sqrt{n}f_c$	2.21	$452\,ns$
coherent betatron	f_{CBO}	$f_c - f_{x_{BO}}$	0.37	$2.703\,\mu s$
vertical waist	f_{VW}	$f_c - 2f_{y_{BO}}$	2.31	$433\,ns$

Table 4.3: A table of frequencies observed in the g–2 experiment due to beam motion from a subset of Run 1 corresponding to a quadrupole voltage of $18.3\,kV$ [52].

4.4   Muon decay in the storage ring

For a muon traversing the storage ring at the magic momentum, its time dilated lifetime increases from a rest lifetime of $2.2\,\mu s$ to $64\,\mu s$. This means the muons circulate the storage ring many times before their decay and the lifetime is long enough for the observation of multiple periods of ω_a which has a time period of $4.4\,\mu s$.

The decay positrons are Lorentz boosted and are emitted predominantly along the muon momentum direction. The high energy decay positrons observed by the detectors are emitted within 2% of the muon's momentum direction. During muon decay, energy is lost to neutrinos and thus the decay positron has a lower momentum than the muon. Therefore the positron has a more curved trajectory in the magnetic field

at a smaller radius compared to the muon. Hence the positron's path will be inwards towards the centre of the storage ring, where the detectors are located to measure them. Data is recorded in the detectors for approximately $650\,\mu$s, by which time the majority of muons will have decayed.

4.5 The magnetic storage ring
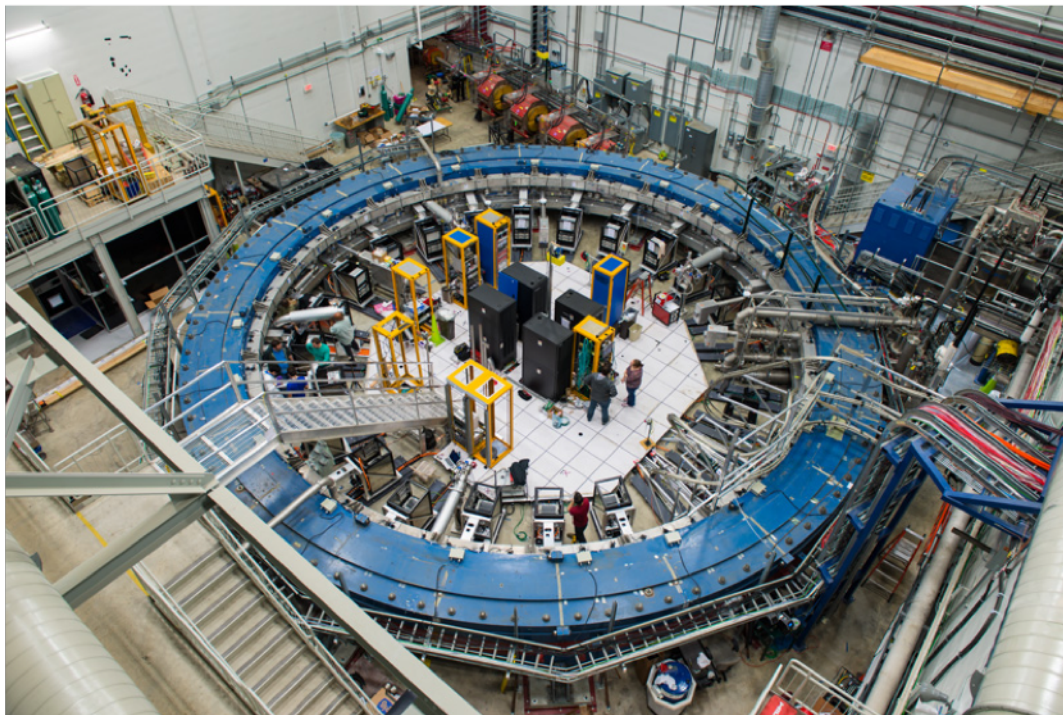
Figure 4.5: Photograph of the muon g–2 storage ring which reuses the BNL 1.45 T storage ring [2].

The determination of a_μ requires a precise measurement of the magnetic field convoluted with the muon beam distribution, along with a precise measurement of ω_a. The goal of the Fermilab E989 experiment is to determine the magnetic field averaged over time in the beam storage region to an uncertainty of $\pm 70\,$ppb, an improvement from the 170 ppb at BNL [2]. The experiment reuses the magnetic storage ring originally designed and constructed for the BNL muon g–2 experiment, as seen in Figure 4.5. The 15 m diameter superconducting coils required specialist transportation and were shipped from BNL to Fermilab in one piece. Other components including the pole pieces and steel yoke were separated and transported individually to be reassembled at Fermilab [2]. A photograph of the muon g–2 magnet is shown in Figure 4.6.
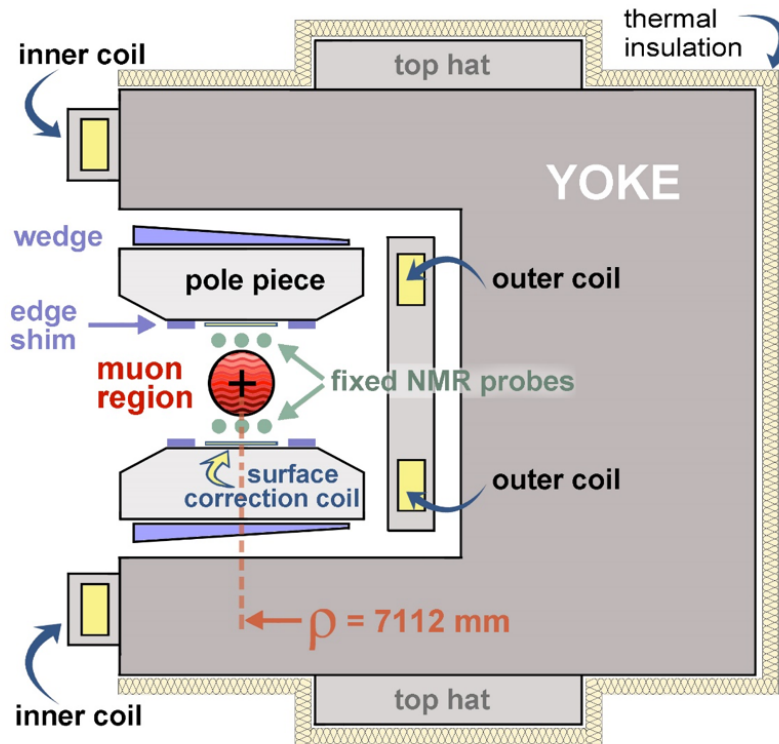
g-2 Magnet in Cross Section

Figure 4.6: The cross section of the storage ring, showing the location of the muon storage region and the fixed NMR probes. It also shows the superconducting magnet components including the yoke, coils and pole pieces [53].

The iron dipole magnet is designed to produce a vertical uniform field of 1.45 T, with a uniformity of 1 ppm when averaged over the full azimuth of the storage ring. The magnet's yoke is constructed from a dozen 30° sections of iron. Each section contains an upper and lower yoke which are separated by a spacer plate. The storage ring is approximately 3 m tall, 15 m in diameter, weighs over 700 tons and has an ideal muon storage radius of 7.112 m.

The 5176 A current for the dipole magnet is carried by three superconducting niobium-titanium (NbTi) coils placed above and below the storage region [53]. Iron pole pieces are placed in between the superconducting coils to create the uniform dipole field. A cryogenic system is used to cool the superconducting coils to the required temperature. The inner superconducting coils sit at a radius of 6677 mm and the outer coils are at 7512 mm. The current in the outer coil is twice the current in the inner coils to maintain a constant field. The current to the inner and outer coils is supplied in

opposite directions to produce the vertical magnetic field in the region between them. The iron yoke is designed as a C-shape structure located at the top and bottom of the storage ring and on the outer radius.

The uniformity of the magnetic field has been greatly improved compared with the BNL experiment due to improvements in the "shimming". Shimming is the process by which the magnetic field is made more homogeneous. Over 1,000 steel shims are introduced at several different positions to provide localised fine adjustments to improve the magnetic field uniformity [54].

Two types of shimming are used: passive and active. Passive shimming is achieved through the 1,000 fixed steel shims while active shimming uses current-carrying coils on the surface of the pole pieces. The currents in the so-called surface correction coils can be adjusted to improve the field homogeneity [55, 43].

4.6   Magnetic field measurement detectors

Precision measurements of the magnetic field to the required precision are carried out using pulsed proton NMR (pNMR) probes containing petroleum jelly or water. A $\frac{\pi}{2}$ RF pulse is used to rotate the proton spin and the resulting free induction decay (FID) is detected by a pick-up coil from which the magnetic field can be determined. The fixed probe system is designed to continuously measure the field during data taking. It comprises 378 NMR probes placed at 72 positions above and below the beam storage region volume throughout the storage ring. The field mapping trolley contains 17 cylindrical probes placed on its front face and arranged in concentric circles. This is shown in Figure 4.7. Every 2–3 days during data taking periods the beam is stopped for a few hours to allow the trolley to map the field in the storage region. A bar code reader on the trolley scans bar codes on the walls of the vacuum chamber to accurately determine the trolley's position while it is mapping the field. The magnetic field measurement is determined in terms of the free proton Larmor precession frequency ω_p. However, the protons in the pNMR probes are in hydrocarbon or water molecules and co-located with other materials and as such are not free protons. This means that the proton experiences a perturbed magnetic field. An absolute calibration is required to make corrections for these perturbations. This
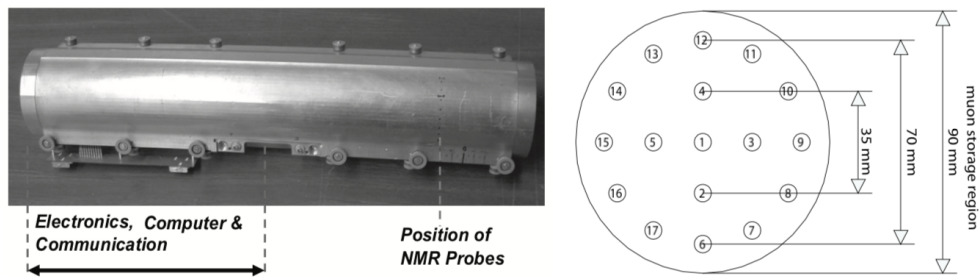
Figure 4.7: On the left a photograph of the trolley used to measure the magnetic field in the muon storage region. On the right the layout of the 17 NMR probes in the trolley face [2].

correlates the measured magnetic field with the Larmor precession frequency of a free proton and must be done for each trolley probe at every location it measures. This is carried out using two NMR probes; the absolute calibration probe and the plunging probe. The absolute calibration probe measures the field at the same position as the central trolley probe. This can then be cross calibrated with the plunging probe which also measures the field in the muon storage region [2].

4.7   Detector systems

4.7.1   Calorimeters

The primary physics goal of the calorimeter is to measure the energy and time of the positrons from the muon decays so that ω_a can be determined. After a muon decays, the positron has insufficient energy to continue its trajectory around the ideal radius and it curls inwards and is incident on a calorimeter.

The experiment's calorimeter system contains 24 calorimeter stations equally spaced on the inside radius of the magnetic storage ring [2]. Each of these calorimeters is made up of 54 Lead Fluoride (PbF$_2$) crystals distributed in an array of 6 crystals high and 9 crystals wide. A photograph of the calorimeter crystals being installed is shown in Figure 4.8. PbF$_2$ crystals were selected due to their fast Cerenkov light signal and good energy resolution. Each crystal is 255 mm wide, 25 mm tall and 140 mm deep [56].

Decay positrons produce particle showers in the crystals and Cerenkov light passes
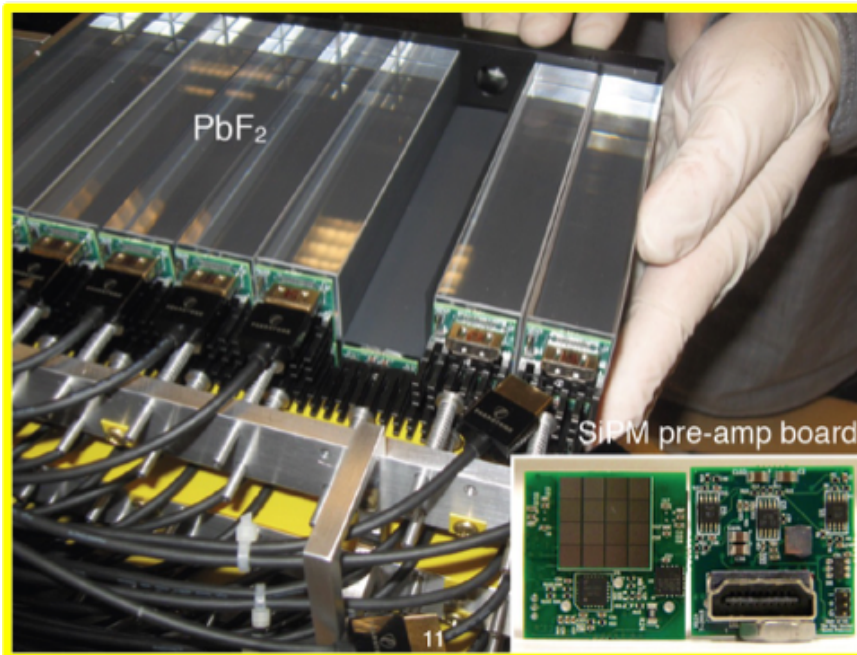
Figure 4.8: Photograph of calorimeter crystals being installed [56].

downstream through the crystal and is detected and readout at the edge of the crystal by a silicon photo multiplier (SiPM). Each crystal is separately wrapped in highly reflective Millipore paper to prevent Cerenkov light passing into neighbouring crystals. SiPM detectors act as pixelated proportional counters and quenching resistors suppress the avalanche such that the pixels can operate at rates of $O(10\,\mathrm{MHz})$. The calorimeter is required to:

- Have an energy resolution of better than 5% for positron energies greater than $2\,\mathrm{GeV}$.

- A time resolution of less than $100\,\mathrm{ps}$ for a given SiPM pixel.

- A 100% efficiency for temporally resolving two showers with a separation of greater than $5\,\mathrm{ns}$ and the ability to resolve 66% of showers separated by less than $5\,\mathrm{ns}$ [2].

A laser calibration system is used to monitor and calibrate the gain variation of each crystal and SiPM [57, 58]. To do this, laser pulses are continually fired to each calorimeter during and between muon fills. This enables the monitoring of both short-term and long-term gain changes e.g. due to temperature variations.

4.7.2   Fiber beam monitors

The fiber beam monitors are constructed from scintillating fibers. These detectors provide a destructive measurement of the stored muon beam distribution and are utilised in dedicated systematic study runs. They can be pneumatically inserted into and retracted from the storage region when required.
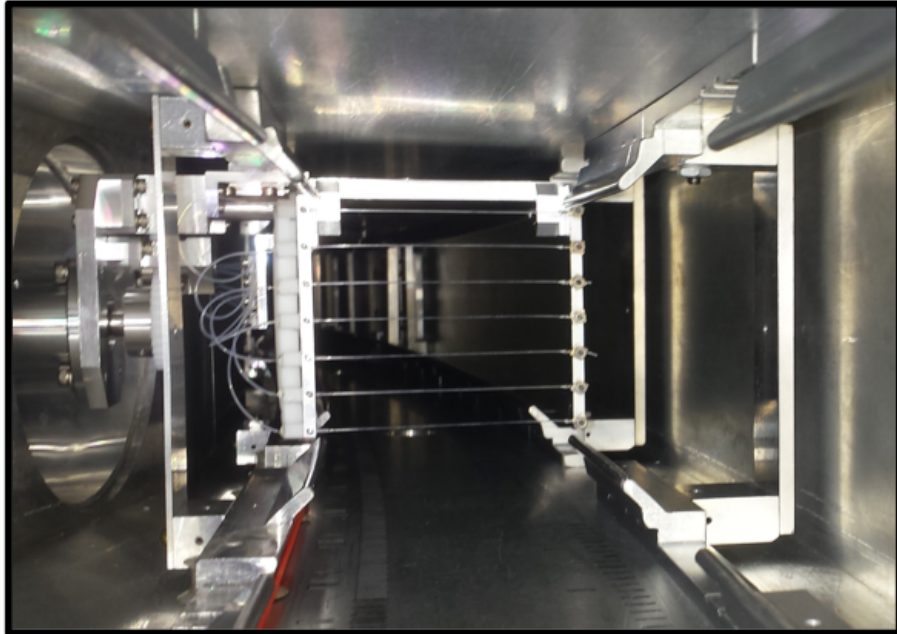
Figure 4.9: Photograph of a fiber beam monitor in the muon beam storage region [2].

Each fiber beam monitor contains seven scintillating fibers which are 90 mm long, 0.5 mm in diameter and separated by 13 mm to create a harp like structure. There are four fiber monitors: two placed at $180°$ and two at $270°$. At both locations, one detector is orientated so that its fibers are vertical and the other horizontal to measure both the radial and vertical beam profiles. A photograph of a fiber beam monitor is shown in Figure 4.9. The detectors can also be rotated horizontally enabling a cross calibration of the fibers [59].

4.7.3   Straw tracking detectors

The straw tracking detectors are designed to make non-destructive measurements of the stored muon beam profile throughout the duration of each muon fill by measuring the decay positrons. Two tracking stations are placed at $180°$ and $270°$ around the inside of the ring, each directly upstream of a calorimeter. At these locations around

the ring, when a decay positron travels inwards to the centre of the storage ring it can pass through straw tracker modules. The positrons pass through the individual straws ionising the gas and creating a pulse, then travel onward to be detected by a calorimeter. Trajectories of the positron's path can then be made by fitting the individual straw hits and this can be extrapolated back to the point of the muon decay. From this the muon beam profile can be constructed. A detailed description of the straw trackers will be given in chapter 5.

4.7.4   Inflector beam monitoring system

The inflector beam monitoring system (IBMS) is used to determine the muon beam distribution at the point of injection into the storage ring. It continuously measures the time the beam enters the storage ring, the intensity of the beam and its xy profile. Examples of which are shown in Figures 4.10 and 4.11. This information is used to optimise the injection beam optics and thus to maximise the number of muons circulating the storage ring.

The IBMS comprises two detectors positioned upstream of the storage ring: one upstream of the inflector and one downstream. These detectors are made from scintillating fibers which are readout by SiPMs [2, 60].

There is also a scintillator detector called the T0-counter. This is placed at the entrance to the storage ring to record the injection time of a fill (t_0). The T0-counter shares the same clock as the other detectors and is used to set the injection time for all of the detectors: $t = 0$ is defined as the time the T0-counter records the first pulse in a fill. An example of a waveform recorded by the T0-counter is shown in Figure 4.12.
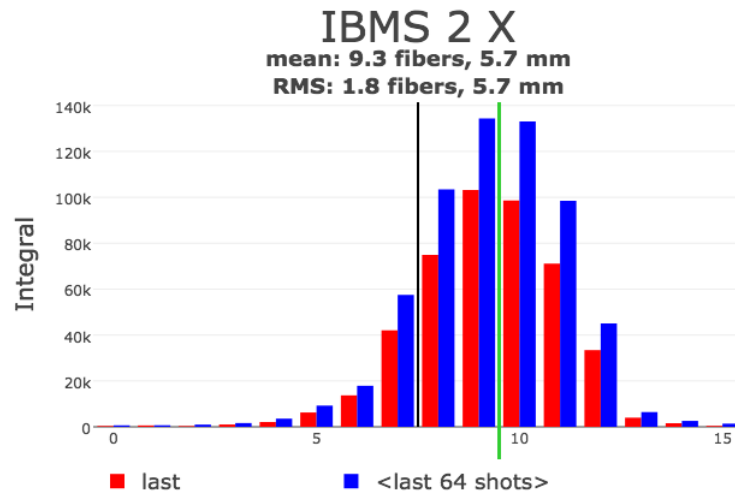
Figure 4.10: An online monitoring plot of the x profile of the beam seen by an IBMS detector.
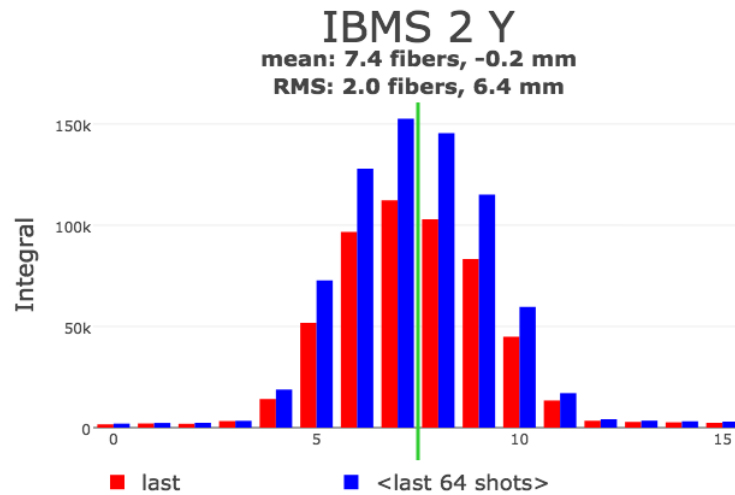
Figure 4.11: An online monitoring plot of the y profile of the beam seen by an IBMS detector. This gives us information about the beam entering the storage ring. By comparing the x and y profiles of the beam that last entered the storage ring to the average of the last 64, the variation in the beam is observed. This sort of variation is acceptable as only 2% of the beam ends up being stored.
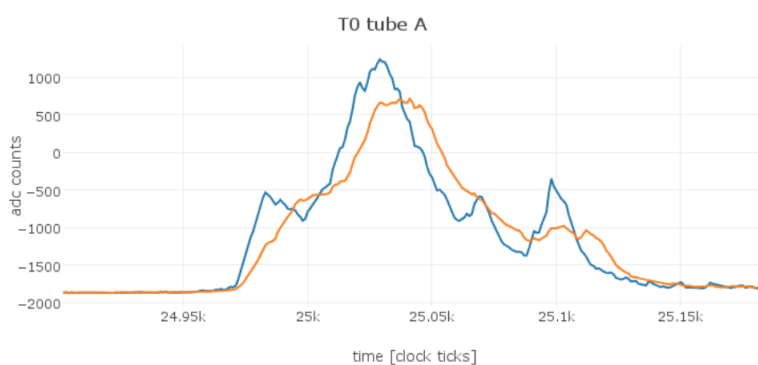
Figure 4.12: An online monitoring plot displaying a T0 waveform. The orange line shows the average of the last 4 fills and the blue line shows the waveform from the previous fill. A clock tick is 1.25 ns. This shows a single pulse compared to the average and there are 16 distinct but similar shapes that are seen due to the structure of the beam.

Chapter 5

Straw tracking detectors

The rest of this thesis will concentrate on the straw tracking detectors. This chapter will discuss the physics goals, design and operating principles of the straw tracking detectors. Chapter 6 will describe the construction and testing procedures of the straw tracking detectors, built at the University of Liverpool, which formed a major part of the first two and a half years of my PhD. Chapter 7 will discuss a detailed study of the vertical motion of the beam using the straw tracking detector data. This study was used to provide an important correction applied to the data before a_μ can be determined.

5.1 Tracker goals and requirements

The primary function of the straw tracking detectors is to measure the trajectory of the positrons originating from the decay of the muons circulating in the storage ring. This is used to determine the point of decay and thus to build up a profile of the muon beam as a function of time. The beam's profile as a function of time is required to determine the O(200 ppb) corrections arising from the variance in the beam's momentum (E-field correction) and the momentum not being entirely orthogonal to the magnetic field (pitch correction). The latter correction, determined by data from the straw trackers, is discussed in detail in chapter 7. The beam distribution must be known precisely since the muon distribution has to be convoluted with the magnetic field map in order to determine the field experienced by the muons measured in the determination of ω_a. The magnetic dipole field is not uniform due to higher order

multipole terms arising from imperfections in the shimming.

The secondary purpose of the straw trackers is to determine and minimise the systematic uncertainties on the determination of ω_a from the calorimeter data. Tracks in the straw tracking detectors can be matched to energy clusters in the calorimeter. The momentum of a track can be compared to the energy of isolated clusters to provide an independent cross check of the calorimeter's energy calibration. Multiple tracks extrapolated to the same calorimeter cluster can be used to identify "pileup" events, whereby two positrons overlapping spatially and temporally are reconstructed in the calorimeter as a single positron. This biases the determination of ω_a since two lower energy positrons are then identified as a single higher energy positron. The correlation of the positron's energy with the muon's spin direction depends on the positron's energy and hence an erroneous determination of the energy though "pileup" systematically shifts the value of ω_a. A reliable determination of the pileup is vital in order to provide an energy-dependent correction to the number of measured positrons before the number of positrons is fitted as a function of time to determine ω_a. A comparison of track momentum (p) to the energy (E) of the calorimeter cluster can also be used to identify muons that leave the storage ring before they decay: so-called "lost muons". Muons, as minimum ionising particles, are characterised by a low value of E/p. These muons are ones that have, over repeated revolutions of the storage ring, lost sufficient momentum e.g. by moving through the quadrupoles, to no longer be constrained within the storage ring and then leave the storage ring and pass through several calorimeters. E/p measurements can be used to identify the rate of the lost muons and to cross-check the determination of their rate from the multiple-calorimeter signature and the determination from simulation [64]. Table 5.1 lists the goals for the systematic uncertainties measured using the tracking detectors.

5.2   Design

The straw tracking stations consist of 8 identical tracking modules which are placed in close proximity to each other. There are two tracking stations situated at 180° (station 1) and 270° (station 2) around the storage ring. These are installed inside

Uncertainty	E821 value	E989 goal	Role of tracking
Magnetic field seen by muons	0.03 ppm	0.01 ppm	Measure beam profile on a fill by fill basis
Pitch correction	0.05 ppm	0.03 ppm	Measure beam oscillation parameters as a function of time in the fill
Pileup correction	0.08 ppm	0.04 ppm	Isolate time windows with more than one positron hitting the calorimeter to verify calorimeter based pileup correction
Calorimeter gain stability	0.12 ppm	0.02 ppm	Cross check laser E calibration with E/p
Precession plane tilt	4.4 μRad	0.4 μRad	Measure up-down asymmetry in positron decay angle

Table 5.1: Systematic uncertainty goals for the Fermilab muon g–2 experiment and the role of tracking required to meet these aims [2].

the vacuum chambers in order to minimise the multiple scattering of particles prior to the trackers and are placed directly in front of a calorimeter. Each tracking module is constructed from two aluminium manifolds (top and bottom manifolds) fixed in place by an aluminium flange. These are both shown in Figures 5.1 and 5.2 respectively. The manifolds contain 128 identically drilled holes to hold in place 128 aluminised Mylar straws. The manifolds also contain the frontend readout electronics, high-voltage (HV) distribution boards and enable the supply of gas to the straws. The straws are arranged in the manifolds in four rows of 32 straws. Two adjoining rows of straws are called the V layers which are at an angle of $+7.5°$ with respect to the vertical plane. The other two adjoining rows are called the U layers and are at an angle of $-7.5°$ with respect to the vertical plane. This stereo-angle of the straw layers enables the vertical height of the incoming positron tracks to be calculated. An aluminium tube called a snout connects to each manifold. The snouts house the flexi cables and feedthrough boards which connects to the secondary electronics in the Frontend Low voltage Optical Box to BackEnd Readout (FLOBBER). Once the manifolds have been populated with the frontend electronics, they are sealed with a

lid and a greased o-ring to form the vacuum seal. A picture of a completed tracking module is shown in Figure 5.3. The trackers are required to measure the vertical and radial beam distributions to a high accuracy. To achieve this a resolution of approximately $100\,\mu$m per position measurement in the radial direction is required. The requirements on the vertical axis are far less stringent as there is no curvature of the tracks in the vertical direction.
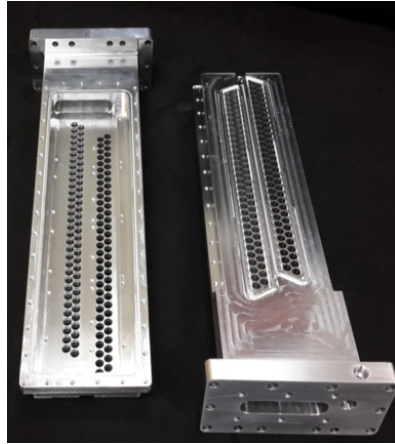
Figure 5.1: Photograph of two aluminium manifolds used in the construction of a straw tracking module.
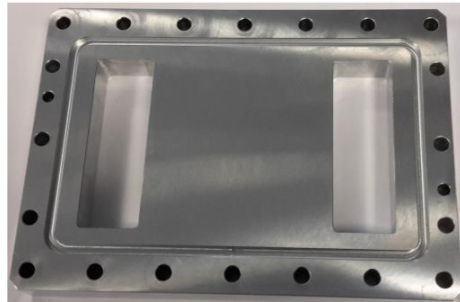
Figure 5.2: Photograph of a flange used in the construction of a straw tracking module.

Circular straws, able to withstand a small differential pressure in vacuum despite their small wall thickness, are used in each module. The Mylar straws are $90.6\,$mm in length and $5\,$mm in diameter. The straws are made up of two layers of $6\,\mu m$ Mylar wound in a spiral with a $3\,\mu m$ layer of adhesive glue between them. The inner wall of the straw acts as a cathode layer and is coated with $500\,\mathring{A}$ of aluminium overlaid with $200\,\mathring{A}$ of gold. The outer layer has $500\,\mathring{A}$ of aluminium which provides additional electrostatic shielding and also helps to reduce the leakage of gas from

the straws [2]. The modules are made purely of non-magnetic materials. This is to ensure that the precise magnetic field is not distorted by the tracking modules.
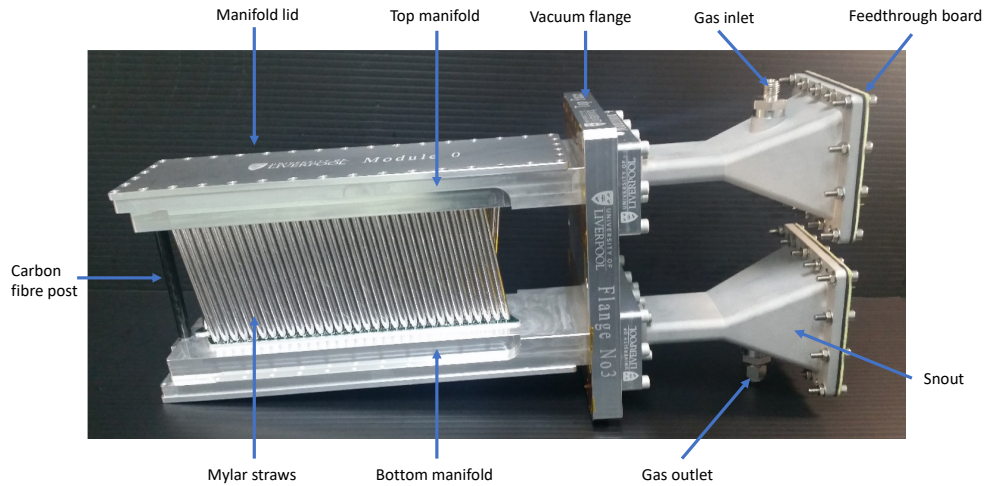
Figure 5.3: A photograph of a straw tracking detector labelling its key components.

At the centre of each straw is a $25\,\mu$m gold-plated tungsten wire. These are secured in place at each end by gold-plated copper pins. There are two different lengths of pins. The long pins at one end are used as the electrical connection with the manifold electronics. The short pins on the opposite end do not connect to the manifold electronics and have insulating end caps placed over them to prevent electrical discharges.

5.3   Operating principles

The straws in the tracking detectors behave as individual drift chambers. When positrons travel through the straw they interact with the gas molecules distributed within the straw. This interaction ionises the gas molecules causing the emission of one or more electrons. This occurs at random as the positron passes through the straw. The interaction of the positron and the molecule is called a primary ionisation. The group of electrons that are ejected from this interaction are called a cluster, with the individual electrons called primary electrons. Further ionisations through interactions of the gas with the primary electrons produces secondary electrons [61]. The gas in the straw tubes is a 50:50 argon–ethane mixture. This gas mixture is

flowed through gas inlets in the snouts of the module at a rate of approximately 0.1 litres per minute (LPM), which in turn flows through the straws of the manifold. Argon is ionised to produce the primary electrons and was selected because it is a noble gas with fewer excitation modes compared to a molecule. Ethane acts as a quencher gas: it has many excitation modes that are used to absorb the photons produced during the secondary ionisations which if not absorbed would cause an electrical breakdown in the gas [62, 63].

Located at the centre of the straw is the sense wire. This is held at a high voltage (HV) of 1650 V and acts as an anode while the straw wall, which is grounded to the manifold, acts as a cathode. This leads to a strong electric field in the straw tube which is directed radially out from the wire. In the presence of the electric field between the sense wire and the straw wall the interacting particles will experience a radial force. This causes the liberated electrons to travel towards the sense wire and the gas ions to travel towards the straw wall. As the electrons travel towards the sense wire they will undergo further interactions with gas molecules producing further ionisations, which will slow down their progress towards the sense wire. The overall motion of the electrons is known as drift. The drift velocity in the straw is approximately $50 \, \mu m/ns$. Due to the presence of a strong vertical magnetic field felt in the straws an orthogonal force is put onto the travelling electrons. This leads to them travelling in a curved path with the angle of this curvature known as the Lorentz angle.

The current signal induced on the sense wire by the travelling electrons is very small. However as the electrons travel very close to the sense wire, the electric field is strong enough to accelerate them. This leads to further interactions between the electrons and gas molecules in a short time, causing an increase in the number of liberated electrons. These will go onto ionise further gas molecules leading to an effect called avalanche multiplication which produces a rapid increase in the number of liberated electrons. The straw drift chambers are known as proportional counters. This means that the signal detected by the wire due to the avalanche is roughly proportional to the number of primary ionisations. The increase in the number of electrons gives a signal large enough to be seen over the noise threshold. The time and width of this signal, generally known as "a hit", is recorded in the readout electronics.

During an avalanche, the collisions cause excitations which lead to the release of photons from the subsequent de-excitation. Photons with enough energy can travel past the avalanche volume and create further electrons from interactions with the gas. This then creates their own avalanches which leads to a breakdown of the gas. To stop this from happening a quencher gas is flowed through the straws. The experiment chose Ethane as it has multiple modes of excitation and therefore can absorb photons of different energies. The avalanche period also leads to the creation of more ions. These drift towards the cathode straw wall. This long distance movement from the region of the avalanche to the straw wall induces a signal which is much larger than the signal produced in the electron avalanche. The ions possess a much larger mass and so their drift velocity is much slower than the electrons such that the signal produced by the ions is separate and much later (of the order of μs) than the electron signal. The signal induced from the ions is referred to as the ion tail.

The signal induced by the initial ionisations from the positron thus results in two pulses: an initial smaller pulse from the avalanche electrons and a much longer pulse from the ion tail. The shorter pulse from the electron avalanche triggers the frontend electronics. The much larger and slower ion signal is suppressed by the electronics. This means that the electronics can cope with a high rate of signals as the larger ion signal does not mask subsequent electron avalanche signals which could occur very soon after the first.

The time that the electronics is triggered is designated as the time of the hit. For the purpose of track reconstruction the path that the positron travelled must be known precisely. The hit time t_h is determined from the time that the positron entered into the straw known as t_0 and the drift time t_d. This is the time the primary ionisation electrons takes to drift from the initial interaction point to the sense wire. The hit time t_h is calculated using the equation

$$t_h = t_0 + t_d. \tag{5.1}$$

Therefore if t_0 is known then t_d can be calculated. This relies on a detailed knowledge of the behaviour of the charged particles in the straw gas. From t_d the distance that the charged particle travelled through the straw (and its distance away from the wire)

can be inferred. This is known as the Distance of Closest Approach (DCA) and gives a circle of possible points where the primary ionisation has occurred called the drift circle. A diagram of a positron passing through a straw and causing primary ionisations is shown in Figure 5.4. No knowledge of the vertical direction is known and so this leads to a cylinder around the wire of possible points where the primary ionisation will have occurred. To resolve this issue and determine the positron's trajectory through the tracking detectors, the cylinders from multiple straws are combined to determine the positron's path. This motivates having the straws orientated in two different directions, as it enables the determination of the vertical direction of the positron's trajectory.
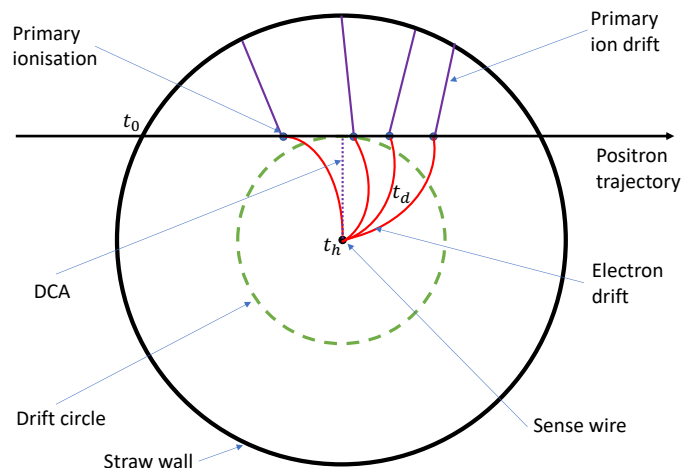
Figure 5.4: A diagram showing primary ionisations caused by the interaction of the positron with the straw gas. This indicates how the drift time t_d is calculated from the hit time t_h and the t_0 value.

5.4   Track formation

A charged particle travelling in a uniform magnetic field perpendicular to its motion will travel in a helical path. The tracking detectors are situated in the fringe field of the magnet and as such the particles experience a varying magnetic field radially and vertically [67]. This complicates the track fitting of the helical trajectory. This changing magnetic field also affects the path of the charged particles as they drift

through the straw, causing an added complication in obtaining the DCA for the positron. The track fitting is instead done by separating the path into short sections.

Drift circles are created and centred around the wire, using the drift radius calculated from the drift time and the drift velocity. By comparing the neighbouring straw drift circles potential tangents can be found. To do this a line of best fit can be drawn from the shortest distance of each tangent between two drift circles.

The trajectory of the positron's path through the straw tracking detectors is calculated from the DCA of the positron's path through multiple straws, along with detailed information on the positions and orientations of the straws. The stages of track formation are as follows. For each tracking module, the straw hits within a time period are grouped together. This time period is approximately $100\,\text{ns}$ and these hits are grouped together to form a time island. Next there is spatial grouping of these hits. This is first done by grouping straw hits within the same view (U or V) in different layers if they are adjacent. These are referred to as clusters. The clusters for the U and V views for a single module are then group together to form seeds. The candidate positron tracks are formed by grouping together seeds in different modules based on which seeds are close in time (within $10\,\text{ns}$) and proximity to the previous one. Once straws have been identified as part of a potential track the t_d is determined in order to calculate the drift distance for each straw. For the simplified version in which a positron is travelling at normal incidence to the plane of the straws, a t_0 value for a cluster with individual hit times of t_A and t_B is calculated using the equation

$$t_0 = \frac{1}{2}((t_A + t_B) - (d/v_{\text{drift}})), \tag{5.2}$$

where d is the distance between the two wires and v_{drift} is the drift velocity.

This allows a t_0 value to be calculated for each straw and hence the t_d can be calculated in order to determine the DCA and then the drift cylinder of the positron's trajectory. In order to determine the vertical direction, the next cluster with a different view must be included, as these straws are orientated at a different angle. However this leads to a degeneracy when allowing for incident particles coming from any angle. The radial degeneracy of the DCA measurement means it is hard to

determine which side of the wire the particle travelled, this is called the left-right ambiguity. Multiple track fitting is required to determine which set of left-right combinations gives the best fit.

The track fitting is carried out using the GEANE (Geometry and Error Propagation) fitting algorithm [66]. This process involves taking the track parameters being fit:

$$\frac{1}{p}, \frac{pu}{pw}, \frac{pv}{pw}, u, v, \tag{5.3}$$

where the uvw coordinates are defined with any two orthogonal vectors u and v, with u and v typically lying in the surface of a detector and calculating the evolution of the error matrices which describe the uncertainties in the track parameters. This is done by transporting the tracks along small discrete steps, whilst checking for materials that the tracks could scatter off and determining the magnetic field in each step to account for its variation throughout the tracker module [52]. The track fitting relies on only the hit information from the U or V layers. This fitting algorithm combines the DCAs determined in each of the hit straws. One can define a χ^2 for a track by dividing the residuals of measured and predicted track parameters by their errors:

$$\chi^2 = (\vec{p} - \vec{x})^T (\sigma^{-1})(\vec{p} - \vec{x}), \tag{5.4}$$

where $\vec{p}$ are the predicted track parameters given from the fit, $\vec{x}$ are the measured track parameters and σ is the covariance matrix with the errors on the fitted parameters.

Minimising the χ^2 with respect to the track parameters leads to an improvement in the track fit [67]. An example of a track candidate is shown in Figure 5.5.

5.5   Track extrapolation

The extrapolation algorithm uses a Runge-Kutta Nystrom algorithm [68, 69]. This uses track parameters determined at the entry point and exit point of the tracking station to either extrapolate forwards to the calorimeters or backwards through the varying magnetic field to the muon decay point. This extrapolation is done in small steps to accommodate the changing magnetic field and to determine whether the
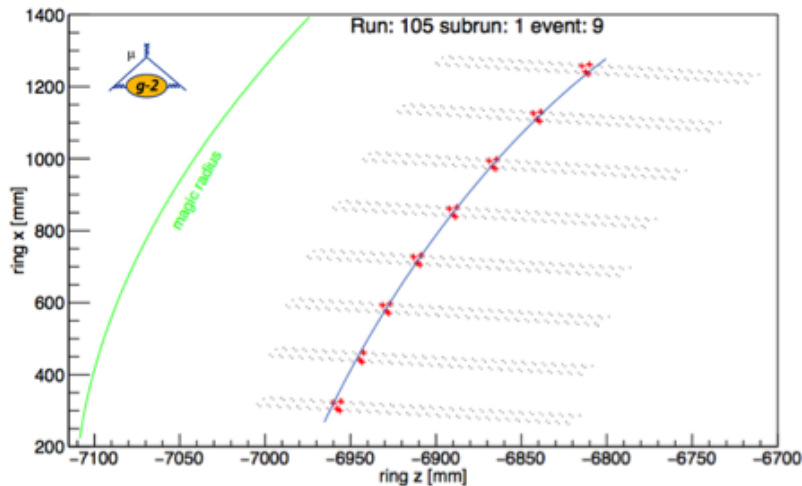
Figure 5.5: A plot showing an example of a track candidate.

particle is likely to hit any material. If this is the case then the particle will scatter, lose energy and have its path altered. These scattered particles are not used in the analyses. The decay position is taken to be the position of radial tangency, where the positron's momentum is tangential to the storage ring's magic radius. The extrapolated muon decay point information is used to infer the profile of the stored muon beam.

The straw tracker station is situated directly upstream of a calorimeter. Tracks can be extrapolated to the calorimeter and the energy at the point if extrapolation compared to the momentum. The data can also be used to determine if the two detectors are aligned correctly and also to independently determine the rate of pileup. Pileup is defined as the case when two low energy positrons hit the same calorimeter crystal and are not spatially and temporally resolved and are counted as a single higher energy positron.

5.6 Tracking quality cuts

Quality cuts are applied to the data to remove failed or badly fitted tracks, reduce the tails observed in the tracking distributions and lower the tracking uncertainties. A summary of the quality cuts used in the tracking analysis is shown in Table 5.2. The quality cuts remove approximately 60% of all measured tracks. The top 4 cuts in Table 5.2 remove around 55% of tracks, with the remaining cuts discarding a further

5% of tracks.

Therefore the cuts are optimised such that a small subset of tracks, representative of the whole sample, are reconstructed as accurately as possible. The fraction of tracks passing the quality cuts is rather small and will need to be improved for a track-only determination of ω_a and the EDM measurement. It is however adequate for the primary goal of measuring the beam motion throughout the fill.

Parameter	Quality Cut
Non-failed track/vertex	
No volumes hit	
Number of straw hits	≥ 12
pValue	5%
σ_y and σ_r	$0.5 < \sigma_y$ 3.5 mm and $0.5 < \sigma_r$ 5.0 mm
Track Entrance Point (at 1st module)	$60 < x < 150$ mm and $-40 < y < 40$ mm
Drift times	$0 <$ and < 70 ns
Track residuals	$< 500\ \mu$m
Fraction of missed layers	$< 30\%$
|U - V hits|	≤ 4

Table 5.2: The quality cuts applied to the tracking detector data.

5.7 Readout electronics

Once a signal has been produced on a sense wire two sets of electronics are used to convert the analog signal into a digital signal. These are the frontend electronics and the backend electronics. The frontend electronics are the boards which detect the signals on the wire and processes these into straw hits. A photograph of the frontend electronics is shown in Figure 5.6. The backend electronics are the electronic boards used to combine the data from all the frontend boards and also synchronise the signals using the common experimental clock.

5.7.1 Frontend electronics

The frontend electronics consist of ASDQs (Amplifier Shaper Discriminator with charge (Q)) boards which are located inside the tracker manifolds and used to convert the analog signals from the sense wire into digital hits. This data is then sent to

LVDS flexicable   Copper heat sink

ASDQ board

Viton o-ring   Internal HV cable
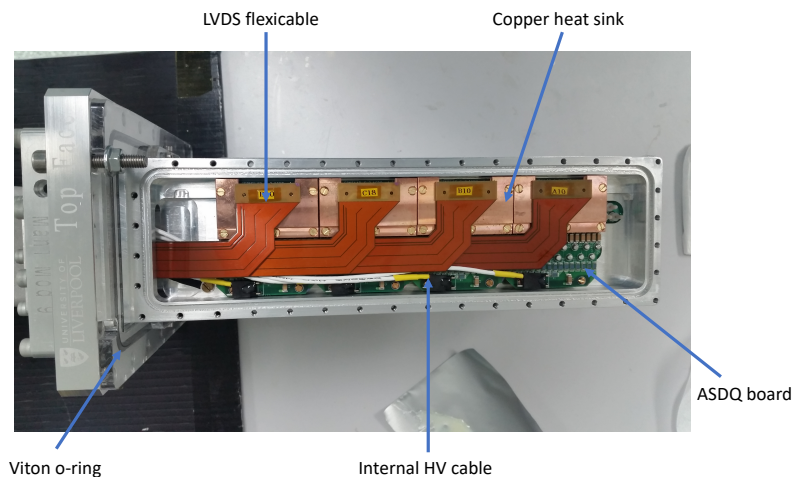
Figure 5.6: A photograph of the manifold frontend electronics with the important components highlighted.

the TDC (Time to Digital Converter) boards which are contained in the FLOBBER. The ASDQ boards are connected to the sense wire via long pins and as such are the first electronics to process the wire signal. Each ASDQ board connects to 16 sense wires and there are four ASDQ boards per manifold.

The conversion of the analog signal into a digital signal in the ASDQ is performed in several steps. These steps include amplification, signal shaping, baseline restoration and discrimination. The signal is shaped to smooth out the multiple small peaks that are created by the multiple primary ionisations when the charged particle passes through the straw. This creates a single smooth peak for a single charged particle. Baseline restoration is used to remove the long signal tail that arises from the much slower ion signal. The ion tail inhibits efficient high rate operation. However the time development of the signal is well known and so the ion tail can be cancelled out. This is done using a circuit element whose impulse response produces a mirror image of the ion tail. A polezero cancellation technique is then used to eliminate the ion tail in the signal. A detailed explanation of the ASDQ ion tail cancellation process is discussed in reference [70]. This ensures that primary ionisations from the next charged particle to pass through the straw are not concealed by the ion tail. This means that two signals can be easily distinguished, increasing the rate of signals that can be measured. The discriminator is used to register when the

signal passes a threshold. The digital hit time is the time the signal first crosses over the threshold and the hit width when it subsequently falls below the threshold. A diagram illustrating the steps the ASDQ takes to convert the analog signal to a digital signal is shown in Figure 5.7.
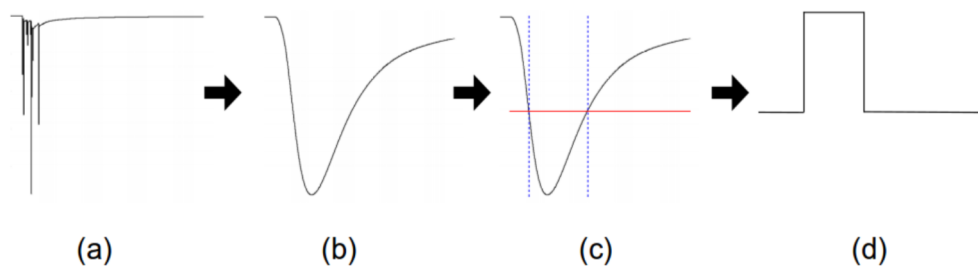
Figure 5.7: A diagram displaying the steps the ASDQ carries out to convert an analog signal to a digital signal. (a) Multiple short signals are measured for each of the avalanches caused by the primary interactions of the positron with the straw gas. (b) The amplification and shaping of the short signals into one smooth signal. (c) The discriminator selects the data that passes above the threshold shown by the red line. The blue lines indicate the section of the signal that passes above this threshold. (d) The digital signal created for the leading and trailing edges of the smoothed out signal. The ion tail is not included in the diagram [71].

The digital signals from the ASDQ boards are then sent to TDC motherboards housed in the FLOBBER via Low Voltage Digital Signal (LVDS) flexicables. Each straw tracking module uses four TDC motherboards and each motherboard is connected to two ASDQs. The FLOBBER was designed to hold the electronics not needed to be directly connected to the sense wires. The clock system provides a primary 10 MHz clock signal which is used as a timebase for generating the experiment's 40 MHz clock. This is sent to the Clock and Commands Center (CCC) for distribution to the detectors. The TDC board then time stamps the ASDQ signal to the precision of 625 ps using the 40 MHz clock signal. A detailed discussion of the experiment's clock system can be found in reference [73]. The channel number, hit time and width are sent to the backend electronics. The low and high voltage required for the tracking modules is supplied by a low voltage crate and a high voltage CAEN SY127 crate [74] located in a rack in the centre of the storage ring.
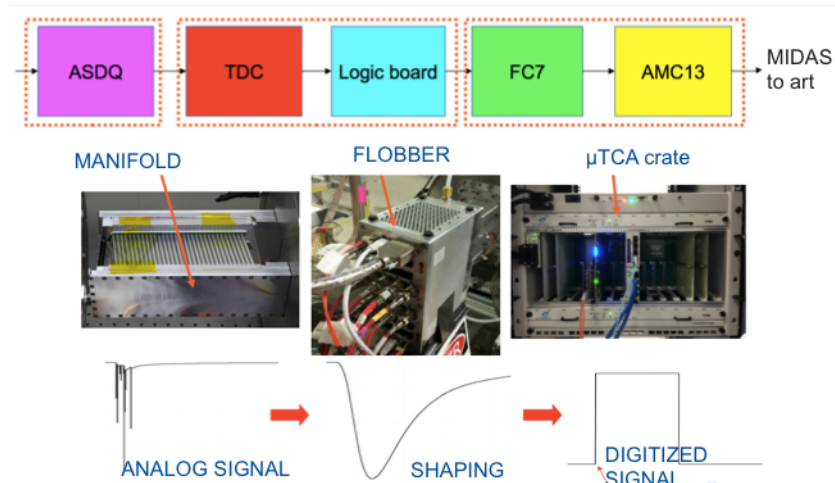
Figure 5.8: The path of the straw hit data through the frontend and backend electronics in the straw tracker readout system.

5.7.2   Backend electronics

The backend electronics comprises logic boards (LB), FC7s and a single AMC13. The two LBs per module are also located in the FLOBBER and provide an interface to the ASDQ-TDC pairs (1 LB per 4 ASDQs). The LBs supply clock and control signals to the TDCs and gather the information together into a single data block to be processed downstream in the FC7 and AMC13 boards. The LB consists of three external interfaces. A fibre-optic cable which connects to the higher level backend electronics to receive the external clock and control signals, the LV line supplying low voltage to the frontend boards and a serial communication port to the slow control hardware. Fiber optic cables can send data over large distances allowing the higher-level backend electronics to be located away from the trackers. They are located in the centre of the ring away from the magnetic field storage region, allowing magnetic materials to be used.

One FC7 μTCA advanced mezzanine card (AMC) per tracker is located in the μTCA crate located at the centre of the storage ring. Each FC7 is connected to 16 LBs. The FC7 is used to supply the clock and control signals for the LBs and collect a hit data from all the LBs into a single block. The AMC13 board is the most downstream board which is also housed in the μTCA crate and collects together the hit data from the FC7 boards as well as distributing the clock and control signals to the tracker modules. The AMC13 connects to a computer in the counting room
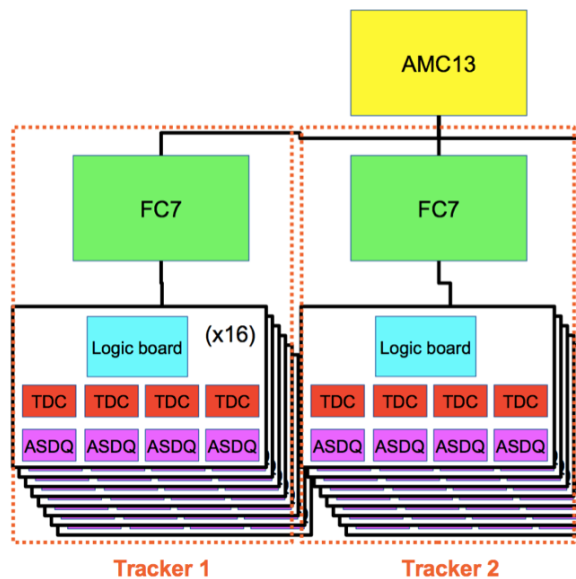
Figure 5.9: The hierarchy of frontend and backend boards and the numbers of each type of board used in the straw tracker readout system.

via a Gigabit Ethernet (GbE) fiber. Diagrams of the hierarchy of the frontend and backend electronics are shown in Figures 5.8 and 5.9.

5.8   Choice of wire voltage

Gain measurements were carried out to find the optimal operational wire voltage for the modules. The gain is the ratio of the final number of electrons detected by the straw wire to the number of electrons initially liberated in the gas. A higher voltage on the straw wire will lead to a larger electric field strength and therefore electrons in the straw will have higher energies after collisions, leading to an increased likelihood of more ionisations. The signal on the straw wire is proportional to the applied voltage. However if the wire voltage is set too high, the gas in the straw starts to breakdown with too many hits being detected by the wire and the electronics becomes saturated. If the voltage is too low, an insufficient number of electrons will be liberated during collisions and a small signal is produced which can be below the $200\,\mathrm{mV}$, threshold in the ASDQ discriminator.

An optimal wire voltage must be found between these two regions. This is the plateau region, combining high gas gain with a minimum of gas breakdown. To determine the optimal wire voltage, the number of straw hits for various wire voltages was

measured. This was carried out using a radioactive Sr^{90} β^- decay source with two types of gases; the test gas mixture used in the University of Liverpool cleanroom 80:20 $Ar : C0_2$ and the experimental gas mixture 50:50 $Ar : C_2H_6$. As can be seen in Figure 5.10 the gain is too low for voltages below 1200 V for the for the $Ar : C_2H_6$ gas mixture. With increasing voltage the gain increases and so does the number of hits recorded by the electronics. At a voltage of approximately 1550 V the number of hits recorded plateaus. This indicates that at this voltage approximately all of the beta particles travelling through the straw are detected by the wire as hits. This continues until the voltage reaches about 1700 V. From there onwards the hit rate increases due to an increasing gain indicating the breakdown of the gas and each beta particle results in multiple hits being recorded. Therefore the optimal voltage for the wire should lie within this plateau range: a voltage of 1650 V was chosen.
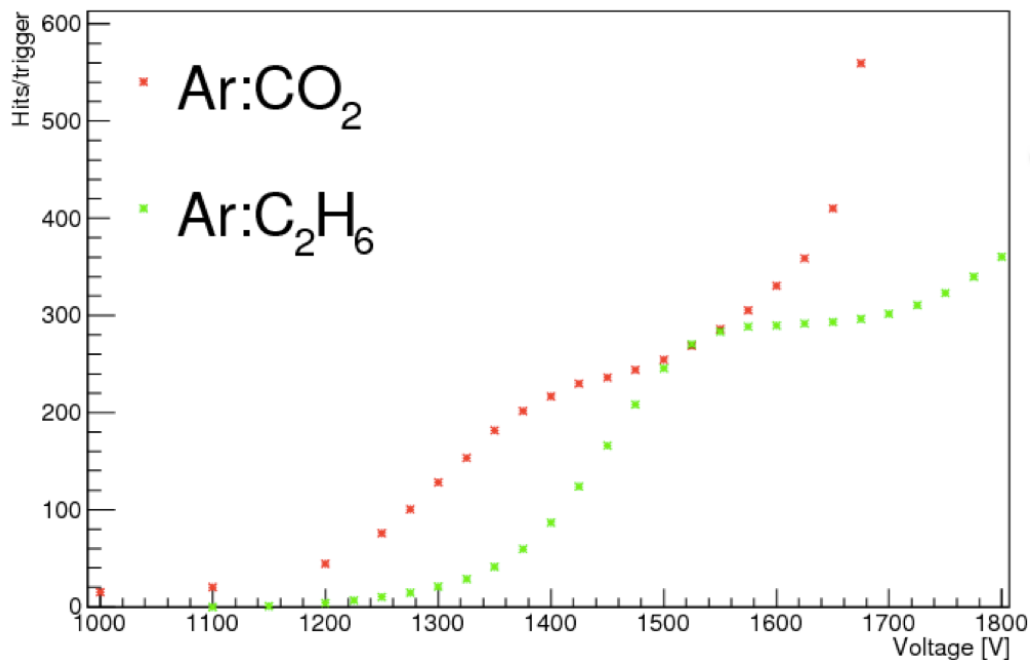
Figure 5.10: The number of hits from a Sr^{90} source as a function of wire voltage for both 50:50 $Ar : C_2H_6$ and 80:20 $Ar : C0_2$.

5.9 Data quality monitoring

The online monitoring of data from the straw trackers is critical to promptly identify and remediate possible failure modes of the detector and the data acquisition system.

The beam profile, drift time, and number of hits per straw are monitored by the experiment's shift crew. The detectors have performed extremely well: the longest period of downtime was two days when a gas valve froze in inclement winter weather. Figures 5.11, 5.12 and 5.13 are examples of the online monitoring web pages.

The data acquisition (DAQ) system for the experiment is provided by PSI's Maximally Integrated Data Acquisition System (MIDAS) software package. This collects and aggregates data from the frontend electronics at 200 Mb/sec and writes the data to tape.
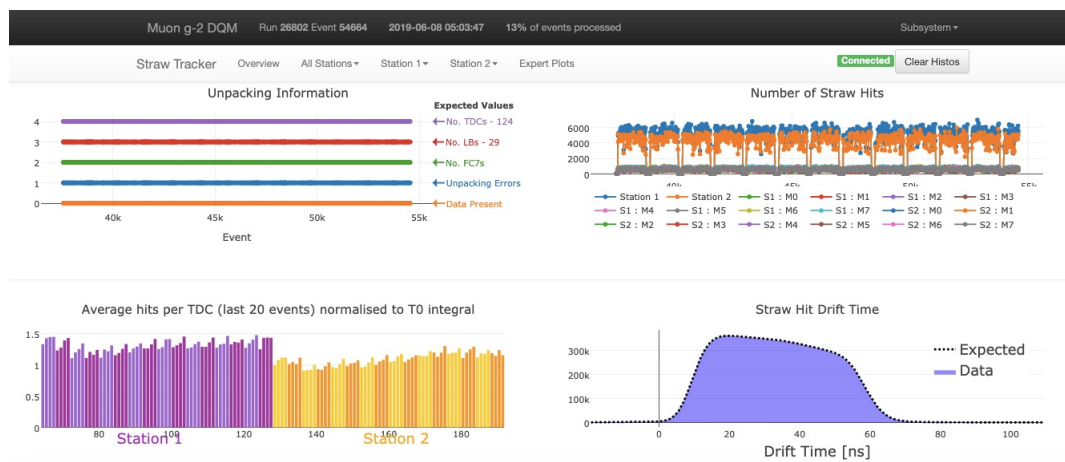
Figure 5.11: The online monitoring plots of the straw tracking detector. Top right: the number of hits in each tracker module. Bottom right: the expected and measured straw hit drift time. Bottom left: the average number of hits per TDC. Top left: a monitor of the tracker electronics.
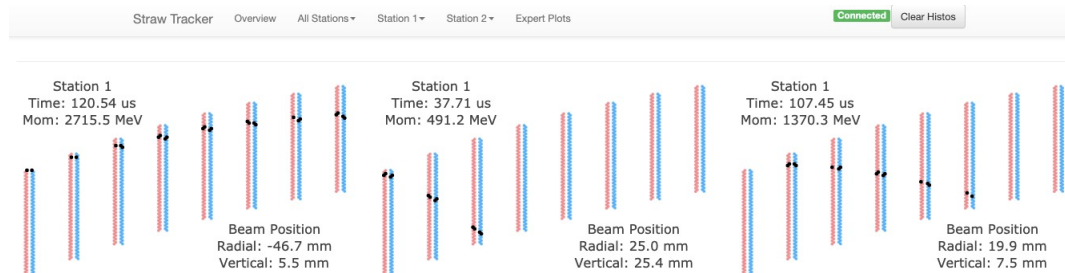
Figure 5.12: An online monitoring web-page showing the hits of potential tracks.
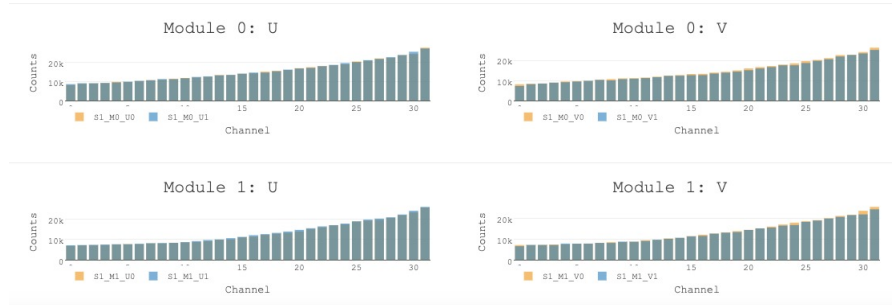
Figure 5.13: An online monitoring web-page displaying the number of hits in two tracker modules.

5.10   Straw Tracker performance

The first g–2 data taking period (Run-1) ran from 23rd March–7th July 2018. Figures 5.14–5.21 show data from the straw tracking detectors for a 60 hour subset of this period in April 2018.

Figure 5.14 shows the distribution of hits in both stations and is used to determine whether there are any dead or noisy channels.
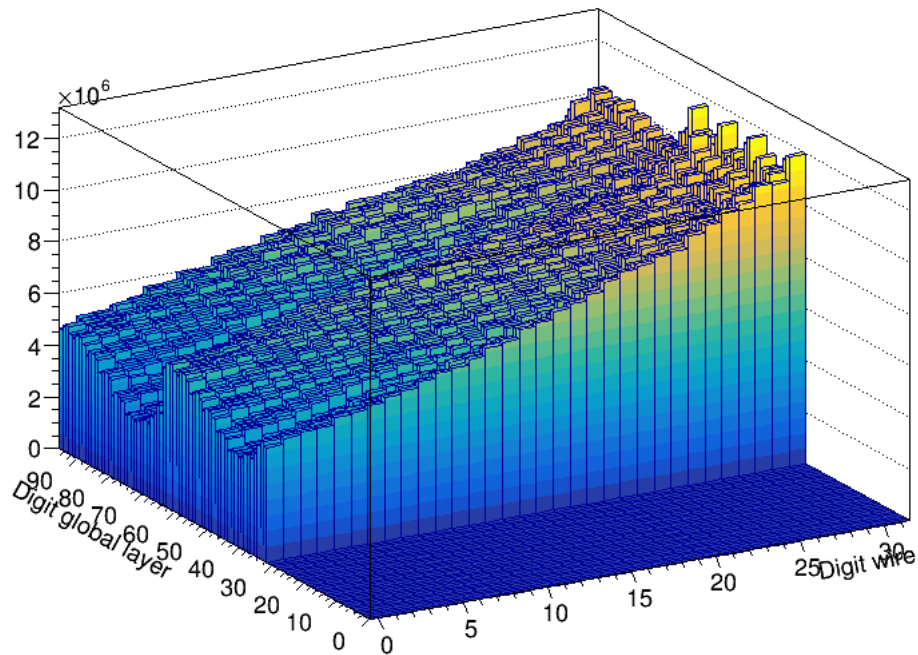
Figure 5.14: The number of hits in each straw for both tracking stations. The largest number of hits are recorded in the straws closest to the beam.

Figure 5.15 displays the drift times for all the modules. The hit time for the straw is used to group straw hits together to form tracks. From this a t_0 value is determined and equation 5.1 is used to calculate the drift time.
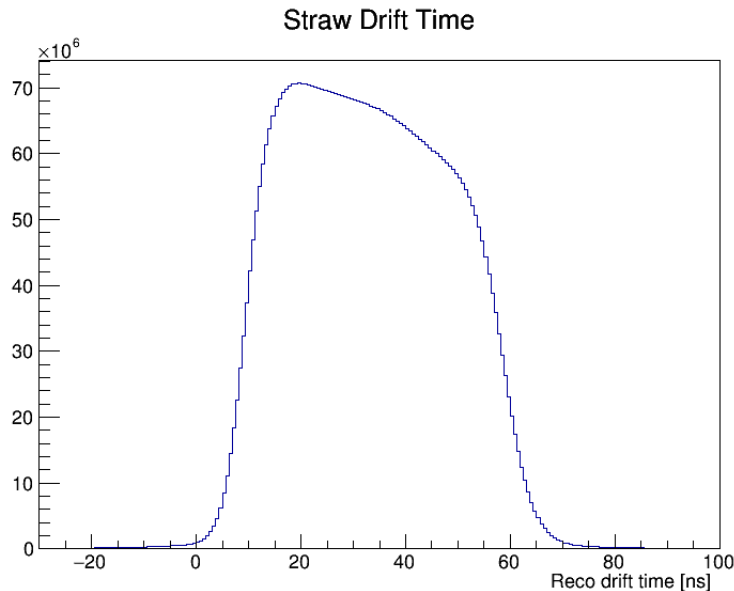
Figure 5.15: The straw drift time as measured during data taking by the tracking detectors.

Figure 5.16 shows the momentum of reconstructed tracks. The structure is due to the inherent momentum dependence of the efficacy of the track quality cuts. This is known because as the quality cuts were being optimised, the individual features of the distributions moved around. Figure 5.17 displays the origin of the tracks reconstructed and Figure 5.18 shows the vertical and radial beam profile.

Figure 5.19 shows the radial position of the beam as a function of time and illustrates the coherent betatron oscillation (CBO) of the stored muon beam and Figure 5.20 shows the radial distribution integrated over time. The high average radius is due to an under kick by the kicker system, where the ideal kick would centre the beam at r = 0. This also causes the beam width to be narrow at the high radius, whereas again with an ideal kick the narrowest point would be at the centre. The radial distribution peaks at approximately 20 mm with respect to the magic radius. The vertical position of the tracks is shown in Figure 5.21.
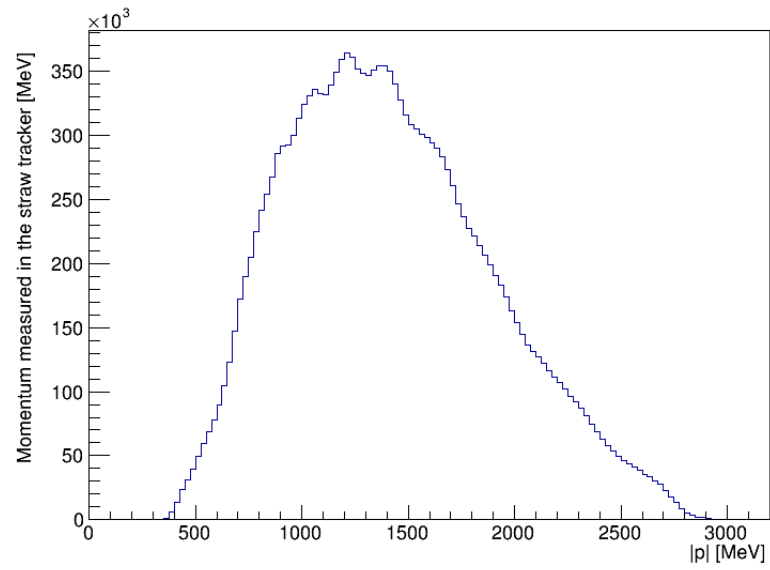
Figure 5.16: The momentum distribution of tracks.
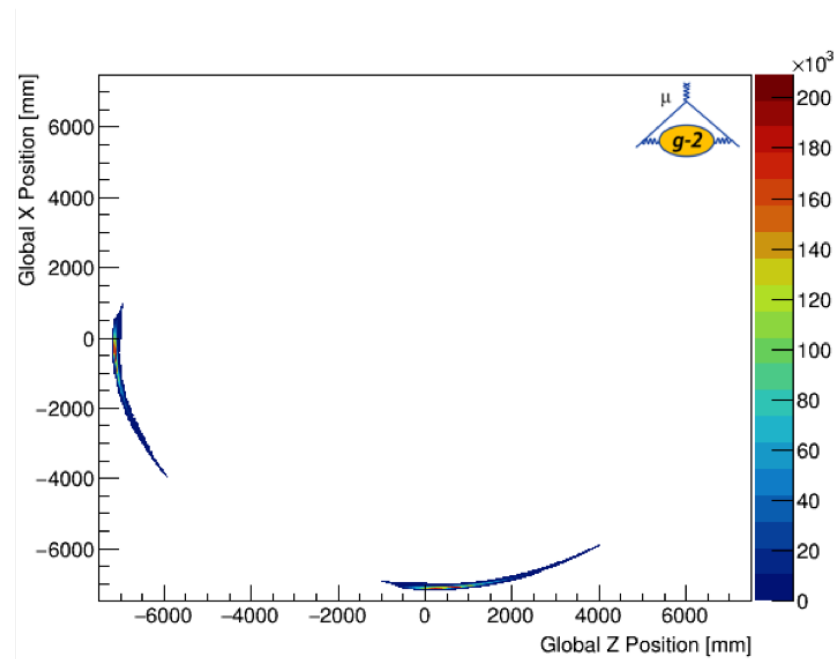
Figure 5.17: A top-down view showing the reconstructed muon decay positions obtained by extrapolating positron tracks.
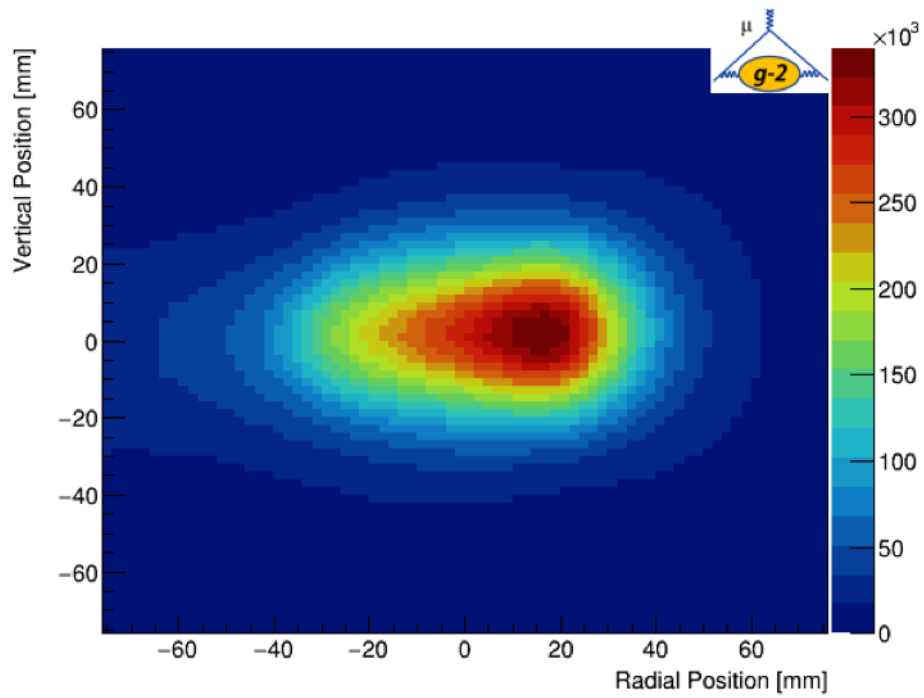
Figure 5.18: The muon beam distribution reconstructed from all extrapolated tracks.
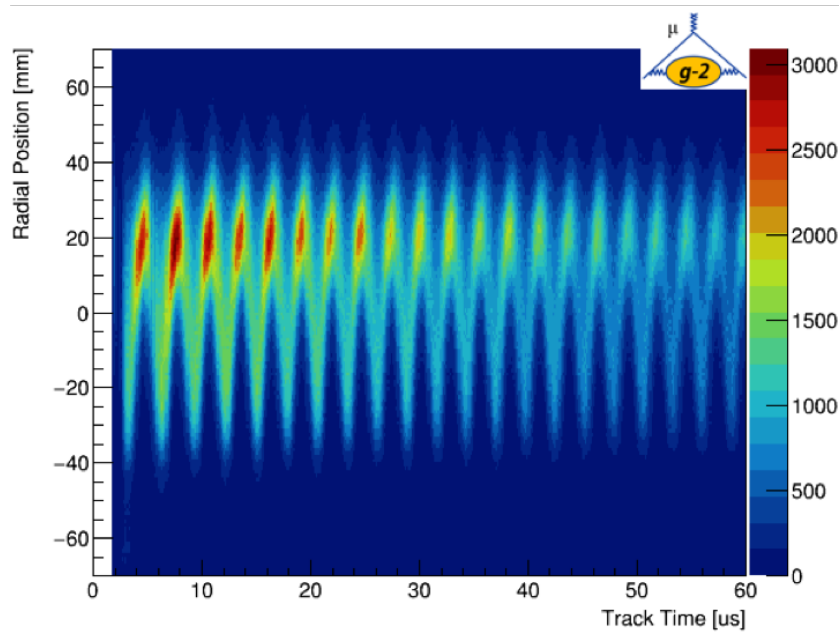
Figure 5.19: The radial position of tracks as a function of time.
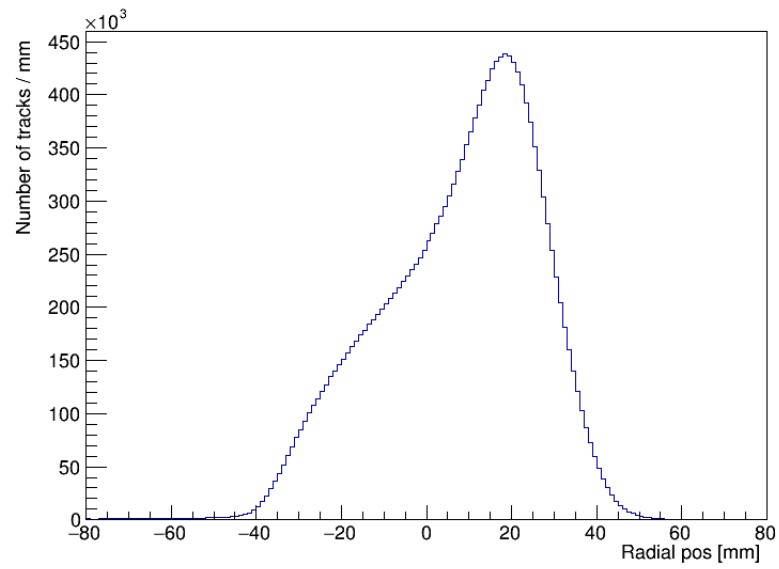
Figure 5.20: Reconstructed radial position integrated over time.
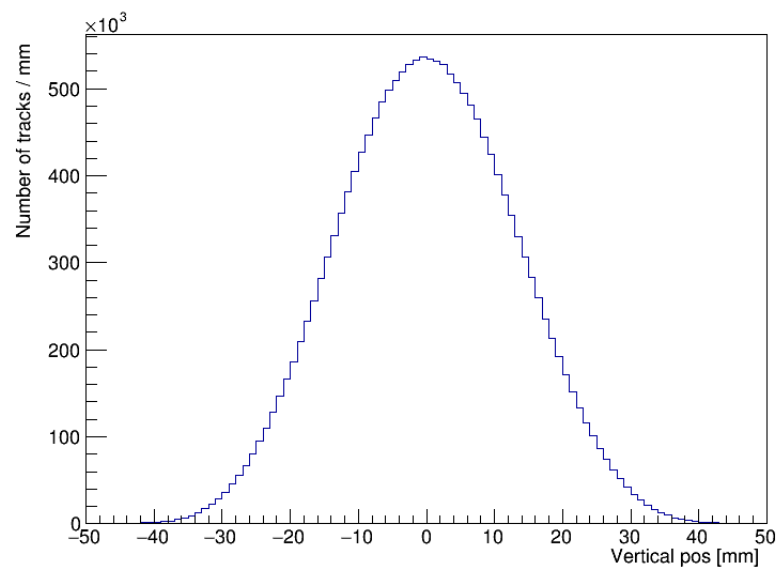
Figure 5.21: Reconstructed vertical position of tracks.

Chapter 6

Construction of the Straw Tracking detectors

6.1 Introduction

This chapter will give details on the construction of the straw tracking detectors as described in chapter 5. This includes each step in the construction process and the strict quality control tests which were meticulously carried out. This was done to ensure that the tracker modules run effectively and meet the required design specifications.

The straw tracking detectors were constructed by University of Liverpool technicians and PhD students in the ISO Class 5 clean room. This was done to prevent any contaminants from entering the module during construction. Personally I was solely responsible for the ASDQ testing and metrology surveys. As part of the construction team I worked on every step of the tracker module construction and testing processes apart from the straw assembly step. A total of 22 tracker modules were produced and tested in Liverpool before being shipped to Fermilab. An overview of the major steps in the construction process is illustrated by a flow chart in Figure 6.1.

6.2 Pre-assembly checks and preparation

Before construction of a tracking module could begin a series of checks and preparations must be carried out. The gold-plated copper pins which fix the wire in place
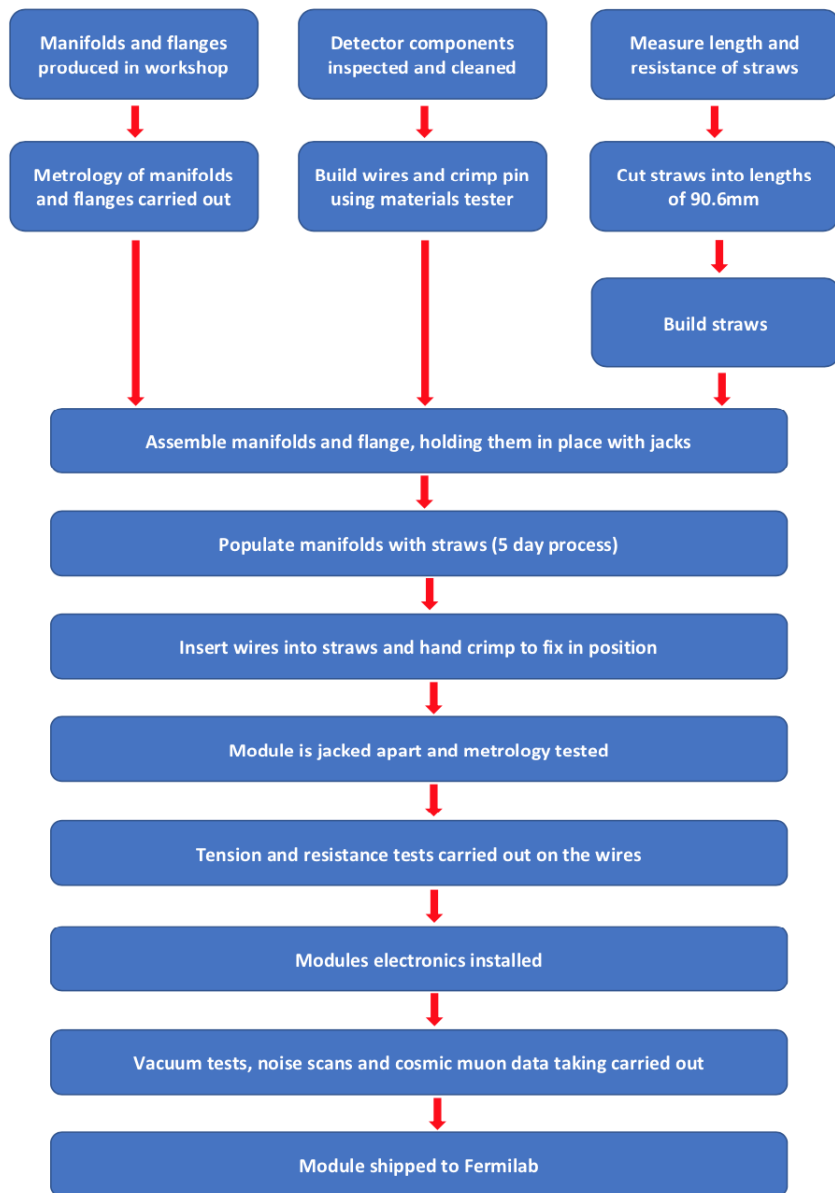
Figure 6.1: Module production flowchart.

within the manifold must be cleaned for any blockages inside before they could be used to construct wires. This was done by placing the pins in an ultrasonic cleaner which uses de-ionized water. They were then cleaned with isopropanol alcohol. Once the pins have dried, any remaining blockages could be removed by threading the pins with thicker $50\,\mu$m gold-plated tungsten wire. The aluminized Mylar straws were also visually inspected for any observable damage, kinks or unravelling of the straws which would lead to gas leakage. Straws with any visible sign of damage were not passed onto the next stage of construction.

The straws were manufactured to be approximately $1.3\,$m long and $5\,$mm in diameter,

which was confirmed by measurement once they were removed from their packaging. Straws differing from these dimensions could have been improperly manufactured. All straws measured had the correct length and diameter. The electrical resistance was measured before and after the supportive inner layer of paper was removed from the straw. If the resistance changed dramatically after the removal of the paper, this would indicate that damage had been created when removing it. The resistance for each straw should be around $200\,\Omega$ for both measurements. Any straw with a much higher or lower value or a straw with a changing resistance was not used in the construction process. The 98% of straws that passed were then prepared for a leak test.

6.2.1   Leak testing

As the Mylar straws are known to be permeable to some gases it was predicted that some gas leakage would be present. The rate of permeation of CO_2 that passes through the straw wall was calculated for every straw. Only the straws with the lowest permeation rates were selected for module construction. The experiment is operated under vacuum and in order for the quadrupoles to operate at the required voltage the storage ring vacuum cannot exceed 10^{-6} Torr. In order to achieve this each tracker station must have a maximum leak rate of 4.5×10^{-5} Torr·L/s, and each tracking module must not exceed 5.6×10^{-6} Torr·L/s. Anything above this is too high to be handled by the storage ring pumping system.

The leak tests were carried out using CO_2 rather than the experimental gas mixture of 50:50 Argon Ethane ($Ar : C_2H_6$) as this was not available for use in the University of Liverpool clean room. The leak rate measured was then converted to $Ar : C_2H_6$ to determine if the straws have a low enough permeation rate to be used in the experiment. The chamber for testing the permeation rate was constructed from copper pipes and was designed by members of the Mu2e experiment. A photograph of the setup is shown in Figure 6.2. This chamber contains a CO_2 sensor and holds a nitrogen environment during the leak test. The method of leak testing began by flushing the test chamber with nitrogen to remove any other gases present in the chamber. Whilst this was taking place the straw was flushed with CO_2 to clear out any other gases within the straw. This was done by gluing a gas inlet of viton
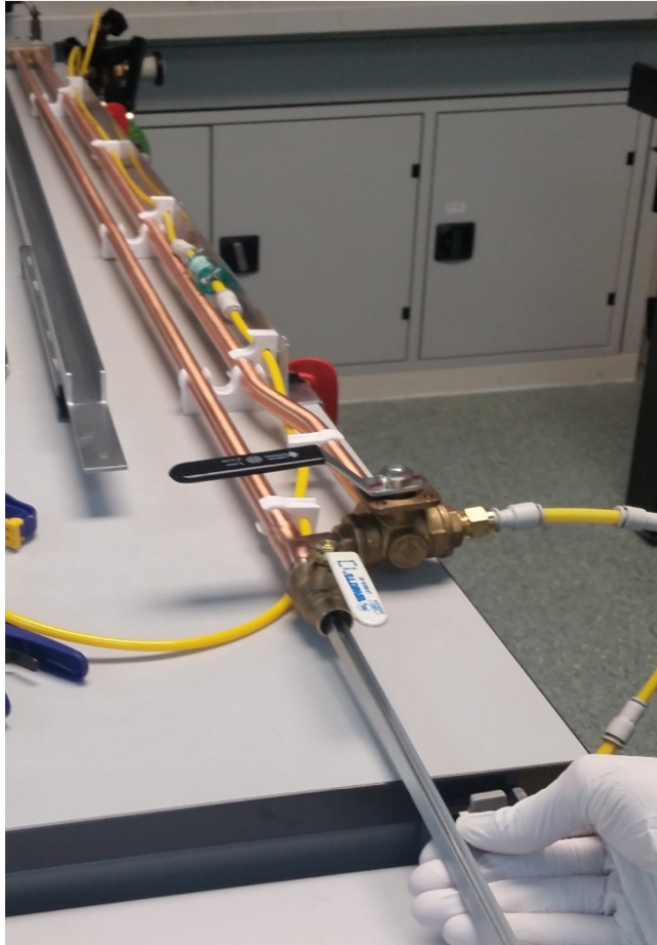
Figure 6.2: Photograph of a straw being placed into the leak testing equipment.

tubing to each end of the straw. The gas line to the CO_2 was then attached at one end to flow the gas through the straw. This was done for one minute. The straw end opposite the gas line was then sealed to allow the straw to fill up with CO_2. Initially this was over pressured to 1.7 relative to Atm. This was done to ensure that the straws will easily be able to cope with the experimental vacuum of 1 Atm. The gas pressure was then reduced to 1 Atm relative and filled at a rate of 0.15 LPM. While this was occurring the straw was inspected for any leaks. This was done by lightly pressing the straws to see if they had fully inflated. The straw is then sealed off from the flow of CO_2 and further inspected for any deflation of the straw. The straw was then immediately placed into the test chamber which was then sealed shut. Ensuring throughout the testing process that the straw was not kinked or bent in order to minimise the risk of damage to the straw. Within the test chamber, the CO_2 sensor recorded the levels of CO_2 that passed through the straw

wall into the test chamber. This test was carried out for 40 minutes with the CO_2 level as a function of time recorded. The leak rate was calculated using the slope of this distribution as shown in Figure 6.3. There were two separate batches of straws tested throughout the construction process. During pre-testing preparation it was discovered that the batch 2 straws had a wall thickness of 13μm, which is 2μm less than the batch 1 straws. At this point in the construction process the conversion rate from CO_2 to Ethane had yet to be determined. However it was predicted that the leak rate of Ethane was much lower than CO_2 and that the leak rate of Argon is negligible compared to the leak rate of CO_2. To set a threshold for the leak rate value it was decided to use one required for Ar:CO_2 rather than $Ar : C_2H_6$ as it was expected to leak more. The experiment required that the average leak rate for the straws using 50:50 $Ar : CO_2$ did not exceed 1×10^{-4} cc/min and so with the planned use of $Ar : C_2H_6$ this was given a lower threshold of 2×10^{-4} cc/min. The batch 1 straws had an average leak rate of 0.95×10^{-4} cc/min when tested with 50:50 $Ar : CO_2$, with a pass rate of 88%. There was concern that the batch 2 straws would have a much larger permeation rate and therefore a larger failure rate. To acquire enough straws for module construction, the threshold of 2×10^{-4} cc/min had to be reduced. By this time a number of vacuum tests had been carried out at Fermilab on a finished module built using batch 1 straws. This was done using both $Ar : CO_2$ and $Ar : C_2H_6$ to study both leak rates. The vacuum tests showed as predicted that Ethane permeates at a much lower rate compared to CO_2. Tests for this module showed a module leak rate of 2.76×10^{-3} cc/min for pure CO_2 and a leak rate close to a factor of 20 lower at 1.49×10^{-4} cc/min using 50:50 $Ar : C_2H_6$. This meant that the straw leak rate threshold could be reduced to 4×10^{-4} cc/min. The average leak rate for batch 2 straws was 2.45×10^{-4} cc/min. At this rate 86% of straws passed.

6.2.2   Pre-installation ASDQ testing

Prior to installation each ASDQ board was tested to ensure that the readout electronics and all 16 channels per ASDQ board were working correctly. This involved a setup where each ASDQ was connected by Kapton flexi-cables to a set of secondary electronics as would be done in the actual experimental setup, as shown in Figure 6.4. Instead of using muon cosmic data which was used in a later stage of module testing,
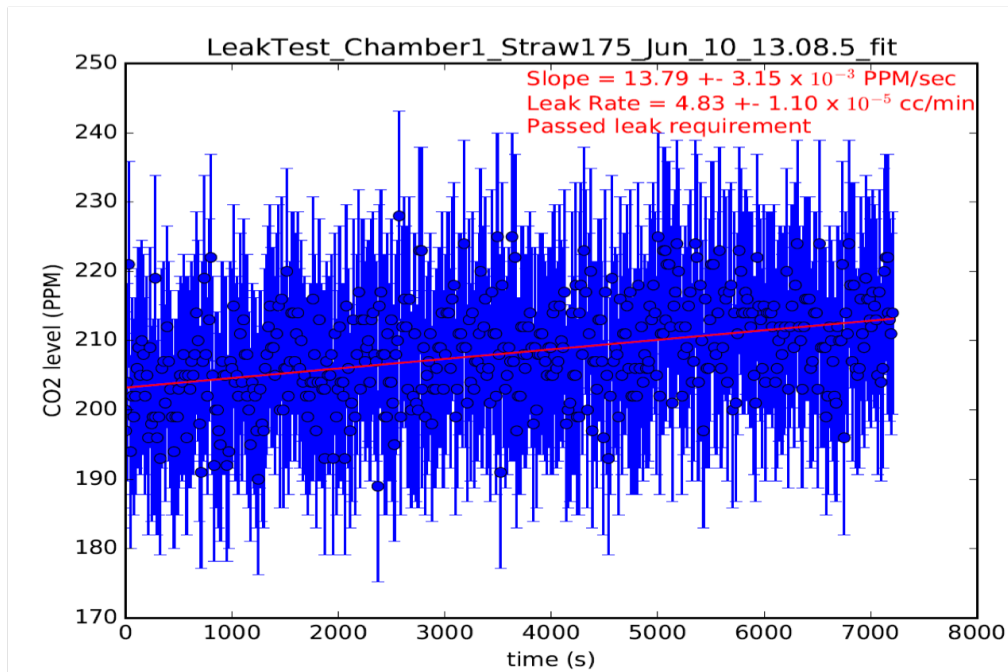
Figure 6.3: Graph of a straw with a passed leak rate of 4.83×10^{-5} cc/min.

pulses were sent to the ASDQ. Here 20 pulses were sent to each of the ASDQ's 16 channels, where the leading edge and the trailing edge were counted. If the channel was working correctly all the pulses should be sent back and so 40 hits would be read per channel. A plot of an ASQD working correctly is shown in Figure 6.5. An example of an ASDQ with connection problems is shown in Figure 6.6. Out of 165 ASDQs tested, 24 failed giving a pass rate of 86%.
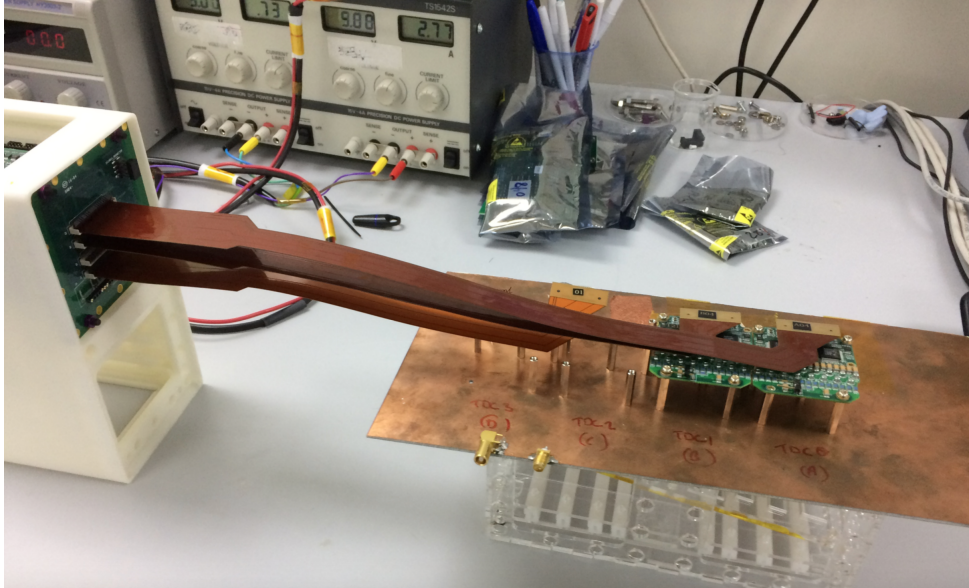
Figure 6.4: Photograph of the testing of two ASDQ boards with the testing setup.
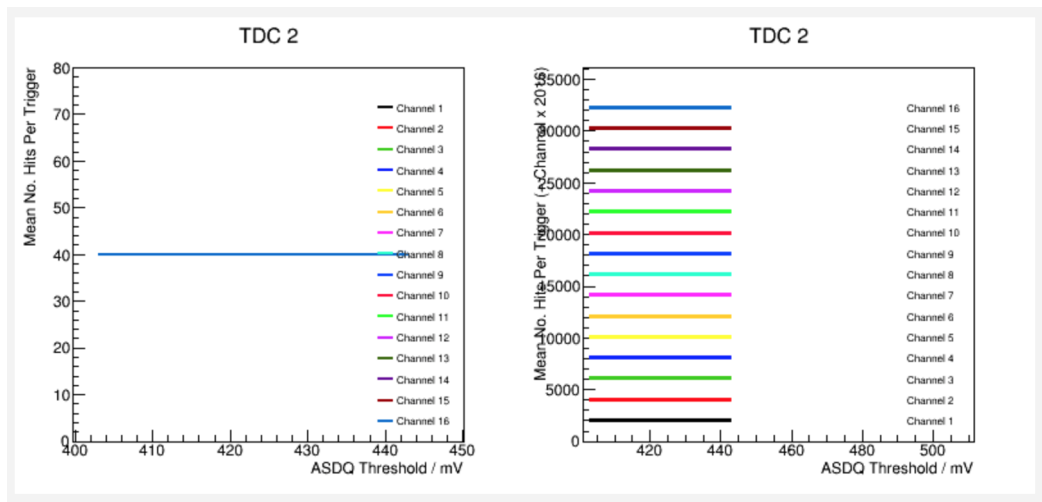
Figure 6.5: Example plot of an ASDQ that has passed testing with all channels recording 40 hits.
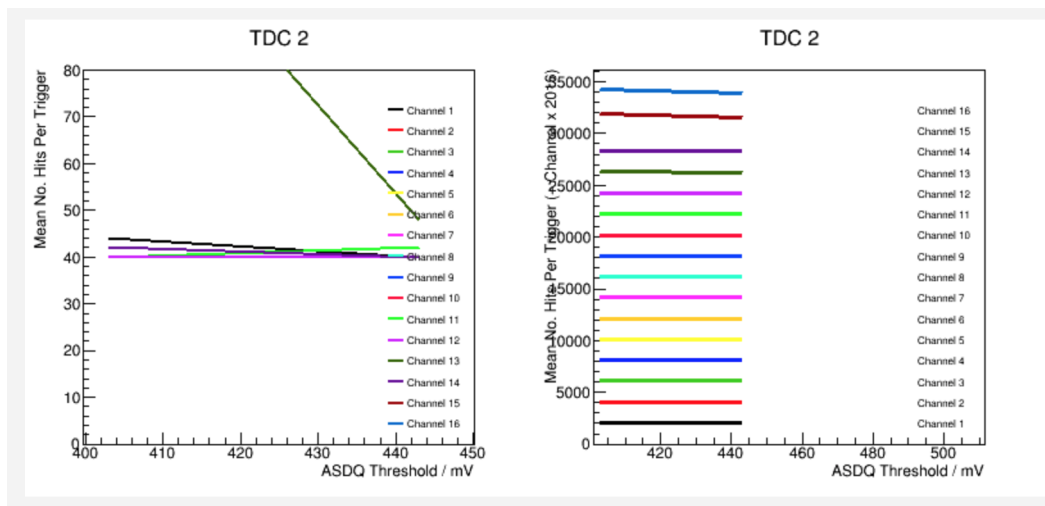
Figure 6.6: Example plot of an ASDQ that has failed testing. This shows that there are several noisy channels producing more than 40 hits.

6.3   Metrology

Before assembly, the machined pieces of the tracker modules had a metrology survey. The manifolds, flanges and lids were measured to determine their surface flatness and any wrongly sized or positioned holes. This information was also used to match together two manifolds and a flange for every module.
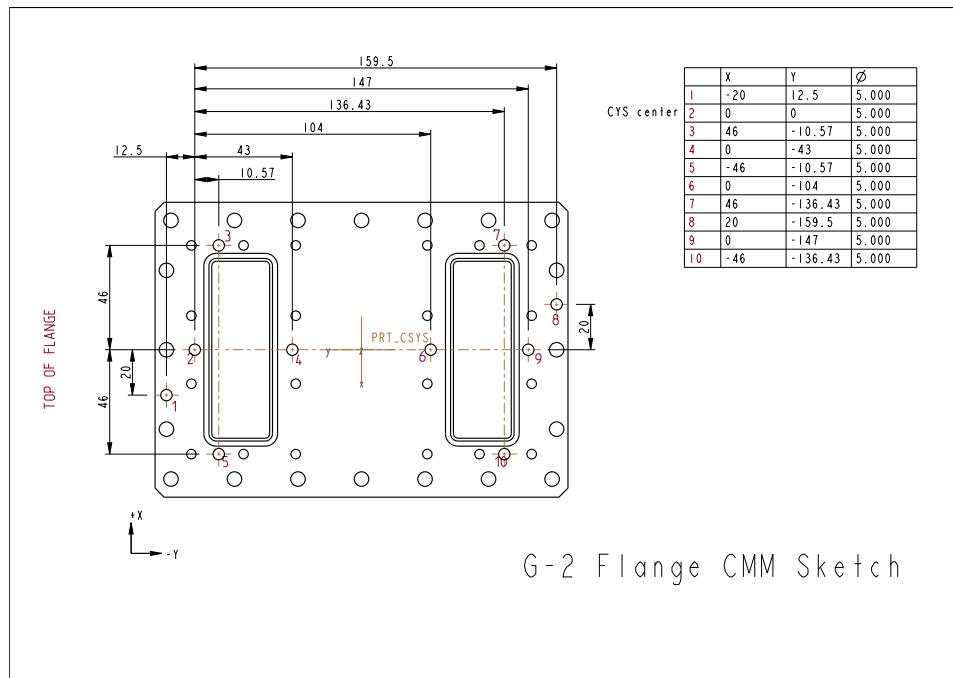
Figure 6.7: Engineering drawing of the flange with the nominal hole positions and sizes displayed.

The metrology survey was carried out using a contact probe with a Coordinate Measuring Machine (CMM). The aim was to learn how accurately the parts had been machined and assess if they lie within acceptable tolerances. Therefore determining whether they were ready for use in module construction or need to be returned to the workshop for alterations. An engineering design sheet showing the required hole positions and sizes for the flange is shown in Figure 6.7. The dimensions of each machined piece were required to be known accurately for alignment of the tracking detectors once they were placed into the storage ring. I wrote a program to measure the pieces automatically as previously all 1326 points for a manifold survey were done by hand. This improved the measurement time from approximately 6 hours manually to 50 minutes automatically. The manifolds were then paired with a flange based on the offsets measured from the flange surveys. The data was stored in

the Liverpool construction database which could then be utilised for any detector alignment studies required.
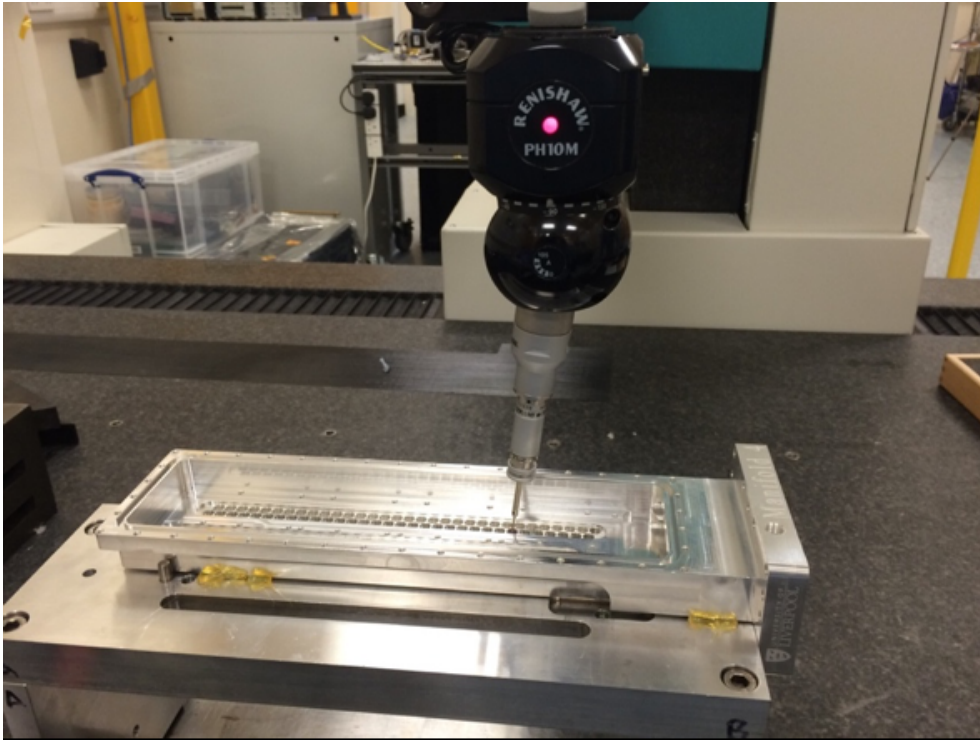
Figure 6.8: Picture of a CMM measurement of the manifold straw holes.

The software Metrosoft Quartis [76] was used to write a program to control the CMM to measure all the machined pieces. This program used CAD models of each piece to select the elements to survey and the number of probe points required for each measurement. A separate program was written for each of the three different pieces. For the manifold surveys a manifold was glued to a stand which was itself fixed in position to the granite work surface of the CMM. This ensures the position of the piece relative to the granite work surface was constant for each separate manifold measurement. Therefore the probe could find the correct position to start its measurement program. The setup is shown in Figure 6.8. From this a coordinate system for the stand was set up and used each time so that the probe would automatically know its position relative to the manifold. This was done using the 3-2-1 method. Where manually a plane of 3 points was made on the stands face. This was set to a primary direction of z and origin of z. Next a line of two points was measured on the side face of the stand, setting a secondary direction of x and an origin of y. A point was then measured on another face and set as the origin of x. This was done

the first time a program was written, saved and used each time. Next the manifold coordinate system was created with its origin located on a corner of the manifold end. This was done using the 3-2-1 method again. This manifold co-ordinate system is shown in Figure 6.9. This coordinate system was saved and would be redone each time a new manifold was measured, as there was likely to be a slight deviation in its position compared to the previous manifold. This ensured the coordinate system of the CAD was updated to the correct alignment for each metrology survey.
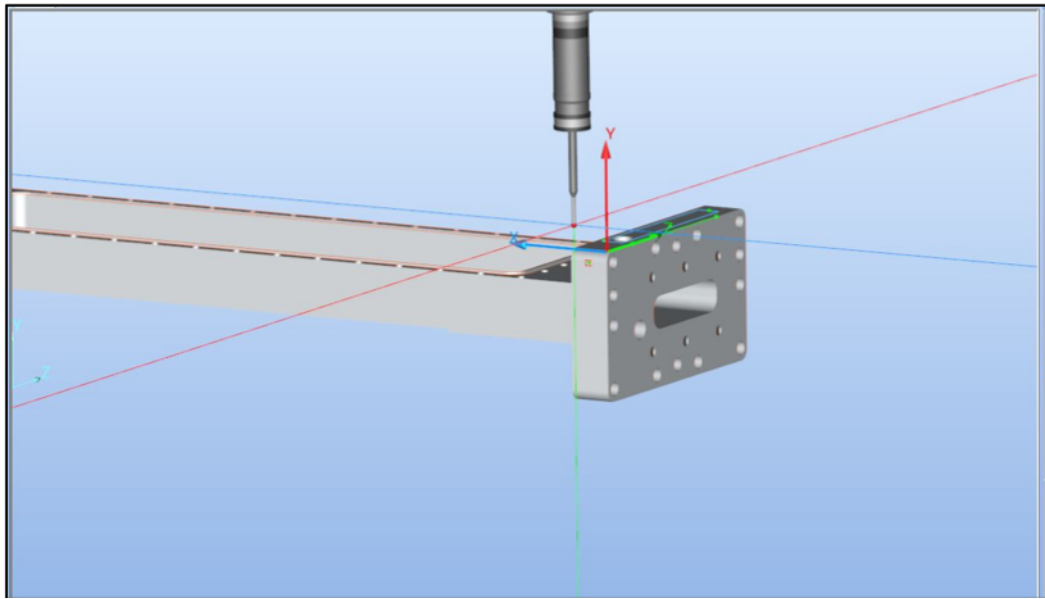
Figure 6.9: Setup co-ordinate system of the manifold. The blue arrow indicates the x axis, the red the y axis and the green the z axis.

The dowel holes and 128 straws holes of the manifold were required to be known in size and position precisely. The dowel holes being used to locate and position the manifold and flange together, prior to being fixed by bolts. These were measured as cylinders by the probe which could also determine if there were any bumps inside the holes which need removing. The software display as straw holes are being measured is shown in Figure 6.10. The straw hole measurements were carried out by the program using a loop which measures a cylinder and moves the probe 6.052 mm along to the centre of the neighbouring hole. This was done for each straw row. As the expected positions were given in the CAD model any deviations of individual holes or offsets of entire rows would be measured by the probe. Along with the holes, the various manifold faces and the o-ring plane were measured for flatness and positioning.
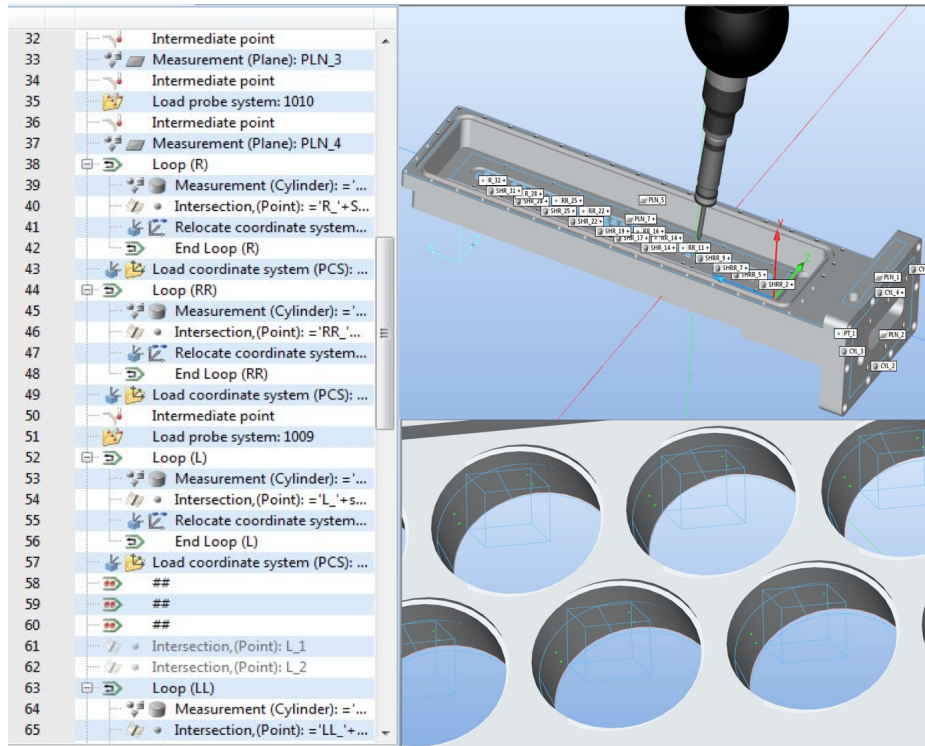
Figure 6.10: Left: A screenshot of the Metrosoft Quartis program. Right: A screenshot of the program display during a manifold measurement.

Once all measurements were completed, the database contains all the values required including nominal values, the values measured and the range of measurements for each element. From this data any alterations to the pieces of equipment could be carried out. The data was then used to match pairs of manifolds together with similar offsets and choose a flange to match with the manifolds. Plots from the database showing a typical measurement of a dowel hole and a manifold surface are shown in Figure 6.11. These display the measured probe points and any deviation from their nominal values. Plots showing all the straw holes sizes and flange dowel holes sizes measured are shown in Figures 6.12 and 6.13 respectively.
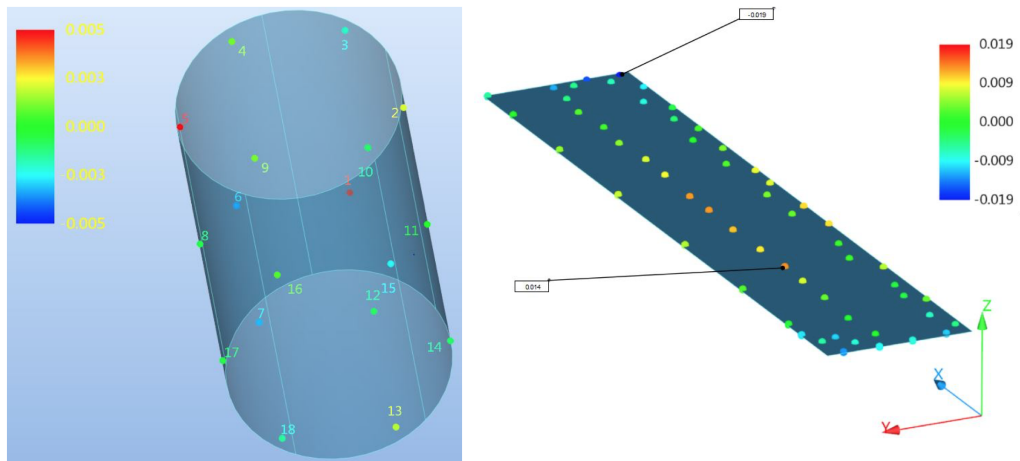
Figure 6.11: Graphical images of results from the Metrosoft Quartis database. Left: A plot of a dowel hole displaying the probes points and the difference from their nominal value in mm. Right: A plot of a plane on the manifold with the probe points showing the difference from their nominal flatness in mm.
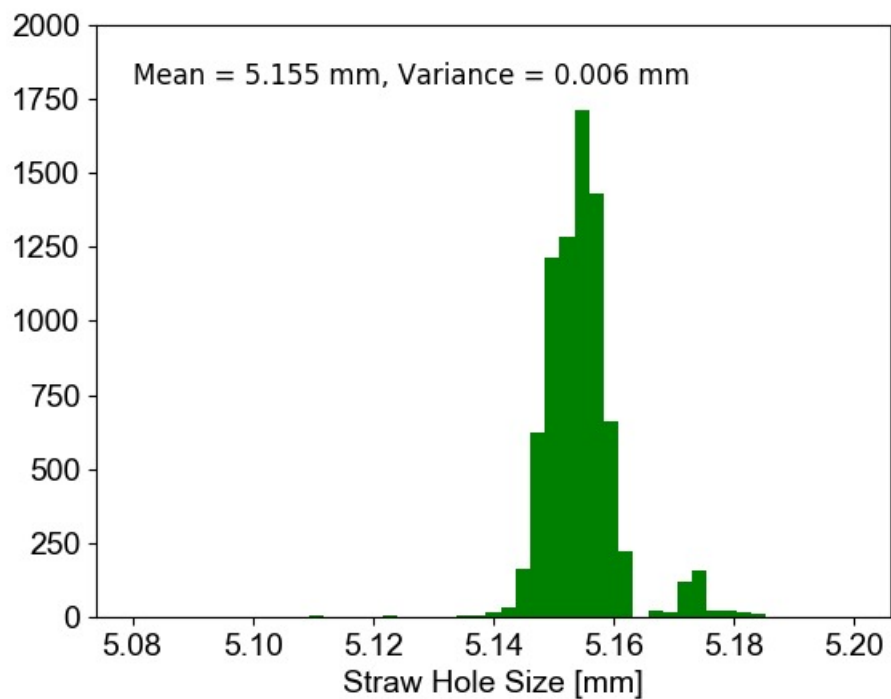
Figure 6.12: Plot displaying the measured manifold straw hole sizes for all manifolds measured. The nominal size for a straw hole being $5.15\,\mathrm{mm}$ with a tolerance of $\pm0.3\,\mathrm{mm}$.
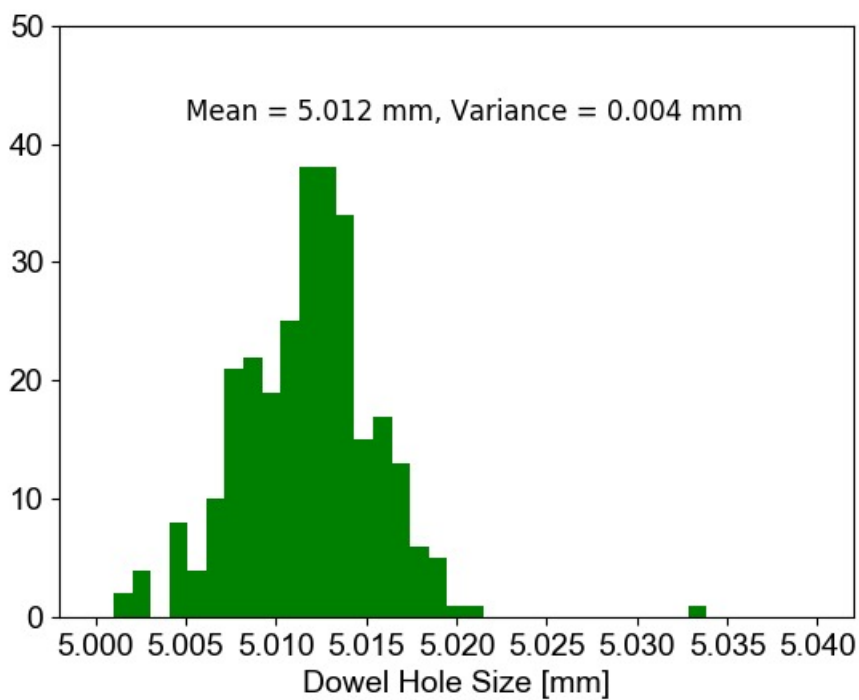
Figure 6.13: Plot showing the size of all flange dowel holes measured. The nominal size for a flange dowel hole is $5.0\,\mathrm{mm}$ with a tolerance of $\pm0.2\,\mathrm{mm}$. The dowel hole sizes were all larger that the nominal size but all apart from two lay within the allowed tolerance.

6.4   Wire crimping and threading

The wires were prepared prior to being strung into the manifold. This involved threading the wire through gold plated copper pins. The $25\,\mu$m gold plated tungsten wire was threaded through a long pin which was then crimped using the materials tester to secure the wire in place. The copper wire must be cut to a length much longer than the straw length, so wires of about 80 cm were cut. The wire was threaded through an injection molded insert which contains slots to allow gas flow through the straws and then threaded through a long pin. Glue was then applied to the end of the long pin which was then placed inside the insert, leaving a small length of the wire going through the pin with most left behind the insert.

To secure the wire in place the long pins were crimped using a Lloyd LRX Plus materials tester [77]. The pins were placed horizontally into the materials tester to ensure an even distribution and were crushed using a 1 kN load cell. A photograph of the crushing process is shown in Figure 6.14 with a close up photograph shown in Figure 6.15. To measure this process a Epsilon Extensionometer [78] was attached to the crushing jaws to measure its extension as it crushed the pin. This data produced a graph which was inspected to ensure that the crimping was carried out correctly. The pin diameter was also measured before and after crimping using a vernier caliper for comparison.

The wires were then left for 24 hours to allow for any expansion of the pin after the crimping process. The short length of the wire was then gently pulled while holding the insert to see if the wire could be pulled through and hence the crimp had failed. Any wires that failed were re-crimped and pull tested again.

6.5   Straw assembly

The long straws that passed leak and resistance tests were then cut into 90.6 mm sections with a guillotine. The aluminium end pieces were then glued to each end of the straw. There are two types of aluminium end piece. The top hat has an elevated ridge at one end which allows the straw to rest in the straw hole and provides the pin for the electronic readout end of the wire. The non-top hat does not connect to the manifold electronics.

Figure 6.14: Photograph of the Lloyd LRXPlus materials tester crimping a pin.

The gluing was done using a q-tip to carefully apply a silver epoxy TraDuct 2902 [79] to the end pieces and attach them to the straw ends, ensuring that the straws were not bent or damaged as the two were bonded together. A row of completed straws is shown in Figure 6.16.

The selected manifold pair plus a flange were put together, positioned correctly and then secured in place by jacks which held the manifolds a selected distance apart. Then 128 straws were inserted and fixed in place into the manifold straw holes. In total the process to glue 128 straws into the module took 5 days. Firstly the straws had silver epoxy applied between themselves and the module. This was used to produce an electrical grounding of the straw to the module. To provide a gas seal between the straw and the module Araldite 2020 was applied. The process required 5 days due to the time the curing took to dry and the fact that only one layer was done at a time to minimise the risks of moving or knocking the straws while the bond was curing.

6.6   Module construction

The modules were placed on the stringing jig which was used to populate the straws with the individual wires. The prepared wire was threaded through a straw using a plastic rod with a hole in the end to attach the wire. The rod was pulled the entire
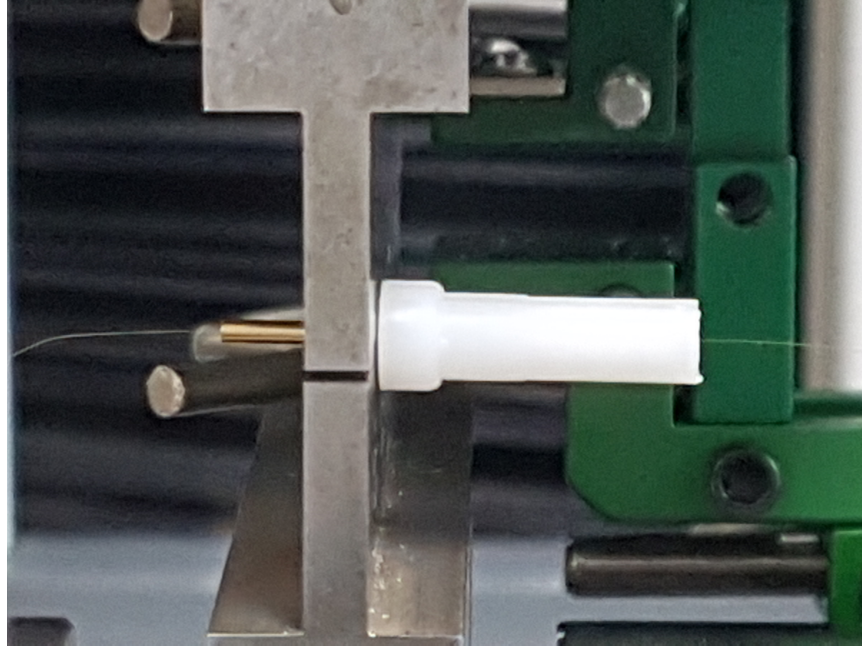
Figure 6.15: Close up photograph of a pin being crushed.
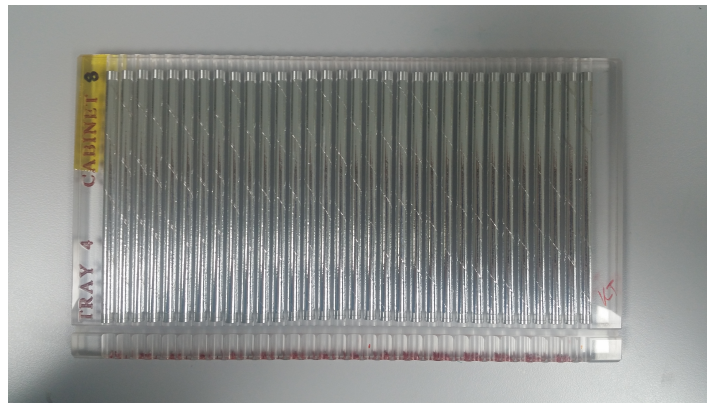
Figure 6.16: Photograph of a row of 32 completed straws.

way through a straw to the opposite end and removed from the other side to thread the wire. A photograph of this is shown in Figure 6.17. The wire end with the pre-crimped pin went into the side of the straw with the top hat aluminium end piece and was fixed there while the bare end of the wire was pulled through to the other end of the straw. Another insert was threaded through the wire and fixed into the non-top hat straw end, with a short annealed pin being threaded onto the wire. The short pin was annealed so that it was easier to crimp with a hand tool. Once both the insert and pin were threaded through the wire a 30 g weight was hung from the end of the wire to provide the required tension while the pin and insert were being secured into the module. The short pin was then glued into the insert and then the

pin was crimped with a hand crimp tool to secure the wire in place. The remaining wire with the weight attached was then cut off and the wire trimmed off as close as possible to the pin end. Glue was then placed on top of the wire to cover it and stop any electrical discharge that could occur. The stringing process was repeated for all 128 straws. Once the stringing process had been completed, the jacks that were holding the manifolds in place were moved apart $50\,\mu$m to produce a $50\,$g tension equally to the straws and wires. This was done to compensate for expansion under vacuum.

Figure 6.17: Photograph of a wire being threaded into a straw on the stringing jig.

6.7   Post module assembly wire testing

A tension test was carried out on the wires after stretching. A tension of $50\pm20\,$g was required. This is about half of the tension needed to break a wire. The higher tensions were desirable to minimise the gravitational sag on the wires. The tension test was carried out by placing a magnet above the test straw. This was positioned above the straw onto a thin layer of perspex to protect the straws. Crocodile clips connecting to the tension tester device were attached to each end of the straw pins. The tension was measured by sending current down the wire and varying its frequency in an external magnetic field. The varying electric field would induce a magnetic field and cause the wire to resonate in the external magnetic field. The current of the wire was recorded

after every pulse. When the frequency of the current pulse reached the resonance frequency of the wire, the current induced in the wire would be recorded and used to calculate the tension. A photograph of a tension test is shown in Figure 6.18. The tension tester calculated the wire tension using the equation:

$$T = 4Lmf^2, \tag{6.1}$$

where f is the frequency in Hertz, T is the tension in Newtons, m is the mass of the wire in kilograms and L is the length of the wire in metres.

Figure 6.18: Photograph of a tension test being carried out on a wire.

Module number	No. of wires re-strung	Module number	No. of wires re-strung
1	32	9	5
2	27	10	7
3	11	11	4
4	7	12	6
5	8	13	4
6	7	14	5
7	5	15	5
8	4	16	6

Table 6.1: The number of wires re-strung for each module.

A resistance test was also carried out on each wire. This was done by touching probes to the pins on either end of a wire which were connected to a digital multimeter. The

resistance of each wire should be within the range of 10–13 Ω. If wires lie outside this range, they would be removed and re-strung. The number of wires that had to be re-strung due to crimp and resistance test failure is shown in Table 6.1. A carbon fibre post was then fitted to the non-flange end of the module and used to secure the manifolds in position. The new manifold separation distance was checked using the CMM, and then the jacks could be removed.

6.8   Module electronics installation

Once the resistance and tension tests had been completed along with any re-stringing and the wires had passed all requirements the module electronics could be inserted. The electronics required include eight ASDQ boards (four per manifold) which were placed onto the readout long pins. End caps were placed onto the short pins providing insulation to stop any electrical discharge from the pin to the ASDQ boards. The two ASDQ chips on each board were then covered with a PTFE thermal heat pad. This was done to prevent the boards overheating by transferring the heat to copper heat sinks which were fixed to the ASDQ boards using brass screws. The heat sinks pass the heat onto the manifold. Four flexi cables and HV cables were connected to the feedthrough board, inserted through the snout and connected to the relevant ASDQ boards. A photograph of this is shown in Figure 6.19. The feedthrough board was then fixed to the snout. Finally the o-ring was covered in vacuum grease, put in place then the lid was secured in position with a torque wrench to seal the lid to the manifold and ensure the lid was attached evenly.

6.9   Module Checks and Data Quality

Before the constructed modules could be shipped to Fermilab, several tests were carried out to ensure that the module could run at an acceptable vacuum, all wires were recording hits correctly and that the module could run at the required HV for a minimum of 2 days. These tests were done by placing the module horizontally into a vacuum chamber to provide the maximum number of cosmic hits for data taking. The module was bolted into the vacuum tank and vacuum sealed using a greased o-ring. The 80:20 Ar:CO_2 test gas was flowed through the module at a rate

Figure 6.19: Photograph of flexi cables and HV internal cables connected to the feedthrough board.

of $0.1\,$LPM into the top manifold, out through the bottom manifold and directed into a bubbler. This was used to check the gas flow. A photograph of the setup is shown in Figure 6.20.

Figure 6.20: Clean room setup for module testing including the vacuum tank on the left and CAEN power supply on the right.

6.9.1   Vacuum testing

The vacuum pump down began with a roughing pump which took it down to $10\,$mbar. Then the turbo pump lowered the pressure to the order of $10^{-6}\,$mbar as required for the experiment. This data was continually monitored as shown in Figure 6.21. If

the module pressure struggled to get below 10^{-3} mbar after one day of pumping, this indicated that the module had a leak which needed to be located. A leak could arise from a hole in the straw wall or the Araldite 2020 gas seal. To look for the leak the module electronics were removed and the module was submerged in water to look for the origin of any air bubbles. This occurred in five modules with a total of six leaking straws being blocked off and not used for data analysis. The vacuum was monitored for several days to ensure that the pressure could remain at the required level.
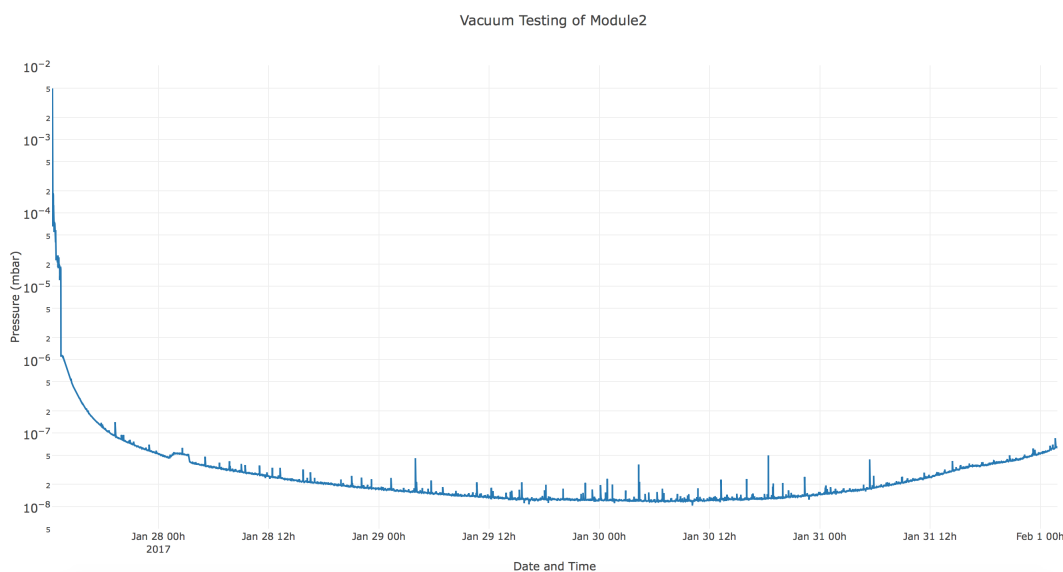
Figure 6.21: Graph of a successful module vacuum pump down to below 10^{-6} mbar. The pressure begins to slowly increase at later times due to the turbo pump being switched off at the end of the test.

6.9.2   Noise scans

Once the required vacuum level had been maintained the frontend electrons as explained in chapter 5 were placed into a custom made box which was fixed to the snout. Noise scans were carried out to ensure that no residual noise from the wires was observed above the 200 mV threshold. This also checked if all the connections to the internal electronics were working and the 16 channels per ASDQ board were all recording data. If channels were not working this could indicate a shorted connection, a broken wire or problems with the HV connection. The threshold was set at 200 mV as this was deemed high enough to cover most of the residual noise from the wires

whilst not losing too many low energy straw hit signals. Noise scans of every channel were tested at three voltages of 1000 V, 1250 V and the near-operating voltage of 1500 V. The actual voltage in the experiment is 1650 V, but Ar:CO_2 breaks down at this value, and could contaminate the wires. If working correctly all the channels at the three voltages should be working identically. A plot of an ASDQ that passed a noise scan is shown in Figure 6.22. For channels that did not work, this showed that the wire connection was faulty or that the wire had a contaminant. This was typically only one or two channels and occurred in 9 modules. Once 1500 V had been successfully reached, the module was left for a day to test if it ran stably. If a failure was observed and it was suspected to be due to a wire contaminant then HV training was carried out. To do this the HV was increased in increments of 100 V from zero until the channel trips. The typical trip voltages for wires was between 800-1200 V. Once the trip voltage was found, the current was increased from $1\,\mu$A to $3\,\mu$A and left at this current for an hour to remove the contaminant. Only three modules required HV training, with one needing HV training on multiple wires. Module 6 had three wires that were successfully HV trained in this manner and all wires were found to have a normal noise scan on re-testing.
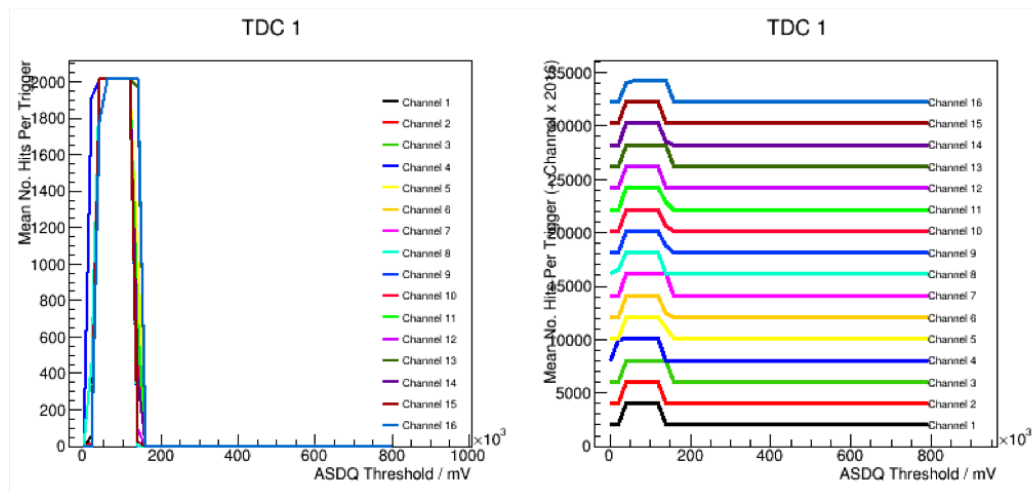
Figure 6.22: Example plot of a noise scan with all channels working correctly.

6.9.3   Module testing using cosmic muon data.

Once all testing had been completed and the vacuum and HV were running stably then DAQ runs with muon cosmic data were taken. A four hour test, which was

the minimum time required to detect hits in all 128 channels, were carried out. If a channel had zero hits in this time it indicated a dead channel. Only five dead channels were found during construction at this point in data quality testing. These wires were all replaced and successfully re-tested. Once any dead channels had been fixed much longer cosmic data runs were needed. This was to ensure that the module could record data stably for a significant amount of time. Plots of long cosmic data runs are shown in Figures 6.23 and 6.24, displaying the hits recorded in all four rows of straws.
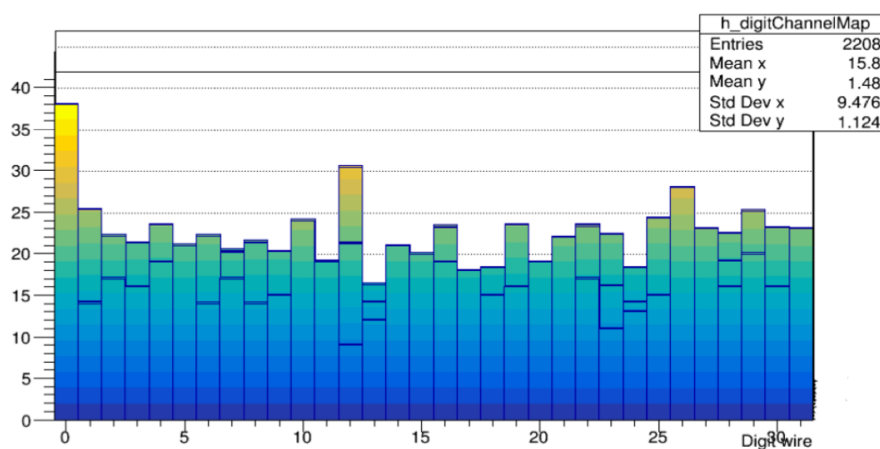
Figure 6.23: A plot of cosmic data channel hits for the four rows of straws.
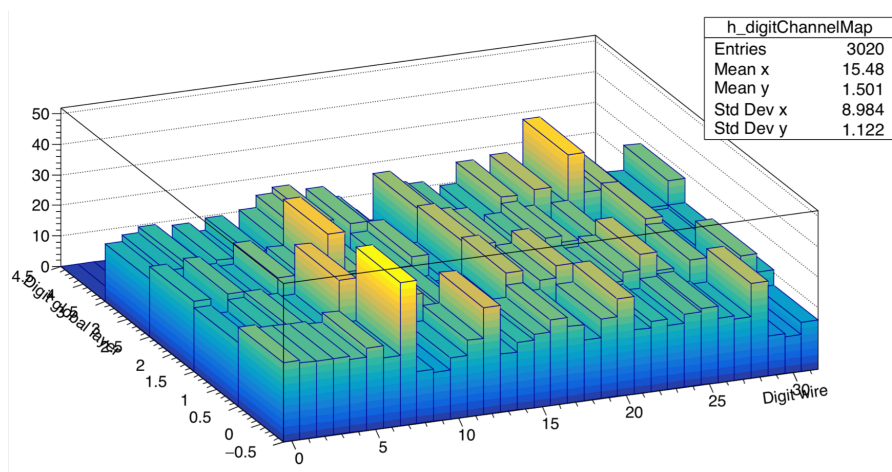
Figure 6.24: A 3D plot showing more clearly the cosmic data channel hits for the four rows of straws.

All modules passed the stringent quality assurance testing and were then readied for shipping to Fermilab. This involved covering the module with perspex shielding and

an antistatic plastic covering before being placed into a pelicase.

6.9.4   Module installation at Fermilab.

Upon arrival at Fermilab, tests were carried out to ensure that the modules were not damaged during transportation. These included noise scans, vacuum tests and gain tests. The modules were then installed into the storage ring vacuum chambers, with data cables, LV and HV cables and cooling pipes attached. Each module was Helium leak tested, ensuring that no leaks were introduced during transport. This was carried out using a mass spectrometer, which was connected to a vacuum port during the storage ring vacuum pump down. By spraying around each module with a small amount of Helium, the amount of Helium present in the vacuum chamber could be measured. All 22 modules were successfully shipped to Fermilab, 16 installed without issue and the remaining 6 modules kept as spares. A photograph of a fully installed tracking station is shown in Figure 6.25. Only the 6 dead channels introduced during the construction process were not in use. All working channels had a noise rate below the 200 mV threshold. The modules all reached the required vacuum to ensure that the storage ring vacuum could attain its target of below 10^{-6} Torr. Thus far the tracking detectors have run extremely stably throughout all data taking periods.

Figure 6.25: A photograph showing an installed tracker station.

Chapter 7

Vertical betatron oscillations

7.1 Introduction

The muon g–2 storage ring acts as a weak focusing betatron. The experiment uses quadrupoles held at an adjustable voltage. The electric field provided by the quadrupoles gives a linear restoring force in the vertical direction, focusing the beam vertically but defocusing radially. However, the combination of the vertical dipole magnetic field and the defocusing radial electric field provides a net linear restoring force in the radial direction and so the beam is focused in both directions. The E-field and the B-field determine the dispersion of the beam, the measurements of which will be the focus of this chapter.

The muons that enter the ring have to pass through the inflector, which is an aperture vertically ~ 15 cm and radially ~ 7 cm wide. These muons do not all have the magic momentum and so the beam has a momentum spread. The restoring forces from the two fields cause the muons to oscillate about an equilibrium position. Vertically, for ideal quadrupoles, the equilibrium position y_e is at the centre of the storage ring ($y = 0$). The radial equilibrium position x_e is determined by the muons momenta. This leads to both the average position and width of the muon beam to exhibit simple harmonic motion called betatron oscillations, in both the radial and vertical directions.

The equations for the horizontal and vertical beam motion are given by

$$x = x_e + A_x \cos(v_x \frac{s}{R_0} + \delta_x), \tag{7.1}$$

$$y = y_e + A_y cos(v_y \frac{s}{R_0} + \delta_y), \tag{7.2}$$

where v_x and v_y are the horizontal and radial beam tunes respectively, s is the arc length along the trajectory, R_0 is the magic radius and δ_x and δ_y are the corresponding phases. The tune is defined to be the number of betatron oscillations per revolution of the storage ring and is related to the strength of the field, characterised by the field index n. The field index is given by:

$$n = \frac{\kappa R_0}{\beta B_0}, \tag{7.3}$$

where κ is the electric quadrupole gradient, $R_0 = 7112\,\text{mm}$ is the radius of the storage ring, β is the relativistic velocity of the muon and B_0 is the magnetic field strength. The corresponding tunes are:

$$v_x = \sqrt{1 - n}, \tag{7.4}$$

$$v_y = \sqrt{n}. \tag{7.5}$$

To determine the oscillation frequencies the tune is multiplied by the cyclotron frequency f_c. For the initial running conditions the quadrupoles were set to $18.3\,\text{kV}$ during data taking, giving a corresponding field index of $n = 0.108$. The resulting horizontal and vertical betatron frequencies are:

$$f_x = f_c\sqrt{1 - n} \simeq 0.94 f_c = 6298\,\text{kHz}, \tag{7.6}$$

$$f_y = f_c\sqrt{n} \simeq 0.33 f_c = 2211\,\text{kHz}. \tag{7.7}$$

Compared to the precession frequency which is:

$$f_a = \frac{e}{2\pi mc} a_\mu B = 229\,\text{kHz}. \tag{7.8}$$

7.1.1   The effect of betatron oscillations on ω_a

Precise knowledge of the muon beam distribution and its behaviour throughout the fill is required to determine the corrections needed to calculate a_μ. This is because as the beam undergoes these radial and vertical oscillations the rate of positrons

measured by the detectors, which have an acceptance that depends upon the decay position, also oscillates. Thus the total number of detected positrons will vary throughout the fill due to the oscillation of the centroid of the beam distribution and the precession of the muon spin. The simple 5 parameter fit function used to fit ω_a is:

$$N(t)_{5par} = N_0 e^{-\frac{t}{\gamma\tau}}(1 + A\cos(\omega_a t + \phi)). \tag{7.9}$$

Where N_0 is an estimate of the number of muons at the start time, $\gamma\tau$ is the average relativistic lifetime of the stored muons, A is the amplitude of the precession oscillation (asymmetry term) and ϕ is the phase of precession at the start time. This is modified to account for the variation in the positron rate due to the betatron oscillations by:

$$N(t) = N(t)_{5par} \cdot N_{CBO}(t), \tag{7.10}$$

with

$$N_{CBO}(t) = 1 + A_{CBO}\cos(\omega_{CBO}t + \phi_{CBO})e^{-\frac{t}{\tau_{CBO}}}. \tag{7.11}$$

Where A_{CBO} is the amplitude of the CBO, ω_{CBO} is the frequency of the CBO term, ϕ_{CBO} is the phase of the CBO at the start time and τ_{CBO} is the lifetime of the CBO. The radial and vertical oscillation frequencies are dependent on the beam momentum distribution, with their oscillation amplitudes being time-dependent. The spread in the accepted muon momentum leads to a range of oscillation frequencies. The storage in the ring is not perfectly harmonic and therefore the muon beam oscillation frequencies are amplitude dependent. This range of oscillation frequencies causes the coherent beam motion to decohere, which manifests itself as a reduction in the beam oscillation amplitude over time. This leads the CBO to decay away exponentially with a lifetime of approximately $300\,\mu s$. The CBO will be described in the following section. The general form for an oscillation term is therefore an exponentially decaying sinusoid. One such term is added for all the observed betatron oscillations. As well as directly affecting N, there are effects from the betatron oscillations on the phase and amplitude in the final ω_a fits.

$$A(t) = 1 + A_A \cos(\omega_{CBO} t + \phi_A) e^{-\frac{t}{\tau_{CBO}}}, \tag{7.12}$$

$$\phi(t) = 1 + A_\phi \cos(\omega_{CBO} t + \phi_\phi) e^{-\frac{t}{\tau_{CBO}}}. \tag{7.13}$$

Here having moved from A and ϕ defined in equation 7.9 to a time dependant A and ϕ, where A_A and ϕ_A refer to the amplitude and phase of the CBO oscillation in the asymmetry term and A_ϕ and ϕ_ϕ are the amplitude and phase of the CBO oscillation of the ϕ term. The relevant betatron oscillations for the Run-1 dataset are defined later in this chapter. In order to minimise the impact of these oscillations on the a_μ measurement tuning is required in order to ensure that the betatron wavelengths are not multiples of the storage ring circumference. If the beam after one full rotation around the ring is situated back in the same exact position then the beam would sample the magnetic field at the same position each time. Any deviations in the magnetic field and quadrupole electric fields will lead to forces that affect the muons orbit with each revolution of the ring. If these forces lie on a resonance then the betatron oscillations will increase and could cause muon loss. Any imperfections in the magnetic field would lead to these field errors accumulating each revolution. Instead the tune is used to ensure that the beam is at a different position every revolution, for example a muon travels slightly more than a full revolution until it gets back to the same radial position, ensuring that the beam samples the whole magnetic field across the azimuth.

The equations used to describe the beam oscillations assume uniform coverage of the quadrupoles. However in the experiment only 43% of the storage ring is covered by the quadrupoles and therefore the equations are only approximate. The focusing strength will change as a function of azimuth around the ring and a measurement of the beam motion at different azimuthal positions is required.

7.1.2   Coherent betatron oscillations

Each stationary tracking detector only observes the beam from one position around the ring and therefore only measures the beam once for each revolution of the storage ring. This means that only frequencies of less than 0.5 f_c can be observed. When

considering the radial width, it is narrow at injection into the storage ring as the entrance is oval shaped; long vertically and narrow radially. Due to the tuning, each muon does not complete a full oscillation until it has done more than one rotation around the ring. This means that the focal point as measured by a stationary detector from injection will move azimuthally during the fill and the width will vary around the ring as the muons orbit it. Furthermore there is an additional focal point at a time of half a betatron period due to the sinusoidal nature of the muons radial position.

The ranges of the field index n used by the experiment mean that the radial beam oscillation frequency is higher than the vertical oscillation. The radial oscillation $f_x > 0.5f_c$ and so instead of observing the true frequency an aliased frequency is measured at a frequency of $f_{CBO} = f_c$ - f_x, which is determined from the Nyquist theorem. The frequency of this is called the Coherent Betatron Oscillation f_{CBO}. The frequency at which a single fixed detector sees the beam coherently moving back and forth radially is given by:

$$f_{CBO} = f_C - f_x = (1 - \sqrt{1 - n})f_C. \tag{7.14}$$

So the oscillation of the radial mean is measured at a lower aliased frequency of f_{CBO}, while the vertical oscillation, which has a frequency $f_y < 0.5f_c$, is measured at its actual frequency. A diagram illustrating this is shown in Figure 7.1. Figure 7.2 gives an illustration of the field index and frequency range that is affected by the aliasing effect for a detector at a fixed azimuthal position. The diagram shows that all the frequencies above $f/f_c = 0.5$ are aliased. The green area indicates the field index values used for the experiment. For f_x its frequency in the green area lies above $f/f_c = 0.5$ and so this frequency is aliased. The dotted orange line shows f_{cbo}, which is measured instead of f_x. F_y is shown by the blue line and lies below $f/f_c = 0.5$ and so it is measured at its correct frequency. $2f_y$, shown in pink also lies above $f/f_c = 0.5$ and so it is measured as f_{VW} instead. This is shown by the dotted pink line. This measured frequency is given by the equation:

$$f_{VW} = f_C - 2f_y = (1 - \sqrt{n})f_C. \tag{7.15}$$

Where the f_{VW} refers to the frequency of the vertical waist, the term used to describe the vertical width of the beam.
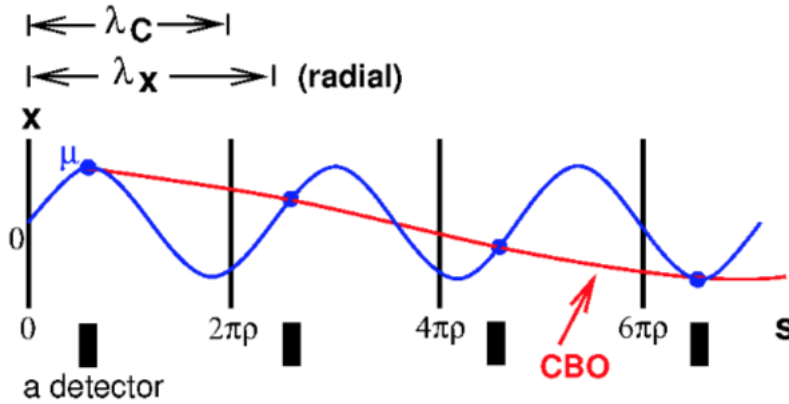
Figure 7.1: An illustration of the coherent betatron oscillation (CBO). Showing in blue the radial betatron oscillation for several wavelengths. In black is the cyclotron circumference. As the radial betatron oscillation has a wavelength longer than the storage ring circumference the detector observes the muon beam to be moving closer to it and then move further away. The frequency that the detector samples this beam motion is the f_{CBO} which is shown in red [2].

The calorimeter detector acceptance is dependant on the radial and vertical position of the muon's decay. These beam positions are determined from the track extrapolation. The track is extrapolated back to the point of radial tangency, where the positron momentum is parallel to the magic momentum. On average the vertical position at this point is a good approximation of the vertical position of the decay, with the per track vertical position resolution being 2.7mm.

The muon beam distribution oscillates during the fill which will cause the rate of positrons measured to oscillate due to detector acceptance. This shows up as an amplitude modulation of the decay positron time spectrum data. Any change in the betatron frequencies during the fill results in a systematic error on the ω_a measurement. The betatron frequencies themselves have frequencies much larger that f_a and so do not affect the ω_a measurement directly. Careful consideration must be taken when setting the CBO frequency, which is close to the second harmonic of $f_a = \omega_a/2\pi$. If the CBO frequency is too close to $2f_a$, the beat frequency $f = f_{CBO} - f_a$ complicates determining f_a from the data, which would introduce a systematic error [2].
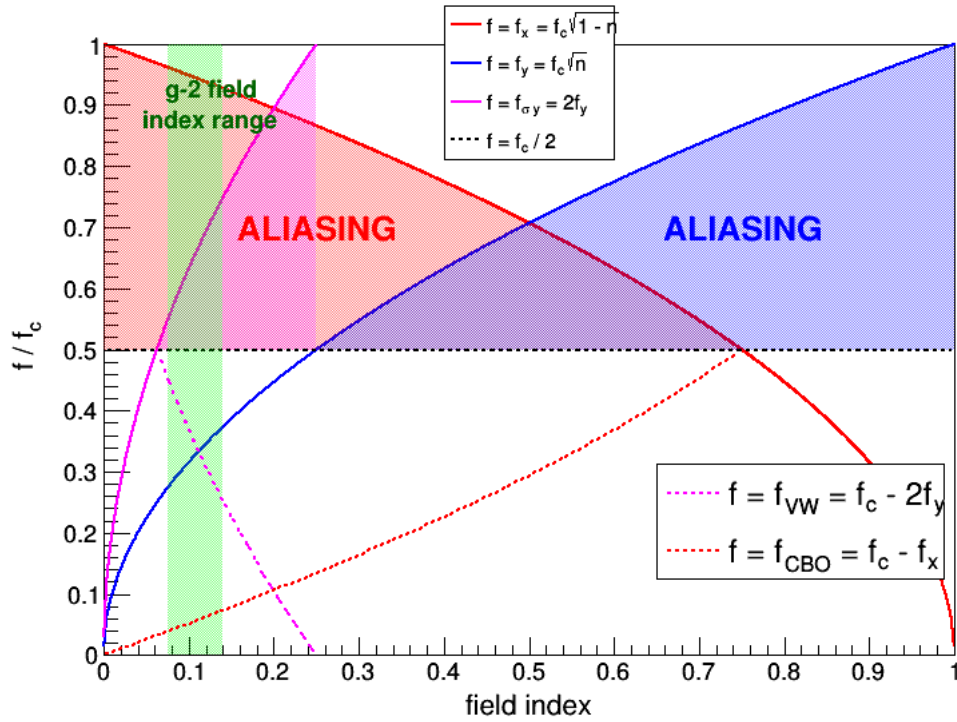
Figure 7.2: For a range of field indices several frequencies are plotted. The range of field indices used in the experiment is shown in green. The Nyquist band, at $f_c/2$, is also displayed. The detectors can only measure frequencies less than $f_c/2$, therefore aliasing occurs at frequencies above this.

For the 2000 run at BNL the f_{CBO} did in fact lie close to the second harmonic of f_a and affected the ω_a determined from fits of the data. This has been avoided for this experiment by selecting the right field strength. The quadrupole voltages that the experiment ran at for Run-1 were $18.3\,\mathrm{kV}$ and $20.4\,\mathrm{kV}$.

Care must be taken to avoid resonances when choosing the operating quadrupole voltage. Otherwise the beam distribution would expand and therefore cause loss of muons. Spin resonances could also occur. This is where the vertical spin is slightly rotated with each betatron cycle and slowly increases throughout the fill. These effects will slowly add up and lead to a phase change of the ω_a oscillation, affecting its measurement.

7.1.3   Lost muons and beam scraping

Muons at the outer limits of the storage radius have a higher likelihood of being lost at early times. The muons which leave the storage region before decay are referred

to as lost muons. These cause a deviation in the muon exponential decay curve, which affects the ω_a fits and leads to a shift in the ω_a calculated. Muons which lie on the outer edge of the muon beam distribution and are outside of the storage ring radius are removed by a process called scraping. This is where an asymmetric charge is placed on the electrostatic quadrupoles at early times causing the centroid of the beam to move radially and vertically by $\sim 2\,\mathrm{mm}$, forcing the muons at the edge of the distribution into the path of the collimators. This causes those muons to scatter, curl inwards and leave the storage ring [80]. The quadrupoles are then restored to their nominal values $13\,\mu s$ after beam injection and the remaining muons are stored. The vertical displacement of the muon beam distribution measured by the tracking stations over the course of the scraping period is shown in Figure 7.3. The binning chosen here was larger than the period of the expected oscillations so that only the effect of scraping can be seen and not the beam oscillation. The ω_a fits do not start until $30\,\mu s$ so that the effects of scraping are no longer present and the muon beam and corresponding betatron oscillations are constant throughout the fitting range. However a small amount of muons will continue to be lost at later times. This could be due to perturbations in the storage rings magnetic and electric fields or by scattering with residual gas in the storage ring. Also with the radial and vertical betatron oscillations of the beam distribution adding to this. When these muons are eventually lost they curl inwards and are capable of travelling through several calorimeters, depositing $\sim 170\,\mathrm{MeV}$ in each. Therefore calorimeter pileup events with an energy below $500\,\mathrm{MeV}$ are consistent with two muons. However events with energies between 1.8 - 3.2 GeV are not. These could be either two low energy positrons or a muon and a positron. Additionally muons are also more likely to produce a signal in just one crystal in the calorimeter. This is because they are much less ionising and do not produce an electromagnetic shower whereas positrons can deposit energy in several crystals. Muons are identified by low energy double or triple coincidences with neighbouring calorimeters. The coincident muons in neighbouring calorimeters are determined by a signal time window with a time of flight of 6.25±0.5 ns [81] for each adjacent calorimeter. The lost muon candidates can also be cross checked with the tracking detector information. By applying cuts and subtracting backgrounds, a spectrum of lost muons can be built up. The lost muon spectrum can then be added

into the ω_a fit function. This is done to account for the positrons that would have been observed at later times in the fill if there were no muon losses.
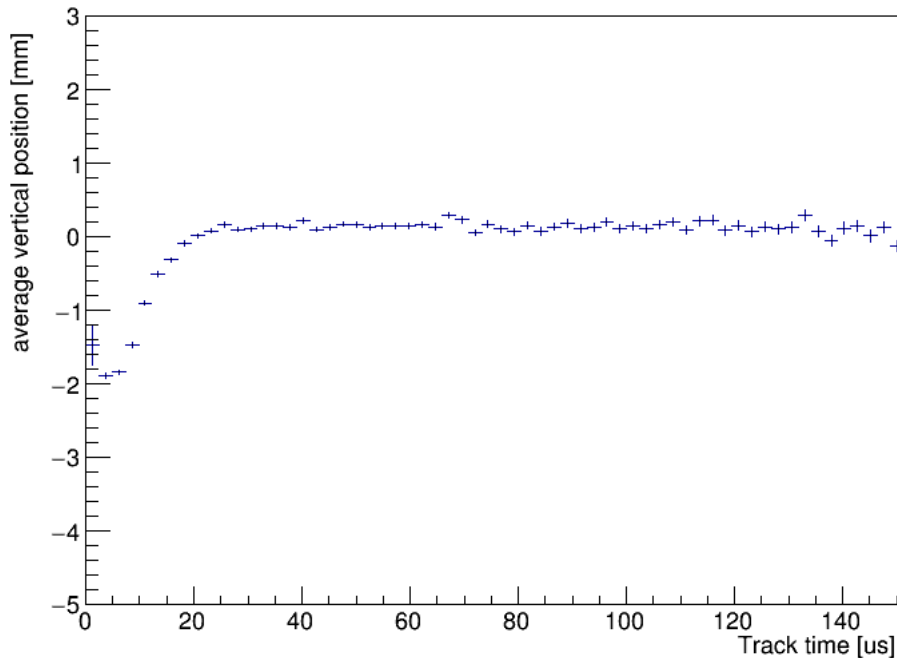
Figure 7.3: Measurement of the vertical displacement of the muon beam centroid at tracking station 12 during the scraping period.

7.2   Corrections to ω_a measurement

After accounting for the lost muons ω_a is extracted from the calorimeter data. There are two additional corrections that need to be applied, due to beam related effects, the so-called E-field and pitch corrections. As mentioned in chapter 3, the storage ring muons are chosen to be at the magic momentum and as such the quadrupole electric field does not affect ω_a directly. However corrections are required to account for muons not at the magic momentum (E-field correction) or not travelling perfectly perpendicular to the magnetic field (pitch correction). The size of the corrections are expected to be of order 450 and 200 ppb [2] respectively, with a targeted combined uncertainty <50 ppb.

7.2.1 Radial electric field corrections

The muon beam distribution is dependant on the phase space acceptance of the beam injection point at the inflector, the storage ring itself and the kick provided by the kicker to place the beam onto the magic storage radius. The storage ring momentum acceptance is $\pm 0.15\%$ [2] either side of the magic momentum and so there is a range of muon momenta around that value. For muons with momenta not equal to the magic momentum $p_m = 3.094\,\text{GeV/c}$, the precession frequency is given by:

$$\omega'_a = \omega_a \Big[1 - \beta \frac{E_r}{cB_y} \Big(1 - \frac{1}{a_\mu \beta^2 \gamma^2} \Big) \Big], \tag{7.16}$$

where E_r is the radial component of the electric field and B_y is the vertical component of the magnetic field. By use of $p = \beta \gamma m = (p_m + \Delta p)$, the fractional difference in ω_a is determined by:

$$\frac{\Delta \omega_a}{\omega_a} = -2 \frac{\beta E_r}{cB_y} \Big(\frac{\Delta p}{p_m} \Big). \tag{7.17}$$

Hence this effect leads to a reduction in the measured frequency and alters the expression for ω_a given in equation 3.7. Therefore the effect of the electric field cannot be completely ignored as doing so causes a bias in the ω_a value. To determine the correction required for the electric field the equilibrium radial distribution of the muon beam is required. This can be measured by analysing how the bunch structure evolves during the fill, a so-called fast rotation analysis. A beam with a range of momenta will undergo debunching. This is where muons with higher momenta will have the largest orbits and so will take the longest time to travel once around the ring, while the lowest momentum muons will take the lower orbit and so complete one cycle around the storage ring in a shorter time. Eventually after many cycles around the ring the low momentum muons will overtake the high momentum muons and will do so multiple times as the muon beam circulates the storage ring. This leads to a stretching of the muon bunch structure until the beam becomes uniform and the bunch structure is lost. The bunch structure is mostly lost by 60 μs [82]. The fast rotation analysis is carried out using calorimeter data, and is confirmed by the equilibrium position of the radial CBO as measured by the trackers. To study the beam momentum distribution, the data from all calorimeters are aligned together in

time and plotted in 1 ns bins to observe the fast rotation. A Fast Fourier Transform (FFT) of the data is performed to observe the different frequencies in the beam distribution. This data is converted into time and then into the muon storage radius to observe the corresponding distribution in radii. If muon storage in the ring was perfect then all muons should lie on the magic radius of 7112 mm. Their deviation from this value gives the distribution spread of the muon beam, from which the electric field correction can be calculated. In the 2001 BNL dataset, the electric field correction for the low n-value dataset was $+0.47 \pm 0.05$ ppm [1].

7.2.2 Pitch correction

The measured ω_a value requires a correction due to the vertical beam motion of the beam. In equation 3.13 it was assumed that the muon beams velocity is perpendicular to the magnetic field, thus the equation is simplified by the assumption that $B \cdot \beta = 0$. However this is an approximation and for the high level of precision required for the ω_a measurement a correction is needed to account for the vertical betatron oscillations, where the muons velocity is not exactly perpendicular to the storage ring magnetic field. A simplistic illustration of vertical betatron oscillations is shown Figure 7.4.

The pitch correction is so-called because during vertical betatron oscillations, the pitch angle ψ, defined to be the angle between the momentum and the horizontal axis, varies harmonically with $\psi = \psi_0 \cos(\omega_y t)$. Where ω_y is the vertical betatron frequency $\omega_y = 2\pi f_y$ with $\omega_y = 2\pi\sqrt{n}f_c \simeq 2\pi \times 2.2$ MHz. It is illustrated in Figure 7.5.

Using the assumption that the muons are all circulating on the magic radius, then $a_\mu - 1/(\gamma^2 - 1) = 0$ giving[1]:

$$\vec{\omega_{a_\mu}} = -\frac{q}{m}[a_\mu\vec{B} - a_\mu\Big(\frac{\gamma}{\gamma + 1}\Big)(\vec{\beta} \cdot \vec{B})\vec{\beta}]. \tag{7.18}$$

The coordinate system used in Figure 7.5 has y as the vertical axis, the z axis is the direction of propagation and $\vec{\beta}$ lying in the zy-plane. The x and z axes rotate with the angular frequency:

---

[1]This derivation originates from the muon g–2 technical design report [2].
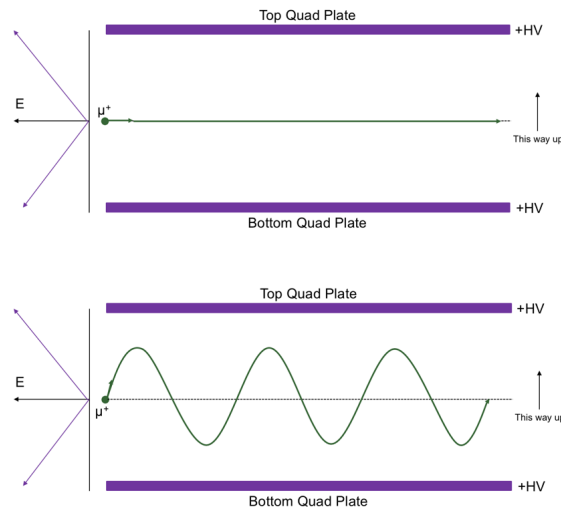
Figure 7.4: Simplistic diagram of vertical betatron oscillations. If the muons were injected into the ring at y = 0 and with no vertical momentum then the muon would stay perfectly horizontal as it travels through the ring until it decayed, as shown in the top diagram. However the muons are not injected perfectly and so will posses a non-zero vertical momentum. The muons will then oscillate due to the restoring force from the quadrupole electric field, with the amplitude of the oscillation dependant on its initial direction as shown in the bottom diagram.

Figure 7.5: A diagram showing the coordinate system of the pitching motion, y = vertical direction, z = azimuthal beam direction [2].

$$\omega = \frac{q}{m\gamma} B_y. \tag{7.19}$$

The equation for the transverse component of ω can be determined by use of the

standard rotation formula:

$$\omega_\perp = \omega_{a_\mu} = \omega_y \cos\psi - \omega_z \mathrm{sin}\psi. \tag{7.20}$$

Using the assumptions:

$$\vec{B} = \hat{y}B_y, \tag{7.21}$$

$$\vec{\beta} = \hat{z}\beta_z + \hat{y}\beta_y = \hat{z}\beta\cos\psi + \hat{y}\beta\sin\psi, \tag{7.22}$$

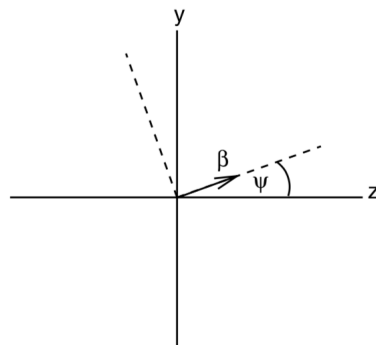$$\vec{\omega_{a_\mu}} = -\frac{q}{m}[a_\mu\hat{y}B_y - a_\mu(\frac{\gamma}{\gamma+1})\beta_y B_y(\hat{z}\beta_z + \hat{y}\beta_y)], \tag{7.23}$$

the equation below is derived:

$$\omega_{a_y} = -\frac{q}{m}a_\mu B_y\Big[1 - (\frac{\gamma}{\gamma+1})\beta_y^2\Big] = -\frac{q}{m}a_\mu B_y\Big[1 - (\frac{\gamma}{\gamma+1})\beta_y^2\frac{\beta_y^2}{\beta^2}\Big]. \tag{7.24}$$

Using:

$$\frac{\beta_y}{\beta} = \sin\psi \simeq \psi, \frac{\gamma\beta^2}{\gamma+1} = \frac{\gamma-1}{\gamma}, \tag{7.25}$$

gives:

$$\omega_{a_y} = \omega_a[1 - (\frac{\gamma-1}{\gamma})\psi^2] \tag{7.26}$$

ω_{a_z} is given as:

$$\omega_{a_z} = -\frac{q}{m}a_\mu B_y(\frac{\gamma}{\gamma+1})\beta_y\beta_z = -\frac{q}{m}a_\mu B_y(\frac{\gamma}{\gamma+1})\beta^2\frac{\beta_y^2}{\beta^2}\frac{\beta_z}{\beta_y}. \tag{7.27}$$

Using:

$$\frac{\beta_y}{\beta_z} = \tan\psi \simeq \psi, \tag{7.28}$$

ω_{a_z} becomes:

$$\omega_{a_z} = -\omega_a(\frac{\gamma-1}{\gamma})\psi. \tag{7.29}$$

The vertical betatron oscillation frequency f_y is approximately ten times faster than the g–2 oscillation frequency f_a. As vertical betatron oscillates ten times per g–2 oscillation, its effect on ω_a is averaged out, leading to $\omega_a \simeq \omega_\perp$ [26]. Substituting equations 7.26 and 7.29 into equation 7.20 gives:

$$\omega_a \simeq \frac{q}{m} a_\mu B_y (1 - \frac{\psi^2}{2}) = -\frac{q}{m} a_\mu B_y (1 - \frac{\psi_0^2 cos^2 \omega_y t}{2}). \qquad (7.30)$$

Taking the time average of the oscillation yields the pitch correction C_p and using the equation relating the maximum allowed angle, ψ_0, and the field index $< \psi_0^2 > = n < y^2 > / R_0^2$ gives the pitch correction [2] [83]:

$$C_p = -\frac{< \psi^2 >}{2} = -\frac{< \psi_0^2 >}{4} = -\frac{n}{4} \frac{< y^2 >}{R_0^2}. \qquad (7.31)$$

The vertical oscillations reduce the magnitude of ω_a and so the correction needs to be added to increase the value. In the 2001 BNL dataset, the pitch correction was $+0.27 \pm 0.04$ ppm [1].

The following analyses used two datasets from Run-1: the 60 hour dataset and the 9 day dataset. Before looking at the oscillations the average vertical position and vertical width were studied to characterise the overall behavior of the vertical components of the beam throughout the fill. These are shown in Figures 7.6 and 7.7. It can be seen that up to $30\,\mu s$ the beam is narrowing due to scraping as expected. After $30\,\mu s$ however both distributions should be flat and this is not observed in either distribution. This decrease in the vertical width should only have a tiny effect on the pitch correction calculated. To check this, the calculation of the pitch correction at two times throughout the fill was done using the vertical width distribution in Figure 7.7 at station 12. One at an early time of $30\,\mu s$ which had a vertical width of $13.05\,$mm and at a late time of $300\,\mu s$ which had a vertical width value of $12.70\,$mm. A $C_p = 182\,$ppb was calculated at $30\,\mu s$ and $C_p = 172\,$ppb at $300\,\mu s$. Therefore the unexpected variation of the vertical width only leads to a $10\,$ppb effect on the pitch correction which is lower than the 30–$50\,$ppb error expected for the Run-1 dataset and lies within specifications. However while this has only a small effect on the pitch correction value, the change in the beam position and width throughout the fill will have an effect on the ω_a fits and therefore this must be quantified and account for.
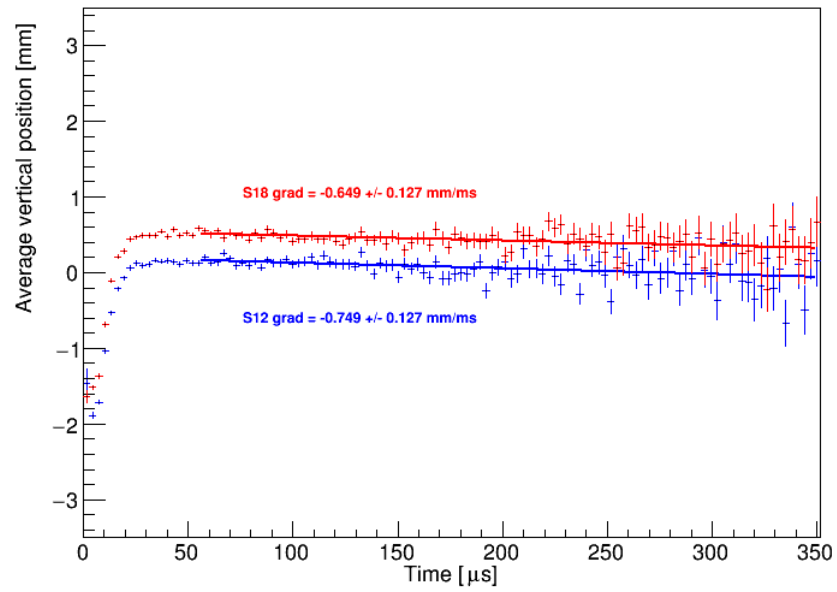
Figure 7.6: A plot showing the average vertical position of the beam for both tracking stations (station 12 in blue and station 18 in red) showing an unexpected decrease throughout the fill.
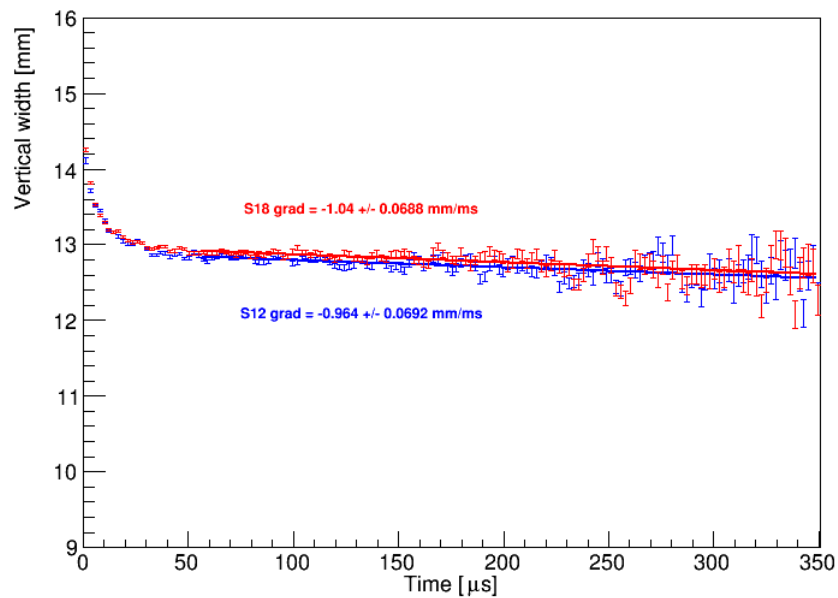

Figure 7.7: A plot showing the vertical width position of the beam for both tracking stations (station 12 in blue and station 18 in red) showing an unexpected decrease throughout the fill.

7.3   Vertical betatron oscillations

Before the observed change in the mean and width during the fill the vertical beam frequencies were expected to be constant, but one explanation for them changing was that the quadrupole voltage was changing in an unexpected way during the fill. This would lead to the betatron frequencies also changing. To investigate this the extrapolated vertical position as a function of time from the trackers was used. The frequencies expected have a period of $\sim 450\,\text{ns}$, therefore the binning chosen was $50\,\text{ns}$. The average vertical position within each time bin is plotted versus time in the fill. A fit is then applied, using a constant frequency as shown in Figures 7.8 and 7.9.

Figure 7.8: A plot of the average vertical position throughout the fill measured at station 12. It shows that at early times oscillations are clearly visible and can be fitted well. The fit becomes worse a later times as the oscillations become less clearly visible.

An oscillation can clearly be seen in early times, but at later times there is beam decoherence due to the momentum spread of the beam distribution. The $\chi^2 = 1.89$ from the simple fit using a constant frequency is unacceptably large, as looking at

the fit throughout the fill a varying frequency is observed. Previously there had been evidence of a varying frequency in the radial beam oscillations and the fact that there was also evidence for this in the vertical beam oscillations indicated that the quadrupole field was indeed varying throughout the fill. This variation needed to be characterised more precisely so that it could be included in the ω_a fit function, and not distort the extracted value of ω_a.
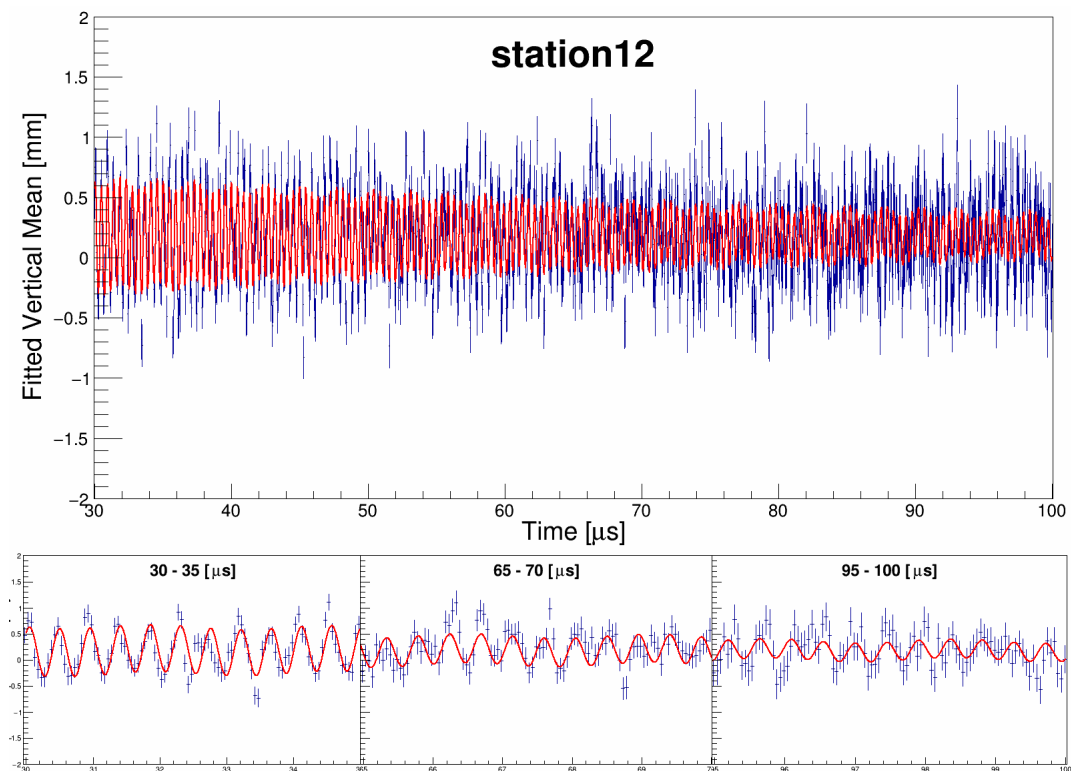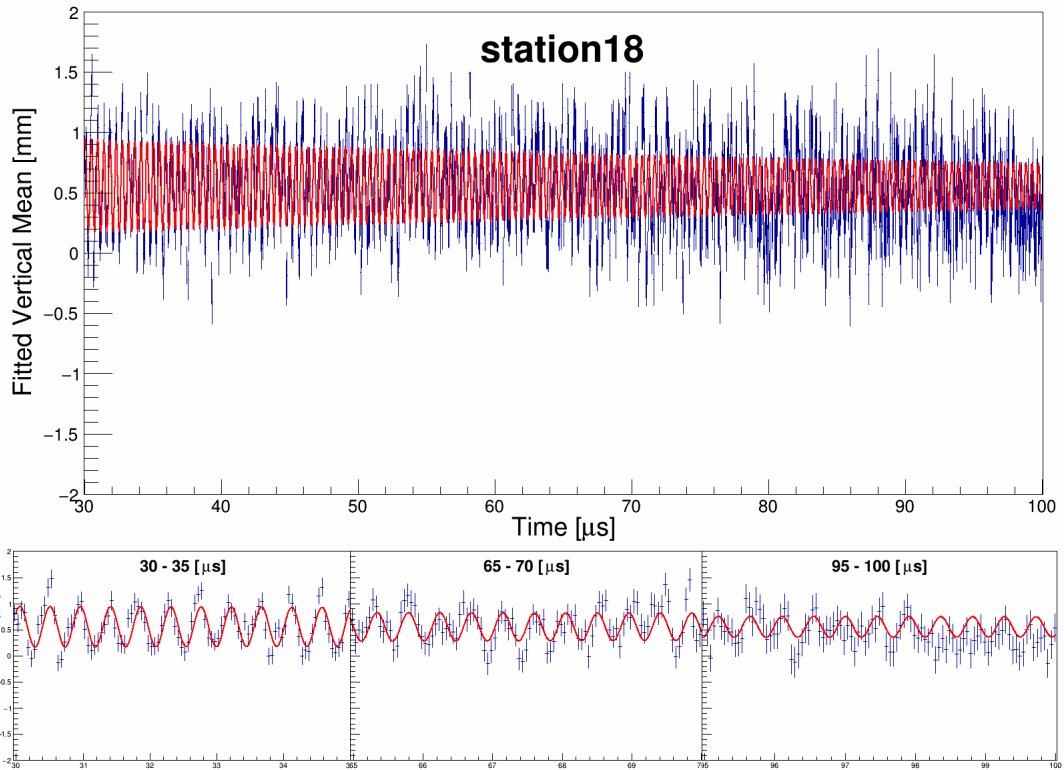

Figure 7.9: A plot of the average vertical position throughout the fill measured at station 18. It shows that at early times oscillations are clearly visible and can be fitted well. The fit becomes worse a later times as the oscillations become less clearly visible.

7.4   Varying beam oscillation frequencies

As mentioned previously, the oscillation of the radial mean has a longer period and therefore is easier to measure with limited statistics. The variation in the radial frequency can be converted into an expected variation vertically using equation 7.32. However the equations are for ideal conditions (complete quadrupole coverage), so it is crucial to measure the vertical frequency variation independently. To investigate this variation in frequency further, time slices from the average vertical position were then taken and a Gaussian fit in the range ± 35 mm was performed to each time slice to obtain the vertical mean and vertical width. It can be seen from the plots in Figure 7.10 that the width as well as the mean is varying throughout the fill. Figure 7.11 and Figure 7.12 show the results of the fit in a $5\,\mu$s time slice from 20–$25\,\mu$s for the vertical width and vertical mean for station 12 and station 18 respectively. Looking at these distributions it can be seen that there are multiple frequencies in both. The individual frequencies present in the distributions can be determined by doing an FFT on the vertical width and vertical mean. Figures 7.13 and 7.14 show the FFT for the fitted vertical mean (in blue) and the vertical width (in red) with the individual frequencies labelled for station 12 and station 18 respectively. However an FFT is not the most accurate method for obtaining the frequency values, particularly when looking for variations in frequency. Therefore fits were applied to the distributions to obtain more accurate frequency values, using the main frequencies from the FFT results as the initial guesses for the fit. Here 3 iterations of fits were carried out. The distributions were then split up into $10\,\mu$s sections (as we have limited statistics) and fitted separately to look for variation/trends throughout the fill. Table 7.1 shows the difference in the frequencies observed in the FFT from Figure 7.13, which was calculated using the field index $n = 0.108$ and the frequencies calculated using the final fit for the whole fill. Figures 7.15 – 7.22 show the fits for the vertical mean, vertical width and fit residuals for both stations at 30–$40\,\mu$s, where the fits are very successful and 30–$100\,\mu$s, which shows that the distributions become harder to fit at later times.
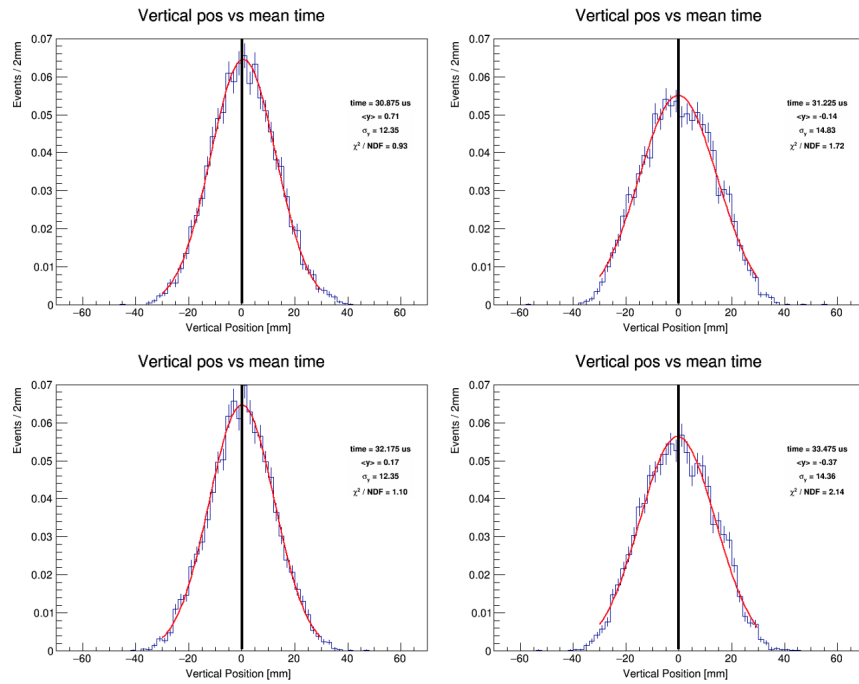
Figure 7.10: Plots showing the Gaussian fits for several time slices. It can be seen that the vertical mean and width are varying with time.

Figure 7.11: Comparison of the mean and width distributions for station 12 at early times of 20–25 μs, showing that a mixture of frequencies are present in the distribution.
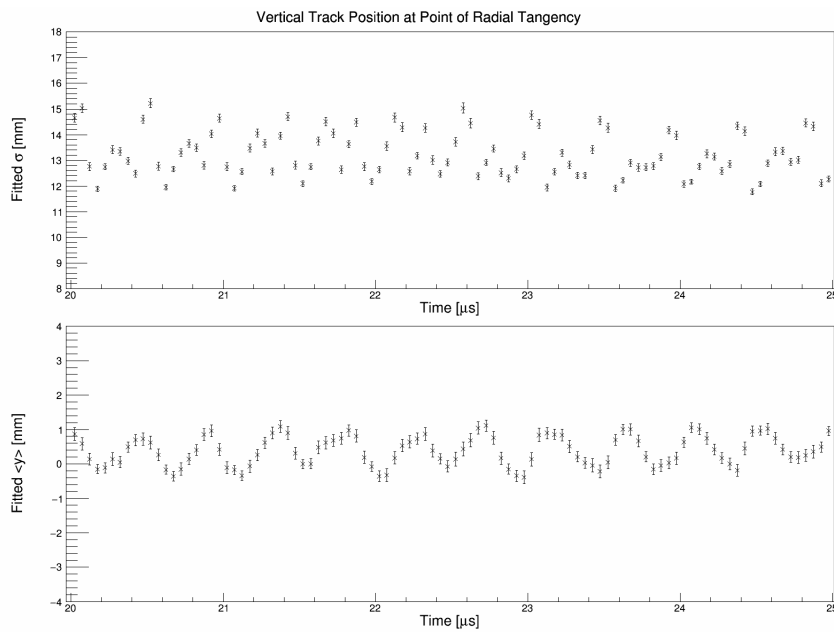
Figure 7.12: Comparison of the mean and width distributions for station 18 at early times of 20–25 μs, showing that a mixture of frequencies are present in the distribution.
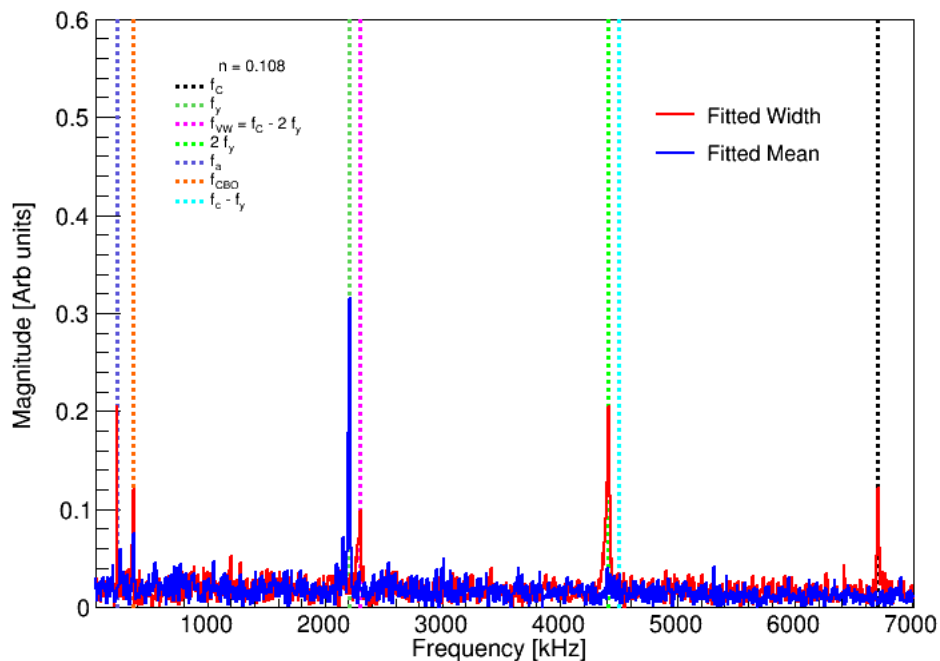
Figure 7.13: The FFT measured at station 12 using data throughout the whole fill. This shows the various frequencies present in the vertical width and mean distributions throughout the fill.

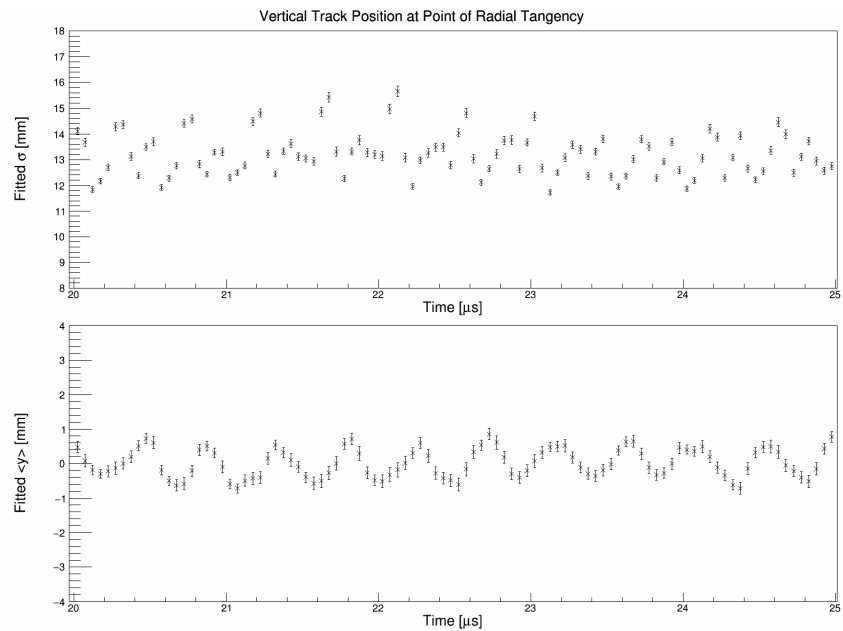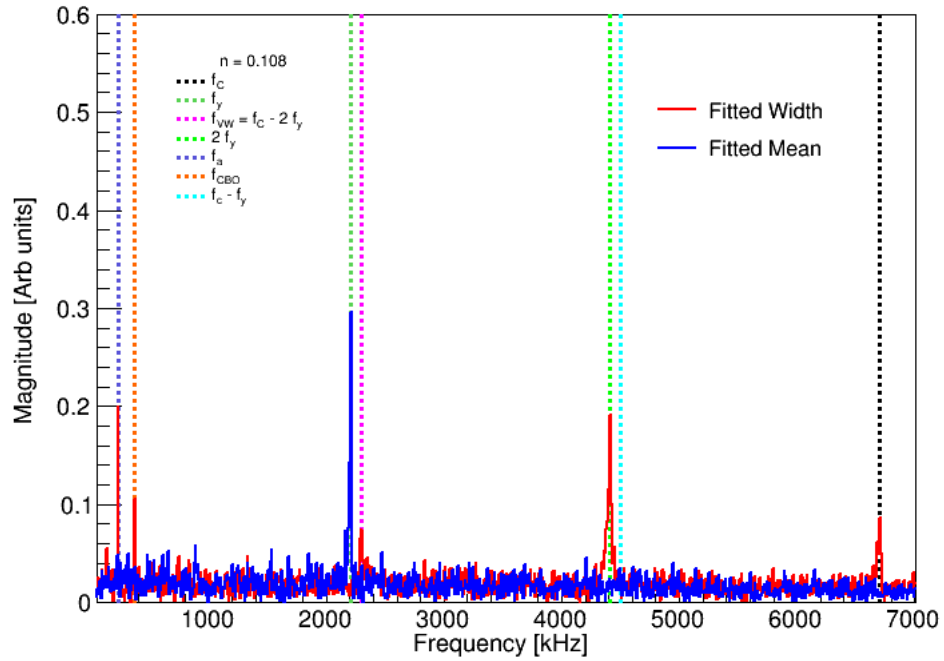Figure 7.14: The FFT measured at station 18 using data throughout the whole fill. This shows the various frequencies present in the vertical width and mean distributions throughout the fill.
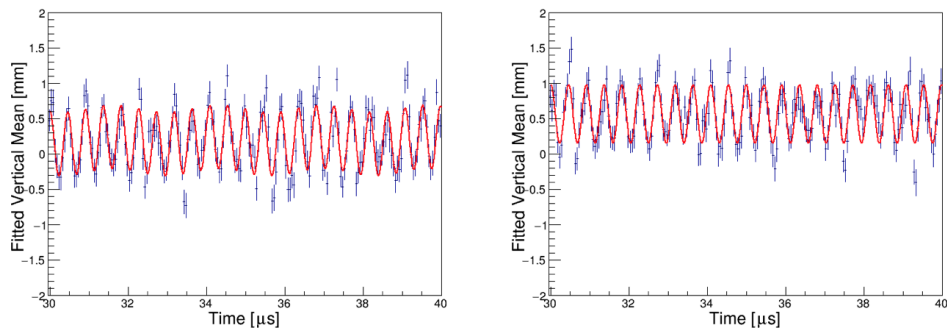
Figure 7.15: Plots of the fitted vertical mean in a $10\,\mu$s time slice between $30\,\mu$s and $40\,\mu$s measured at station 12 on the left and station 18 on the right.

Figure 7.16: Plots of the vertical mean fit residuals between $30\,\mu$s and $40\,\mu$s measured at station 12 on the left and station 18 on the right.
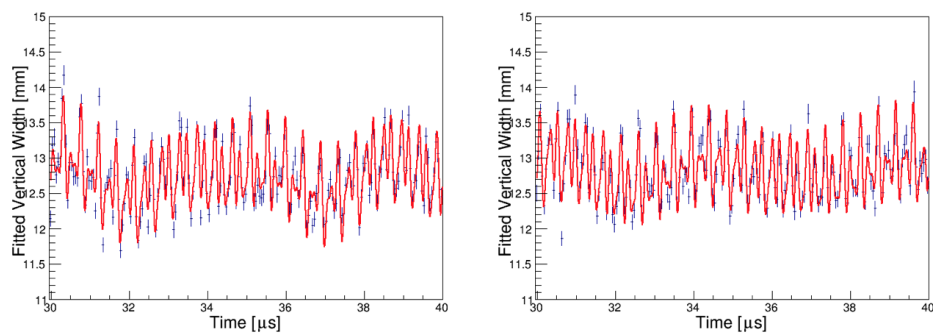
Figure 7.17: Plots of the fitted vertical width in a $10\,\mu$s time slice between $30\,\mu$s and $40\,\mu$s measured at station 12 on the left and station 18 on the right.
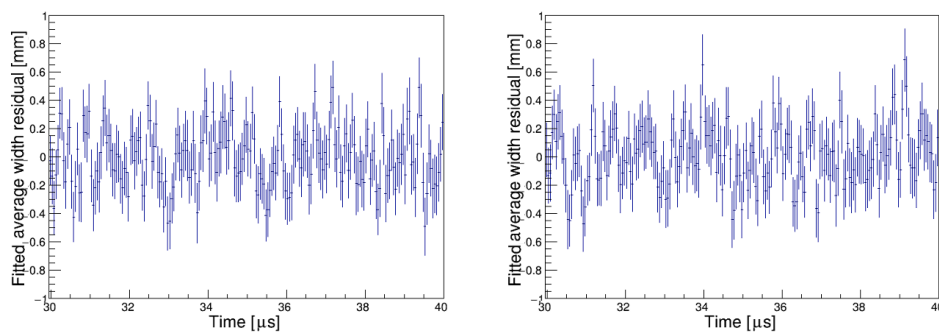
Figure 7.18: Plots of the vertical width fit residuals between $30\,\mu$s and $40\,\mu$s measured at station 12 on the left and station 18 on the right.
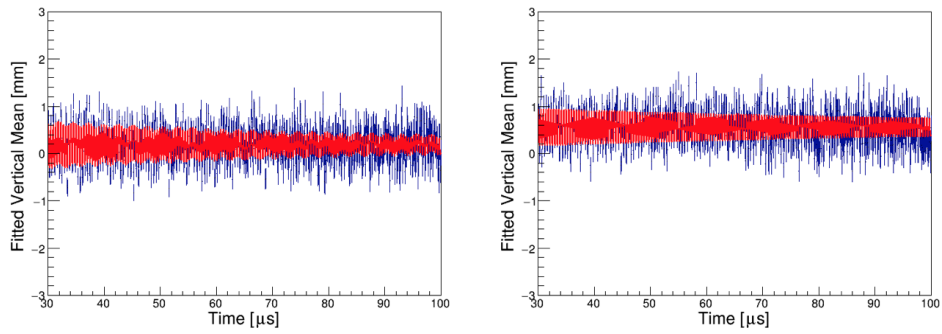
Figure 7.19: Plots of the final fitted vertical mean in over $70\,\mu$s between $30\,\mu$s and $100\,\mu$s measured at station 12 on the left and station 18 on the right.
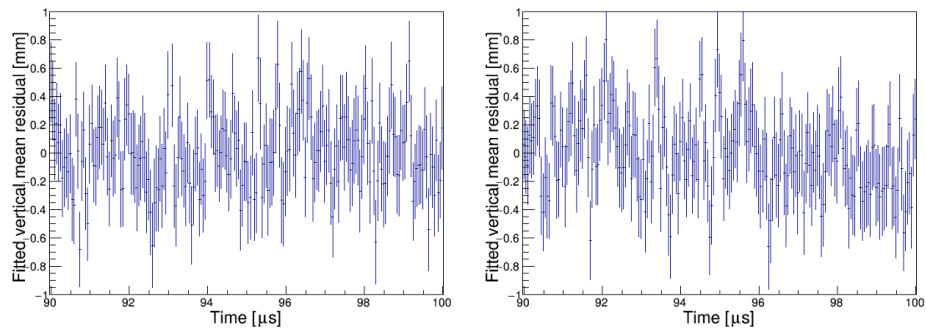
Figure 7.20: Plots of the vertical mean fit residuals between $90\,\mu$s and $100\,\mu$s measured at station 12 on the left and station 18 on the right.
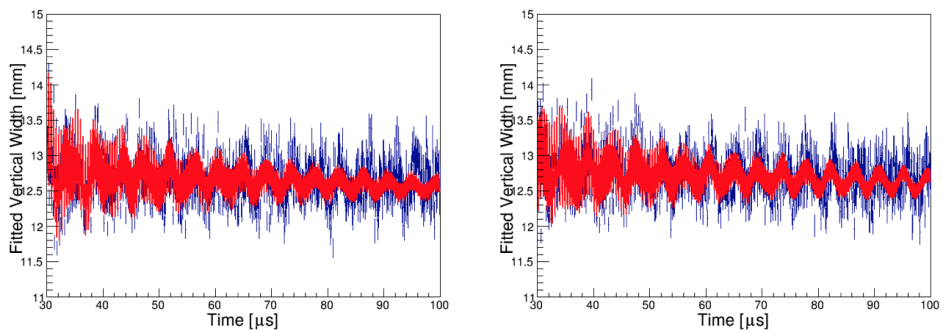
Figure 7.21: Plot of the final fitted vertical width in over $70\,\mu$s between $30\,\mu$s and $100\,\mu$s measured at station 12 on the left and station 18 on the right.
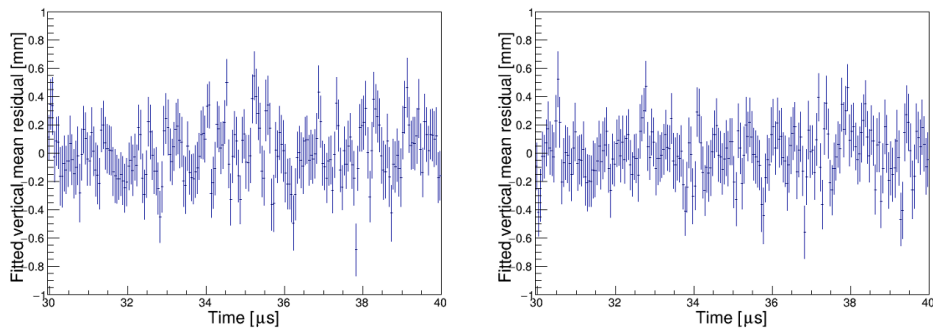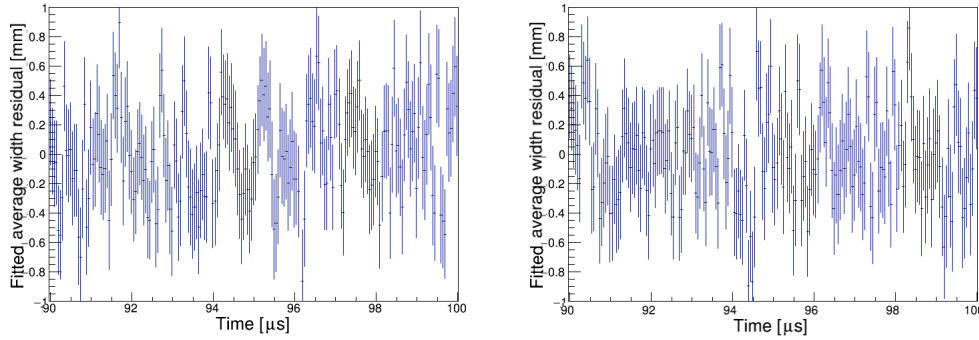
Figure 7.22: Plots of the vertical width fit residuals between $90\,\mu\text{s}$ and $100\,\mu\text{s}$ measured at station 12 on the left and station 18 on the right.

Quantity	Expression	Expected Freq. [MHz]	Period [μs]	Fitted Freq. [MHz]	Period [μs]
f_a	$\frac{e}{2\pi mc}a_\mu B$	0.229	4.37	0.222	4.505
f_c	$\frac{\nu}{\pi R_0}$	6.711	0.149	6.711	0.149
f_y	$\sqrt{n}f_c$	2.202	0.454	2.209	0.453
f_{CBO}	$f_c - f_x$	0.372	2.688	0.376	2.667
f_{VW}	$f_c - 2f_y$	2.296	0.436	2.297	0.435

Table 7.1: Frequencies in the g–2 storage ring for the 60 hour data with a field index of $n = 0.108$, showing the frequencies determined for the FFT along with the frequencies calculated using the fit for the whole fill.

7.4.1   Comparison with radial frequency variation.

The relationship between the vertical betatron oscillation frequency and the radial CBO frequency is shown below:

$$f_y = f_{CBO}\sqrt{\frac{2f_c}{f_{CBO}} - 1}. \tag{7.32}$$

This is derived from equations for continuous quadrupoles rather than the segmented quadrupoles of the experiment.
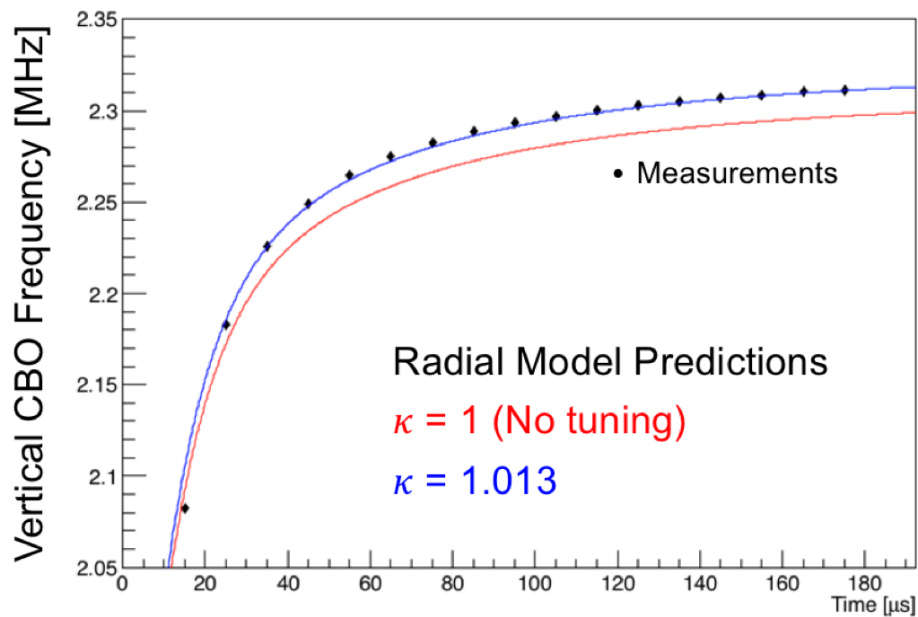
Figure 7.23: Comparison of the vertical CBO oscillation calculated using the vertical betatron oscillation and the vertical CBO observed experimentally. A tuned factor of 1.013 is required to create an agreement between the two values.

Figure 7.23 displays the observed vertical CBO frequency distribution obtained from the $10\,\mu$s fits to the tracker data. The measurements are the black dots, the red line is calculated using equation 7.32. In order to obtain a good agreement between the two, an additional multiplicative factor needed to be applied to f_y. This factor corresponds to a 1.3% increase, and is attributed to the equations being based on 100% quad coverage, which is not the case in the experiment. With this factor established, it is now possible to convert between the measured variation in frequency radially and vertically. This is important because the radial CBO, and its variation

throughout the fill, can be fitted more precisely than the vertical frequencies. Although the fit is still not perfect after the addition of the scaling parameter κ, it is accurate enough for the Run-1 level of statistics, and helps improve the ω_a fits. The impact of adding the variation of the vertical oscillations to the ω_a fits, including this parameter is discussed in the next section.

7.5 Fitting ω_a

The ω_a fit, first introduced in equations 7.9 – 7.13 is shown in full below:

$$N(t) = N_0 e^{-\frac{t}{\gamma\tau}}(1+A{\cdot}A_{BO}(t)\mathrm{cos}(\omega_a t+\phi{\cdot}\phi_{BO}(t)){\cdot}N_{CBO}(t){\cdot}N_{VW}(t){\cdot}N_y(t){\cdot}N_{2CBO}(t){\cdot}J(t).$$

(7.33)

This equation includes terms from every frequency in the muon beam distribution and a lost muon contribution $J(t)$.

For the 60 hour dataset, the ω_a fits can be performed and yield acceptable χ^2 values with a constant vertical waist frequency, even though the variation in the radial frequency must be accounted for. This is because the period of the radial CBO is longer, as is the lifetime. However the variation in the vertical waist must be accounted for once the statistics increase, for example for the 9 day dataset, which has approximately 3 times the statistics. The ω_a fits for the 9 day dataset before and after the scaling parameter κ is included are shown in Figure 7.24. The effect of the addition of the scaling parameter κ is seen by looking at the FFT of the residuals from the ω_a fits. The top plot in Figure 7.25 shows the residuals when constant frequencies of f_{VW} and f_y are used. There are clearly still residuals remaining at these frequencies, which are not accounted for in the fitting functions. The bottom plot in Figure 7.25 shows the same fits, except this time the observed variation in f_{CBO} is converted and applied to the f_{VW} and f_y frequencies, including a free parameter which is the equivalent of κ in Figure 7.23. The value of this parameter, obtained from fits to the calorimeter data is $\sim 1\%$, which is consistent with the κ value obtained from the tracker data. Separate values of the scaling factor for each frequency were trialled, but gave consistent results. In order to keep the number of parameters in the ω_a fits to a minimum a single scaling factor is used.
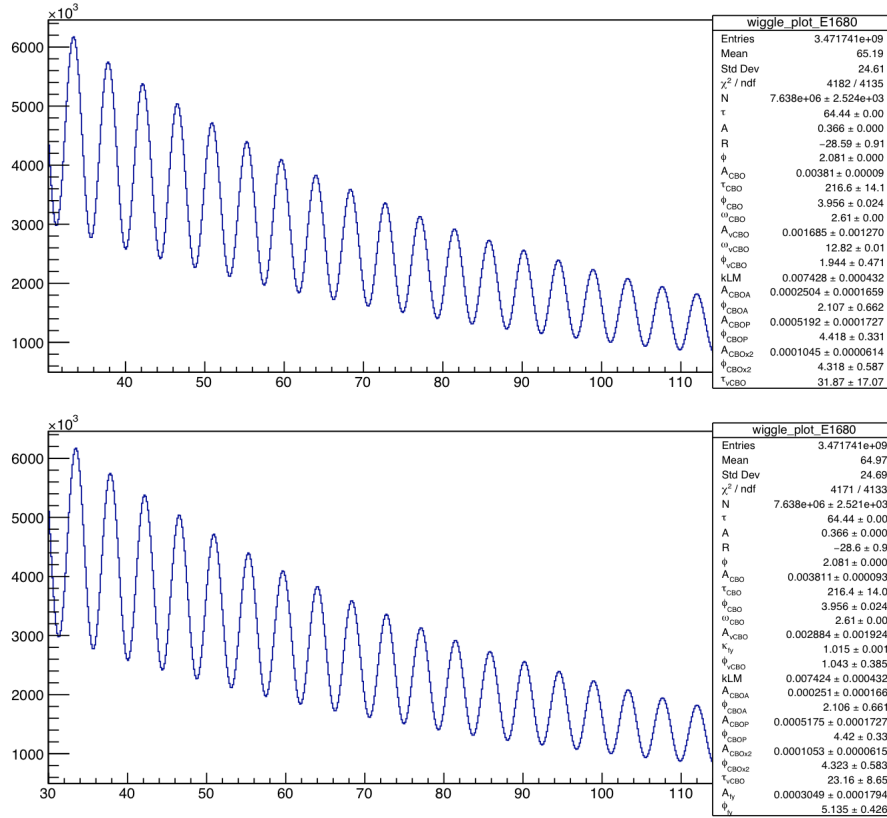
Figure 7.24: Plots of the ω_a fit results for the 9 day dataset before and after the kappa function is applied. The change in ω_a is only of the order of $\sim$ 5ppb, but it also improves the stability of the fit when carrying out cross checks, including per calorimeter scans and start time scans which change the start time of the fit to check that the parameters do not shift to a different value.

During Run-1 it was discovered that several of the quadrupole resistors were damaged. This meant that the quadrupole voltages had not reached their nominal values by the start of analysis data taking at 30μs, and were still changing throughout the fill. This was determined to be the cause of the varying vertical distribution of the stored muon beam. Therefore as the g–2 phase is different for each vertical position due its drift length, the varying vertical position would cause the average phase to change and lead to a systematic error. The quadrupole resistors were fixed during the shutdown between Run-1 and Run-2 and this effect has not been observed in any later data runs.
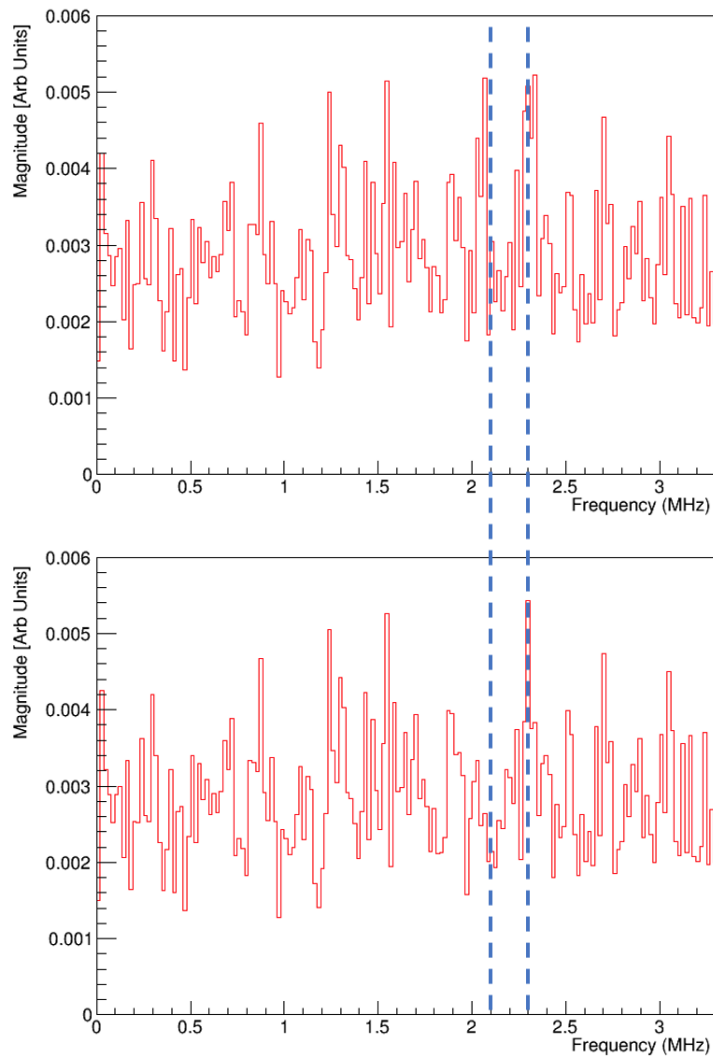
Figure 7.25: The top plot is an FFT of the residuals of the precession frequency fits for a constant vertical waist and vertical mean frequency. The slight excesses at ~ 2.1MHz and ~ 2.3MHz (blue dotted lines) cause unacceptably large χ^2 values. The bottom plot is an FFT of the residuals of the precession frequency fits, where the variation in the radial CBO frequency is converted to the corresponding variations in the vertical waist and mean, including the scaling parameter κ. It can be seen that the excess at ~ 2.1MHz has been removed and the excess at ~ 2.3MHz is reduced. The fits now have acceptable χ^2 values.

Chapter 8

Outlook

This thesis has described the design, construction and testing of the straw tracking modules of the Fermilab g–2 experiment. 22 modules were produced and 16 of these are currently installed in the experiment. These modules have been extremely reliable and have surpassed all the design specifications in terms of resolution and leak rate. This bears testament to the rigorous and stringent quality assurance procedures implemented throughout the construction of the modules.

Using data from the tracking detectors, I characterised the vertical motion of the muon beam as a function of time. Unanticipated changes in the vertical mean and width distributions of the beam showed evidence that the quadrupole voltage was changing in an unexpected way during the fill. The parameterisation of this behaviour has removed biases in the determination of ω_a.

The experiment has completed two data taking periods and accumulated a dataset over four times the size of the BNL E821 experiment (Figure 8.1). This and the subsequent data will produce the world's most precise determinations of a_μ. This is sufficient to establish evidence for BSM physics at more than seven standard deviations should the BNL a_μ value be confirmed.
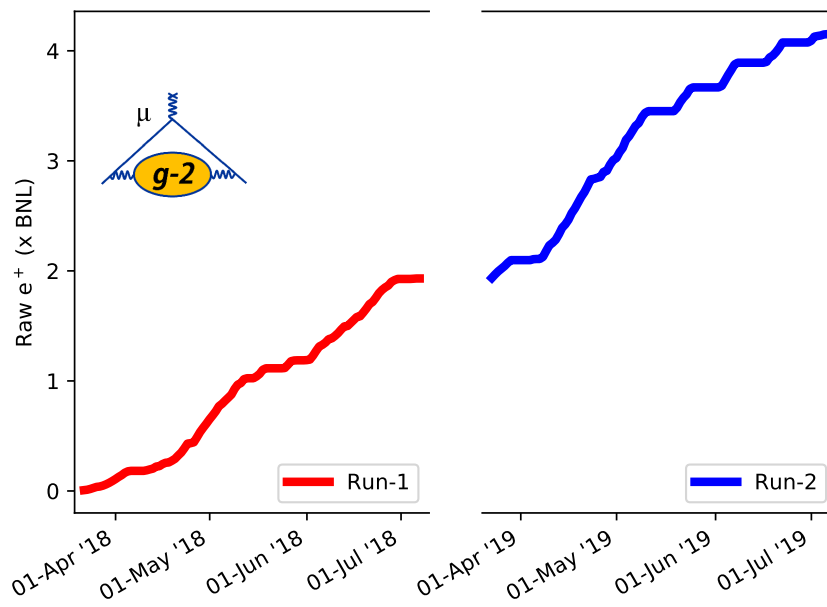
Figure 8.1: The number of recorded positrons as a fraction of the E821 dataset recorded to date by the Fermilab g–2 experiment.

Bibliography

[1] G. W. Bennett *et al.*, Final report of the E821 muon anomalous magnetic moment measurement at BNL, Phys. Rev. D73, 072003 (2006).

[2] J. Grange *et al.*, Muon g–2 Technical Design Report. (2015).

[3] C. D. Anderson and S. H. Neddermeyer, Cloud Chamber Observations of Cosmic Rays at 4300 Meters Elevation and Near Sea-Level, Phys. Rev. 50, 263 (1936).

[4] F. Farley and Y. Semertzidis, The 47 years of muon g–2, Progress in Particle and Nuclear Physics (2004).

[5] P. A. M. Dirac, The quantum theory of the electron, Proceedings of the Royal Society of London (1928).

[6] P. Kusch and H. M. Foleym, Magnetic Moment of the Electron, Phys. Rev. 74 (1948).

[7] J. Schwinger, On quantum-electrodynamics and the magnetic moment of the electron, Phys. Rev. 73, 416 (1948).

[8] R. Feynman, Space-Time Approach to Quantum Electrodynamics, Phys. Rev. 76, 769 (1949).

[9] S. Tomonaga, On a Relativistically Invariant Formulation of the Quantum Theory of Wave Fields, Progress of Theoretical Physics, 1 (2), 27 (1946).

[10] F. Dyson, The Radiation Theories of Tomonaga, Schwinger, and Feynman, Phys. Rev. 75, 486 (1949).

[11] S. Fogwell, D. Hanneke and G. Gabrielse, New Measurement of the Electron Magnetic Moment and the Fine Structure Constant, Phys. Rev. Lett. 100, 12080 (2008).

[12] T. Kinoshita, T. Aoyama and M. Nio, Revised and improved value of the QED tenth-order electron anomalous magnetic moment, Phys. Rev. D97, 036001 (2018).

[13] Richard H. Parker, Chenghui Yu, Weicheng Zhong, Brian Estey, Holger Müller, Measurement of the fine-structure constant as a test of the Standard Model, Science 13 Apr 2018: Vol. 360, Issue 6385, pp. 191-195 (2018).

[14] Bob Holdom, Two U(1)'s and ϵ charge shifts, Physics Letters B, Volume 166, Issue 2 (1986).

[15] G. Giudice, P. Paradisi and M. Passera, Testing new physics with the electron g–2, Journal High Energy Phys. 113 (2012).

[16] J. Abdallah *et al.* (DELPHI Collaboration), Study of Tau-pair Production in Photon-Photon Collisions at LEP and Limits on the Anomalous Electromagnetic Moments of the Tau Lepton, Eur. Phys. J. C 35 159 (2003).

[17] C.S. Wu *et al.*, Experimental Test of Parity Conservation in Beta Decay, Phys. Rev. 105, 1413 (1957).

[18] T. D. Yee and C. N. Yang, Question of parity conservation in weak interactions, Phys. Rev. 104, 254 (1956).

[19] F. J. M. Farley F. Combley and E. Picasso, The CERN muon (g–2) experiments, Physics Reports, 68, 93 (1981).

[20] M. Davier, A. Hoecker and B. Malaescu, Reevaluation of the hadronic vacuum polarisation contributions to the Standard Model predictions of the muon g–2 and $\alpha(M_Z^2)$ using newest hadronic cross-section data, Eur. Phys. J., C77 12, 827 (2017).

[21] A. Keshavarzi, D. Nomura and T. Teubner, The muon g–2 and $\alpha(M_Z^2)$: a new data-based analysis, Phys. Rev D97, 114025 (2018).

[22] M. Endo and W. Yin, Explaining electron and muon g–2 anomaly in SUSY without lepton-flavor mixings, J. High Energ. Phys. 122 (2019).

[23] S-P. Li, X. Li, and Y. Yang, Muon g–2 in a U(1) -symmetric two-Higgs-doublet model Phys. Rev. D 99, 035010 (2019).

[24] A. Doff, C. Siqueira, Composite Higgs models, Technicolor and the muon anomalous magnetic moment, Physics Letters B754, 294 (2016).

[25] E. Megias, M. Quiros, L. Salas, g–2 from Vector-like leptons in warped space, Journal of High Energy Phys. 16 (2017).

[26] E. de Rafael, J. P. Miller and B. L. Roberts, Muon g–2: Experiment and Theory, Reports on Progress in Physics 70 (2007).

[27] R. Frisch and O. Stern, Über die magnetische Ablenkung von Wasserstoffmolekülen und das magnetische Moment des Protons, Z. Phys. 85, 4 (1933).

[28] I. Estermann and O. Stern, Über die magnetische Ablenkung von Wasserstoffmolekülen und das magnetische Moment des Protons, Z. Phys. 85, 17 (1933).

[29] L. W. Alvarez and F. Bloch, A quantitative determination of the neutron moment in absolute nuclear magnetons, Phys. Rev. 57, 111 (1940).

[30] R. Garwin, L. Lederman and M. Weinrich, Observations of the Failure of Conservation of Parity and Charge Conjugation in Meson Decays: the Magnetic Moment of the Free Muon, Phys. Rev. 105, 1415 (1957).

[31] G. Charpak *et al.*, Measurement of the anomalous magnetic moment of the muon, Phys. Rev. Lett., 6, 128 (1961).

[32] J. Bailey *et al.*, The anomalous magnetic moment of positive and negative muon, Nuovo Cimento A9 369 (1972).

[33] J. Bailey *et al.*, Final report on the cern muon storage ring including the anomalous magnetic moment and the electric dipole moment of the muon, and a direct test of relativistic time dilation, Nuclear Physics B, 150(Supplement C):1-75, (1979).

[34] T. Aoyama *et al.*, Complete Tenth-Order QED Contribution to the Muon g–2, Phys. Rev. Lett. 109, 111808 (2012).

[35] J. Grange *et al.*, The New Muon g-2 Experiment at Fermilab, NUFACT2014, arXiv:1501.03040(2015).

[36] J. Price, Decay asymmetry. g-2 internal talk, G Minus 2 Experiment Document 3959-v1 (2016).

[37] D. Stöckinger, C. Gnendiger and H. Stöckinger-Kim, The electroweak contributions to muon g–2 after the Higgs-boson mass measurement, Phys. Rev. D88, 053005 (2013).

[38] F. Jegerlehner, The Anomalous Magnetic Moment of the Muon, Springer Tracts in Modern Physics (2008).

[39] A. Chapelain, The Muon g–2 experiment at Fermilab, Proceedings of the 12th Quark Confinement & the Hadron Spectrum Conference, EPJ Web Conf. Volume 137, 08001 (2017).

[40] K. Melnikov and A. Vainshtein, Hadronic light-by-light scattering contribution to the muon anomalous magnetic moment reexamined, Phys. Rev. D70, 113006 (2004).

[41] E. de Rafael, J. Prades and A. Vainshtein, The Hadronic Light-by-Light Scattering Contribution to the Muon and Electron Anomalous Magnetic Moments, Advanced series on directions in high energy physics, Lepton dipole moments, pp. 3003-317 (2009).

[42] A. Nyffeler, Precision of a data-driven estimate of hadronic light-by-light scattering in the muon g–2 : Pseudoscalar-pole contribution, Phys. Rev., D94 053006, (2016).

[43] B. L. Roberts J. P. Miller, E. de Rafael and D. Stöckinger, Muon g–2 : Experiment and Theory, Ann. Rev. Nucl. Part. Sci. 62, 237 (2012).

[44] A. Czarnecki and W. J. Marciano, The anomalous magnetic moment: A harbinger for new physics, Phys.Rev. D64, 013014 (2001).

[45] B. L. Roberts, Searching for physics beyond the Standard Model through the dipole interaction, J. Phys. Conf. Ser. 295 012027 (2011).

[46] D. Stöckinger, g–2 and physics beyond the Standard Model, Nuclear Physics B - Proceedings Supplements 1182, 1 (2008).

[47] D. Stöckinger, The Muon Magnetic Moment and Supersymmetry, J. Phys. G34, 45 (2007).

[48] P. Mohr, D. Newell and B. Taylor, CODATA recommended values of the fundamental physical constants, Rev. Mod. Phys. 88 (2016).

[49] W. Liu, M. G. Boshier *et al.*, High Precision Measurements of the Ground State Hyperfine Structure Interval of Muonium and of the Muon Magnetic Moment, Phys. Rev. Lett. 82, 711 (1999).

[50] D. Stratakis *et al.*, Performance analysis for the new g–2 experiment, Proceedings of IPAC2016, (2016).

[51] J. Holzbauer, The Muon g–2 Experiment Overview and Status, 19th International Workshop on Neutrinos from Accelerators: arXiv:1712.05980 (2017).

[52] N. Kinnaird, Muon spin precession frequency extraction and decay positron track fitting in run 1 of the fermilab muon g–2 experiment, PhD Thesis, Boston University (2020).

[53] G. T. Danby *et al.*, The Brookhaven muon storage ring magnet, Nucl. Instrum. Meth. A457 151-174 (2001).

[54] M. Farooq, T. Chupp, and Muon g-2 Collaboration Collaboration, Absolute Calibration of the Magnetic Field Measurement for Muon g–2, In APS April Meeting Abstracts, p F1.036, (2017).

[55] D. Flay, Precision Magnetic Field Calibration for the Muon g–2 Experiment at Fermilab, PoS, ICHEP2016 1075 (2017).

[56] J. Kaspar *et al.*, Design and performance of SiPM-based readout of PbF_2 crystals for high-rate, precision timing applications, JINST 12, P01009 (2017).

[57] A. Anastasi *et al.*, Test of candidate light distributors for the muon g–2 laser calibration system, Nucl. Instrum. Meth. A788 43-48 (2015).

[58] L. P Alonzi *et al.*, The calorimeter system of the new muon g–2 experiment at Fermilab, Nucl.Instrum.Meth. A824 (2016).

[59] B. Martinez *el al.*, Development and Testing of Scintillating Detectors for the Muon g–2 Experiment, APS Division Nuclear Physics Vancouver Meeting (2016).

[60] W. Collins, Building IBMS Detectors for Muon g–2, Phys. Rev. D64:013014, (2016).

[61] G.I. Merzon V.A. Chechin V.K. Ermilova, L.P. Kotenko. Primary specific ionization of relativistic particles in gases, Soviet Journal of Experimental and Theoretical Physics, Vol. 29, p.861 (1969).

[62] W. Blum *et al.*, Particle Detection with Drift Chambers, Springer-Verlag Berlin Heidelberg (2008).

[63] Fabio Sauli, Principles of operation of multiwire proportional and drift chambers, Geneva : CERN, page 92, (1977).

[64] J. D. Crnkovic *et al.*, Lost muon studies for the muon g-2 experiment at fermilab, E989 Collaboration internal meeting, Document number GM2-doc-6189-v7, (2017).

[65] G. W. Bennett *et al.*, Improved limit on the muon electric dipole moment, Phys. Rev. D 80, 052008 (2009).

[66] E. Nagy, V. Innocente and M. Maire, GEANE: Average Tracking and Error Propagation Package, Proceedings of Workshop on Detector and Event Simulation in High-energy Physics (MC 91), p.58-78, (1991).

[67] N. Kinnaird, Geane track fitting, Internal g–2 Note, Document 8102-v3. (2017).

[68] E. Nyström, Güber die numerische integration von differentialgleichungen, Acta Soc. Sci. Fenn. 50, 1-54 (1925).

[69] I. Gavrilenko, E. Lund, L. Bugge and A. Strandlie, Track parameter propagation through the application of a new adaptive Runge-Kutta-Nyström method in the ATLAS experiment, JINST 4, P04001 (2009).

[70] W. Bokhari *et al.*, The ASDQ ASIC for the Front End electronics of the COT, CDF/DOC/Tracking/CDFR/4514 (1999).

[71] T. Stuttard, The development, testing and characterisation of a straw tracking detector and readout system for the Fermilab muon g–2 experiment, PhD Thesis, University College London (2017).

[72] W. Turner, The construction and commissioning of the straw tracking detector in the new muon g–2 experiment at Fermilab, PhD Thesis, University of Liverpool (2018).

[73] K. Labe, Muon E989 Clock System Manual, Internal g–2 Document GM2-doc-10995-v4 (2019).

[74] CAEN SY127, `http://www.tunl.duke.edu/documents/public/electronics/CAEN/caen_sy127.pdf`.

[75] C. Green, *et al.*, The Art Framework, J. Phys. Conf. Ser., 396:022020, (2012).

[76] Metrosoft Quartis, `https://www.metromec.ch/images/pdf/quartis/Metrosoft_QUARTIS_EN.pdf`.

[77] Lloyd LRX Plus materials tester, `http://www.jlwinstruments.com/index.ph/products/products-library/lrx-series-materials-testing-machine`.

[78] Epsilon Extensionometer, `https://www.ametektest.com/media/ametektest/download_links/epsilon_extensometer_catalogue.pdf`.

[79] Silver epoxy TraDuct 2902, `https://bondlab-qa.web.cern.ch/bondlab-qa/glues/data-sheets/tra-con_tra-duct-2902.pdf`, (2002).

[80] J. Crnkovic *et al.*, Muon g–2 storage ring beam and spin dynamics, Internal g–2 Document GM2-doc-9191-v24 (2019).

[81] S. Ganguly *et al.*, Lost muon study for the muon g–2 experiment at Fermilab, Proceedings of IPAC2018, J. Phys.: Conf. Ser. 1067 011001 (2018).

[82] D. L. Rubin *et al.*, Muon beam dynamics and spin dynamics in the g–2 storage ring, Internal g–2 Document 11847-v2, (2018).

[83] James P. Miller and B. Lee Roberts, The Muon (g–2) Spin Equations, the Magic γ, What's small and what's not, arXiv:1805.01944v2, (2018).